Pulsed Electronic Speckle Pattern Interferometry (ESPI)

by

Bernardino Barrientos García
M. en C., Ing. en Elec. y Mec.

Thesis submitted in partial
fulfilment of the requirements for
the award of Doctor of Sciences from
Centro de Investigaciones en Optica, A. C.
(Universidad de Guanajuato)

August 1999

This work is dedicated to my family

Francisco García
Natividad Salinas
Isabel Barrientos
Juana Juárez
Ignacio Barrientos Juárez
Sara García Salinas
Raúl Barrientos García
Cristina Barrientos García
Miguel Barrientos García
Simeón Barrientos García
Josefina Barrientos García
Arturo Barrientos García
Ma. del Carmen Barrientos García
Gregorio Barrientos García
Ignacio Barrientos García
Juan Gabriel Barrientos García
Alejandro Barrientos García

Acknowledgements

Contents

Summary

A novel Electronic Speckle Pattern Interferometry, ESPI, technique is presented in this work. The technique consists of an out-of-plane interferometer which incorporates a specially fabricated computer-generated hologram. This hologram allows us to achieve spatial phase stepping and therefore analysis of transient phenomena becomes feasible. The advantage of this technique is the calculation of deformation by means of a double exposure method where no changes of any kind are necessary to be introduced between consecutive recordings.

Chapter I   Introduction

The fields of vibration analysis and mechanical design both make use of experimental, analytical and numerical techniques to determine or predict the mechanical behaviour of a certain sample under particular loading conditions. In connection with analytical and numerical techniques for mechanical analyses we may mention Soderberg and deformation energy techniques [1] and finite element methods [2,3,4], respectively. The main drawback of the former relates to the relatively small number of boundary conditions and specimen shapes for which analytical solutions can be found. Finite element methods can overcome these restrictions, but calculations can be extremely time-consuming and the results should be verified, possibly using a suitable experimental technique. The most common conventional experimental technique uses accelerometers positioned in a matrix of single points across the object surface [5]. The spacing of the accelerometer matrix positions must be sufficient to perform a confident interpolation between neighbor positions, i.e. to ensure the minimum spatial resolution. For instance, in vibration analysis, if the frequency range is high and the structure large, say $1\,m^2$, then the required spacing of the accelerometers may be 5 cm apart in order to accurately produce a surface map of displacement. The positioning of a large number of accelerometers is expensive and time-consuming. Furthermore, the presence of even a single accelerometer may affect the surface motion to be measured.

Many optical techniques have been used to make experimental measurements, because they are, by nature, non-destructive and non-contact. Of particular interest are interferometric techniques which allow extremely small deformation measurements to be made. Techniques based on holographic interferometry [5,6,8] and speckle pattern interferometry [5,6,7,9,10] are attractive because often, no special preparation of the test object surface is required. Both holographic interferometry and speckle pattern interferometry are based on a double-exposure method in which two images are recorded, before and after deformation. These two images are compared to produce fringes related to the deformation of the object. The process by which the fringes are produced will be described later. The errors introduced in a measurement, as in the case of classical interferometry [23], e.g. in a Michelson interferometer, due to the low-quality of optical components, are cancelled out identically in this case.

In holographic interferometry, a holographic plate works as a recording device. The main

disadvantages are the following. The development of the hologram plate is time-consuming; localization of the interference fringes is not straightforward in many cases; separation of the out-of-plane deformation (along the observation direction) from the in-plane component (perpendicular to the observation direction) is not direct [11] (these deformation components are important because the strain, bending and stress are proportional to them). Furthermore, in real-time observation the hologram has to be developed in-situ or exactly repositioned.

Speckle pattern interferometry, unlike holographic interferometry, enables the employment of recording devices with low resolution. A photographic emulsion [9] or a television camera [12] can be used: in the latter case the technique is called electronic speckle pattern interferometry (ESPI). The first ESPI results were presented for vibrating objects in 1971 by Butters and Leendertz [12] using a CW laser. The stability conditions were less restrictive than for holographic interferometry because the exposure could be shorter. However, the optical system still had to be rigidly mounted and environmental conditions controlled. Electronic processing meant that no film needed to be developed and that the deformation could be observed in real time. Therefore, ESPI overcomes several of the disadvantages of holographic interferometry. The main drawback of ESPI is the low-quality of the fringe patterns due to speckle noise.

In recent work, pulsed light sources were used in ESPI [6,13,14,15] as to reduce the influence of environmental disturbances [13,14,15]. As it is pointed out in Ref. 7, 13 and 15, double-pulsed addition ESPI enables interferometric measurements to compensate further for external disturbances. In this case, two laser pulses are fired during one TV field. Consequently, the two pulses are added on the same field, and this gives rise to correlation fringes related to the deformation applied between pulses. The pulses can be the throughput of a Q-switched laser, which can deliver pulses of a few nanoseconds. These short pulses effectively freeze object motion when both spurious and object frequencies are low. This enables us to analyze harmonic vibration and transient deformation measurements in the presence of considerable rigid body motion or environmental disturbances. Pulse pairs can be obtained by double-pulsing a single laser cavity [13] or by using a laser with two cavities [7,15,16].

The assessment of the optical phase (and hence the deformation) can be implemented typically by phase-stepping and carrier-fringe approaches. Temporal phase-stepping [15], where an increasing phase change is introduced between the object and reference beam of the interferometer in three consecutive TV fields, is clearly not suitable for transient deformation or

harmonic vibration analyses when the object is unstable on the time-scale of four TV fields. Carrier fringe pattern techniques allows us to calculate the optical phase from a single TV field [7] and are therefore suitable for transient deformation measurements of the type described in reference [17]. However, the range of deformation measurements for the fringe carrier methods is reduced with respect to phase-stepping. An alternative technique for transient deformation studies is spatial phase-stepping [18], in which an interferometer is modified so that at least three phase-stepped images are recorded simultaneously. The measurement range is preserved but a more complicated experimental arrangement is required. Spatial phase-stepping is typically based on polarization control [19] or on a diffraction grating [20,21]. In the latter, it is usual to translate the grating laterally in order to introduce equal and opposite phase steps in the +1 and -1 diffraction fields.

The main aim of this work was to investigate a new spatial phase-stepping technique. The technique is based on a computer-generated hologram (CGH) similar to one used for point range measurements in a Twyman-Green interferometer [22]. We used a special CGH, which apart from diffracting the light into four separate fields it also introduces a phase change between these fields. Thus, in such a case there is no need to transversely move the CGH in order to introduce a phase change. The results of this work are demonstrated for ESPI, but the methods may be applied to other optical metrology techniques.

I-1   References

[01] S. Timoshenko, *Resistencia de materiales II*, Espasa-Calpe Barcelona 468 (1945).

[02] R. D. Cook, *Finite Element Modeling for stress analysis*, John Wiley & Sons NY (1995).

[03] C. C. Spyrakos, *Finite Element Modeling in Engineering Practice*, Algor Pub. Division, Pitt. PA (1994).

[04] R. J. Pryputniewicz, "holographic and finite element studies of vibrating beams," SPIE **599** 54-62 (1985).

[05] J. R. Tyrer, "Application of pulsed holography and double pulsed electronic speckle pattern interferometry to large vibrating engineering structures," SPIE **599**, Opt. in Eng. Measur., 181-188 (1985).

[06] R. G. Hughes, "The determination of vibration patterns using a pulsed laser with holographic and electronic speckle pattern interferometry techniques," *The engineering uses of coherent optics*, E. R. Robertson (Ed.), CUP, U. K. 199-218 (1976).

[07] A. J. Moore and C. Pérez-López, "Fringe carrier methods in double-pulsed addition ESPI," Opt. Comm., **141**, 203-212 (1997).

[08] P. Boone and R. Verbiest, "Application of hologram intereferometry to plate deformation and translation measurements." Opt. Acta **16**(5) 555-567 (1969).

[09] J. A. Leendertz, "Interferometric displacement measurement on scattering surfaces utilizing speckle effect," J. Phys. E: Sci. Instrum. **3**, 214-218 (1970).

[10] J. A. Leendertz and J. N. Butters, "An image-shearing speckle-pattern interferometer for measuring bending moments," J. Phys. E: Sci. Instrum. **6**, 56-59 (1973).

[11] R. Jones and C. Wykes, *Holographic and Speckle Interferometry: A discussion of the theory, practice and application of the techniques*, CUP, U. K. (1983).

[12] J. N. Butters and J. A. Leendertz, "Holographic and video techniques applied to engineering measurement," Meas. & Control **4** (12), 349-354 (1971).

[13] T. J. Cookson, J. N. Butters and H. C. Pollard, "Pulsed lasers in electronic speckle pattern interferometry," Opt. and Laser Tech. **10**, 119-124 (1978).

[14] R. Spooren, "Double-pulse subtraction TV holography," Opt. Eng. **31**, 1000-1007 (1992).

[15] A. J. Moore and C. Pérez-López, "Fringe visibility enhancement and phase calculation in double-pulsed addition ESPI," J. Mod. Opt. **43**, 1829-1844 (1996).

[16] M. C. Shellabear, F. Mendoza-Santoyo and J. R. Tyrer, "Processing of addition and subtraction fringes from pulsed ESPI for the study of vibrations," Proc. SEM Conference on Hologram Interferometry and Speckle Metrology, K. A. Stetson and R. J. Pryputniewicz, Eds. 238-244 (1990).

[17] A. Fernández, A. J. Moore, C. Pérez-López, A. F. Doval and J. Blanco-García, "Study of transient deformation with pulsed TV holography: application to crack detection," App. Opt. **36**, 2058-2065 (1997).

[18] T. D. Upton and D. W. Watt, "Optical and electronic design of a calibrated multichannel electronic interferometer for quantitative flow visualization," App. Opt. **34**, 5602-5610 (1995).

[19] . A. J. P. Haasteren and H. J. Frankena, "Real-time displacement measurement using a multicamera phase-stepping speckle interferometer," App. Opt. **33**, 4137-4142 (1994).

[20] O.Y. Kwon and D.M. Shough, "Multichannel grating phase-shift interferometers," SPIE **599**, 273 (1985).

[21] M. Kujawinska and D. W. Robinson, "Multichannel phase-stepped holographic interferometry," App. Opt. **27**, 312-320 (1988).

[22] M. Deininger, L. L. Wang, K. Gerstner and T. Tschudi, "Optical phase step method for absolute ranging interferometry using computer-generated holograms," App. Opt. **34**, 5620-5623 (1995).

[23] D. Malacara, M. Servín, Z. Malacara, *Interferogram analysis for optical testing*, Marcel Dekker Inc., U. S. A. (1998).

Chapter II   Pulsed ESPI and spatial phase-stepping

The background of ESPI metrology is presented in this chapter. This includes a brief description of well-known tools necessary in the study of optical measurements, such as implementation of experimental setups, synchronization schemes, phase extraction methods, and unwrapping algorithms. Regarding the former, the employment of a diffractive optical element is investigated.

II-1   ESPI

Fig. II-1 shows a basic ESPI arrangement, sensitive to out-of-plane displacements, which is similar to a Mach-Zehnder interferometer. A coherent input light beam is split into two components, a reference beam and an object beam; the former being detected directly by a CCD camera. The object beam is collected by means of a SLR (single lens reflex) zoom lens and then combined with the reference beam through a beam combiner before being imaged onto the CCD.
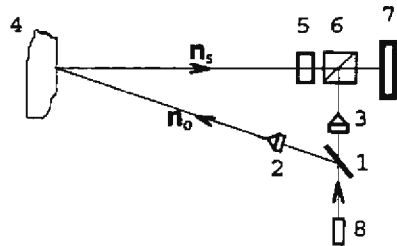
Fig. II-1. ESPI arrangement with out-of-plane sensitivity (in-line geometry). 1. Beam splitter; 2,3. Beam expander; 4. Object under test; 5. Zoom lens; 6. Beam combiner; 7. CCD camera; 8. Illumination source. Here n_o and n_s stand for the illumination and observation unit vectors, respectively.

II-1.1   Static deformation measurements with CW ESPI

In order to measure static deformation, due to the application of a constant and permanent load, we make use of a CW laser (e.g. an Argon laser) as the source of light in Fig. II-1. As it was mentioned in the preceding chapter, environmental disturbances should be kept to a minimum in the time between two consecutive acquisitions if their influence is to be minimized during the measurement.

II-1.1.1   Fringe formation

When the object beam and the reference beam are combined an interference pattern (a phase-referenced speckle pattern) in the space after the beam coupler is formed and can be expressed as [1],

$$I_{und}(x,y) = I_o(x,y) + I_r(x,y) + 2\sqrt{I_o(x,y)I_r(x,y)}\cos[\psi(x,y)], \tag{II-1}$$

where I_r and I_o denote the intensities of the reference and object beams, respectively, on a pixel with coordinates (x,y), and $\psi(x,y)$ is the optical phase between the two beams. At least one of the beams contains a speckle pattern, and hence $\psi(x,y)$ varies randomly with position. The first two terms on the right hand side of Eq. (II-1) represent a randomly-varying background (DC) term. The cosine function of the third term represents modulation and is related to the contrast of the interference pattern at the CCD plane (image plane.)

The phase relation to surface deformation can be found by calculating the optical path difference (Δs) that arises when the object is displaced by a distance d [1]:

$$\Delta s = (\bar{n}_o - \bar{n}_s) \cdot \bar{d}, \tag{II-2}$$

where n_o and n_s represent the unit vectors along the illumination beam and the observation direction, respectively, see Fig. II-1. In the case of out-of-plane displacement measurements the sensitivity direction is in the observation direction. In this case, it is desirable that $n_o \approx -n_s$, so that the in-plane component does not contribute significantly to the measured displacement. Thus, the corresponding optical phase change is given by

$$\begin{aligned}\phi &= k\,\Delta s \\ &= 2kd, \end{aligned} \tag{II-3}$$

where k is the propagation vector ($2\pi/\lambda$, with λ the wavelength of the source.) Thus, after an out-of-plane displacement of the object, the intensity at pixel (x,y) will be expressed by:

$$I_{def}(x,y) = I_o(x,y) + I_r(x,y) + 2\sqrt{I_o(x,y)I_r(x,y)}\cos[\psi(x,y) + \phi(x,y)]. \tag{II-4}$$

It is assumed that external noise is so small that $\psi(x,y)$ does not change significantly between consecutive interference patterns (undeformed and deformed).

Interferometric techniques enable us to compare a particular interference pattern with a reference pattern, with deformation (Eq. (II-4)) or without deformation (Eq. (II-1)). Standard comparison methods include subtraction, addition and relational operators.

Subtracting Eq. (II-4) from Eq. (II-1), yields

$$I_{sub}(x,y) = 4\sqrt{I_o(x,y)I_r(x,y)}\left|\sin\left[\psi(x,y) + \frac{1}{2}\phi(x,y)\right]\sin\left[\frac{1}{2}\phi(x,y)\right]\right|.$$

(II-5)

Notice that the background terms in the original expressions cancel each other. This is valid, only if pixel intensities remain virtually unchanged during the measurement and only their phase difference changes. The modulus is included to remove negative intensity values which cannot be displayed on the TV monitor. Eq. (II-5) represents a high-frequency random term that modulates a low-frequency term, which in turn gives rise to a fringe pattern related to deformation. This technique can be implemented in real-time by means of a frame grabber: A referenced speckle interference pattern is stored in memory and subtracted continuously from the current field at a rate of 60 Hz (every 16.7 ms).

If the phase-referenced speckle patterns before and after deformation are compared by addition, then the resulting intensity will be given by

$$I_{add}(x,y) = 2[I_o(x,y) + I_r(x,y)] + 4\sqrt{I_o(x,y)I_r(x,y)}\cos\left[\psi(x,y) + \frac{1}{2}\phi(x,y)\right]\cos\left[\frac{1}{2}\phi(x,y)\right].$$

(II-6)

In this case, the fringe pattern represented by Eq. (II-6) has a high content of speckle noise since the random DC terms are not cancelled out but reinforced. It is common to apply an electronic high-pass filter to fringe patterns of this type in order to eliminate this term [2].

By comparing the last two equations, we can see they give similar fringes but with a lag of π rad. This means that a black fringe in the subtraction operation corresponds to a bright fringe when signals are added.

The F number of the zoom lens (f/D, where f is the effective focal length and D the diameter of the exit pupil) defines the spatial frequency content of the phase-referenced interference images. As the pupil is stopped down, the average speckle size on the detector increases according to

the point spread function of the zoom (d_{sp}=2.4λv/D, v is the zoom-to-CCD distance and d_{sp} the average diameter of the speckles at the CCD plane). As is explained in **Appendix A**, the average diameter of the speckle must be of the order of the pixel size to have good intensity modulation and hence good fringe contrast. However, there should be a balance between the speckle size and the intensity at each pixel. The degree of decorrelation, due to a change of the collected scattering angles from the object, of two interference patterns at a point also modifies the contrast at that point.

II-1.1.2   Phase-stepping

Phase-stepping [3,4,5,6,7,8,9,71,73] enables us to extract the phase embedded in a phase-referenced speckle pattern. This method involves the recording of at least three sequential interference images with a constant phase step between them at a particular deformation state. To calculate the optical phase ψ(x,y) in Eq. (II-1), a system of at least three equations must be formed since Eq. (II-1) has three unknowns (I_o(x,y), I_r(x,y) and ψ(x,y)):

$$I_{und,i}(x,y) = I_o(x,y) + I_r(x,y) + 2\sqrt{I_o(x,y)I_r(x,y)}\cos[\psi(x,y) + \theta_i(x,y)], \tag{II-7}$$

where θ_i represents the phase step introduced into each speckle image and i={1,2,3, ...N}, where N is the total number of images at a certain deformation state. One way to define θ_i is by setting it equal to (i-1)2π/N rad. This stepping can be carried out by changing the optical path of the reference beam in Fig. II-1 by the employment of a PZT piezoelectric element. With N=4, the optical interference phase can be extracted from [8]

$$\psi(x,y) = \tan^{-1}\frac{I_2(x,y) - I_4(x,y)}{I_3(x,y) - I_1(x,y)}, \tag{II-8}$$

where I_i (i=1,2,3,4) are the intensity values at each pixel at the coordinates (x,y), respectively, at a particular state of deformation.

The assessment of the optical interference phase can also be achieved by another 4-step algorithm due to Carré [10,11,12]. The phase steps need not necessarily be known in advance as in the previous case. However, an unknown linear phase step of 2α is assumed between consecutive captures, so that the values of the stepping phases are θ_i(x,y)={-3α(x,y),-α(x,y),α(x,y),3α(x,y)}. The interference phase can then be found using

$$\psi(x,y) = \tan^{-1}\frac{\sqrt{[3(I_2 - I_3) - (I_1 - I_4)][(I_2 - I_3) + (I_1 - I_4)]}}{(I_2 + I_3) - (I_1 + I_4)},$$

(II-9)

where the (x,y) dependence of the measured intensities has been omitted. Due to the fact that this algorithm does not assume a constant phase step for the whole image but for each single pixel, it can compensate for errors in phase shift as well as for spatial variations of the phase shift. Therefore, it makes possible the use of diverging reference beams in conjunction with low precision PZT drivers. However, this algorithm requires that the phase steps at a given pixel element be constant. The phase step can be calculated by

$$\alpha(x,y) = \tan^{-1}\frac{\sqrt{3(I_2 - I_3) - (I_1 - I_4)}}{(I_2 - I_3) + (I_1 - I_4)}.$$

(II-10)

The (x,y) dependence of intensities is again dropped. The computation of $\alpha(x,y)$ is discussed further in **Appendix C**.

Two methods have been proposed for the determination of the optical phase due to deformation. In the first one [5,6,7] (see Fig. II-2a), the optical phase at the reference state, $\psi(x,y)$, and at the deformation state, $\psi(x,y)+\phi(x,y)$, are calculated (as is indicated by Eq. (II-8) or Eq. (II-9)). Subtraction of these phase terms corresponds to the phase resulting from the object deformation at each pixel, according to Eq. (II-3). This method (labeled here as DOP, difference-of-phase method) does not produce any interference fringes. When using either Eq. (II-8) or Eq. (II-9), e.g. for a reference state, each intensity I_i has the form of that given by Eq. (II-1). On the other hand, a second method makes use of expressions of the type of Eq. (II-5), producing N sets of interference fringes [7,8,9]. The intensities obtained for correspondent pixels are then included in Eq. (II-8), and the phase calculated (see Fig. II-2b). This method is labeled here as POD (phase-of-difference method). It has been shown that DOP results are better than those obtained by POD [9], mainly because nonvalid pixels (low-modulation pixels) can be excluded. In the case of addition fringes, the POD method is the only method that can be applied because the constituent speckle patterns (before and after deformation) cannot be separated. This is due to the fact that both acquisitions are grabbed in the same field. Recently, the phase of addition fringe patterns was extracted for the first time by applying Eq. (II-8) and using a comparison subtraction phase

map [7].
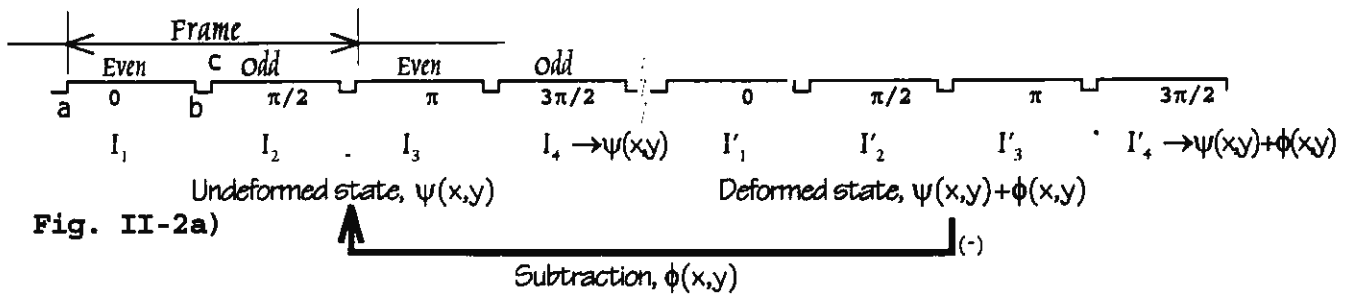
Fig. II-2a)
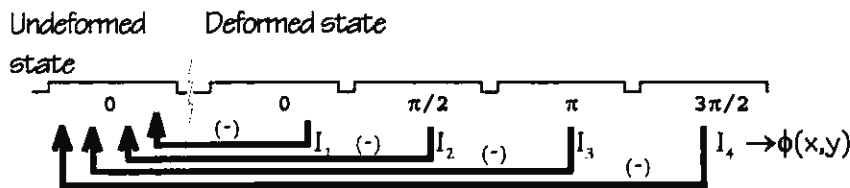
Fig. II-2b)
Fig. II-2. A TV frame is composed of two interlaced fields (even and odd). Every TV field consists of a scanning (acquisition) time (**ab**) and a blanking (transfer-gate) time (**bc**). In a NTSC-RS170 communication system, there are 30 frames per second. Then, when working with fields only half the spatial resolution of the CCD is available. a) DOP method (8 intensity measurements are needed.) b) POD method (5 intensity measurements are needed.)

II-1.1.3   Fringe carrier

Fringe carrier methods allow the optical interference phase to be calculated using only one interferogram. This can be done by either handling a fringe pattern in the spatial domain [13,14,69] (spatial synchronous detection, SSD), or in the frequency domain (FT) [14,15,72]. In the latter, the intensity signal must be mapped onto the Fourier plane, where it is low-pass filtered, and returned to the spatial plane, before the phase is extracted. For the former method, it is only necessary to multiply the original signal by two fringe carrier frequencies in phase quadrature (e.g., a sine and a cosine), they are then low-pas filtered, and the phase recovered. Both methods need the introduction of a carrier frequency in order to remove phase ambiguities. When analyzing rapid transient events, introduction of a carrier frequency is not straightforward since the required separation between consecutive captures are of the order of a few μs. However, it has been demonstrated for both SSD [14,16] and FT [17] that the phase can be recovered without introducing any fringe carrier, which in turn means that the sign of the deformation is ambiguous and must

be supplied by an operator taking into account the deformation conditions. Spatial methods for analyzing fringe patterns are faster than Fourier methods since they do not need a fast Fourier transform (FFT) computation followed by an inverse FFT. Spatial methods, however, are less accurate.

A disadvantage of these techniques when compared with phase-stepping methods is the reduction of the range of displacement measurements that arises from the introduced phase carrier fringes. These limit the spatial resolution of the detection device.

II-1.1.4   Phase unwrapping

As we have seen, the phase is recovered through the tangent function, see Eqs. (II-8) and (II-9). Thus, the range of the computed phase values goes from -π to π, or equivalently from 0-2π. If more than one fringe is present, phase discontinuities appear. Fig. II-3a shows a line of a raw (wrapped) phase map that contains several 2π jump discontinuities. By integrating (unwrapping) these discontinuities, we can calculate the actual phase by adding a multiple of 2π sequentially starting on the left until the end of a line of pixels, as shown in Fig. II-3b. At the end of a line, the next line is scanned in the reverse direction. This procedure results in an integration of the raw phase data line by line. This is the simplest unwrapping algorithm [18]. It may suffice when classical inteferometry is used to measure the aberrations in an optical component, since it is possible to produce good quality interferograms with a high signal-to-noise ratio. The unwrapped phase represents the physical parameter that is being measured, e.g. displacement.
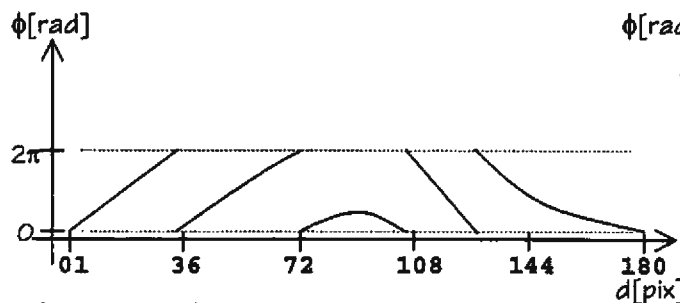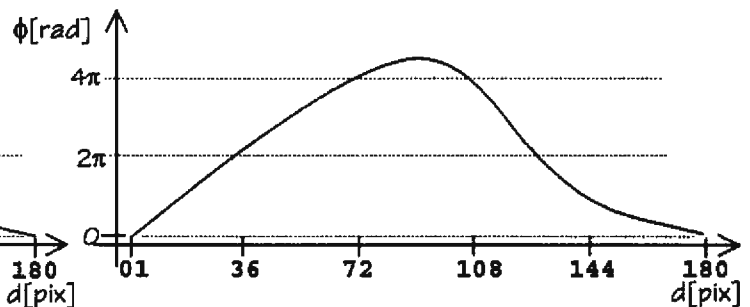
Fig. II-3a)   Fig. II-3b)

Fig. II-3. a) Wrapped (raw) phase map. The arctangent function inherently gives 2π discontinuities. A line of pixels with 5 fringes is shown. b) Unwrapped phase map. Where 2π discontinuities are detected, a multiple of 2π is added or subtracted from a neighbouring-pixel phase.

If the unwrapped map is not expected to be continuous, more sophisticated algorithms have to be employed [19-22]. Problems arise when the data is undersampled; the sampling frequency must be at least twice the fringe spatial frequency. Further problems arise because of random noise (as in speckle interferometry), when there are holes or masked data, when there are low phase modulation pixels, and in general when path inconsistencies are found. This is explained below. Therefore, preprocessing of the data is certainly necessary when dealing with speckle patterns. This preprocessing consists of marking bad phase pixels and occasionally smoothing and low-pass averaging. However, these operations may lead to the elimination of valid fringe data. This is particularly true when there are several fringe frequencies in the data and then the filter size plays an important role [23].

The unwrapping algorithm employed in **Chapter IV** is described next. First, when calculating the optical phase, pixels with a modulation less than a pre-selected threshold value (see *Appendix C*) are marked as invalid (masked pixels). These pixels are eliminated and therefore are not unwrapped. Then, we look for phase inconsistencies. In this step, we make use of one important feature of unwrapping, that the integration of phase discontinuities along a closed path should be zero. This arises from the fact that the phase at a certain pixel is unique when unwrapping along different paths [20]. In this operation every pixel in the image and 3 of its neighbours in a small square are examined. The four phase values can be unwrapped around the square. Since the sampling theorem requires that there must be at least two pixels per fringe, the phase gradient between two neighboring pixels is expected to be less than π, otherwise it implies that a 2π-phase discontinuity has been found. As Fig. II-3 shows, a discontinuity may be positive or negative. It is positive when the discontinuity goes from 2π to 0. We assign a +1 to this phase jump, −1 to its opposite, and 0 otherwise (when the absolute phase gradient is less than π.) Adding these indices for the four phase-pixel gradients, we get 0 or another number. If it is 0, the phase has returned to its original value having gone around the square, and the phase is said to be consistent. No action is taken. If the phase is a multiple of 2π when returning to the starting pixel of the group of 4 pixels, the phase is inconsistent and all 4 pixels are marked as invalid. These pixels are excluded during the next step: application of a path dependent unwrapping algorithm. A spiral scanning method is used [24]. It starts at a central pixel and measures the phase gradient between the current pixel and all the unmasked 3x3 neighboring pixels that have already been unwrapped (i.e. pixels for which a multiple of 2π has been determined). The current unwrapped value is assigned considering a "voting" system that involves those neighboring pixels

previously unwrapped. The process is repeated by spiraling around the growing central area of the unwrapped data, Fig. II-4a. The unwrapping propagates in a circular direction from the selected starting point. A disadvantage of this method is that errors propagate in the radial direction when a clump of masked pixels is encountered. Despite this, it produces in general good results. Once the integration has been carried out, optionally the unwrapped phase values can be sorted and the central pixel replaced with the median phase value present in the ordered array of neighboring pixels. The purpose of this optional procedure is to reduce the number of masked pixels. Simple median filters affect the boundaries of good pixel regions. In fact, these regions are enlarged. Thus, to overcome this problem, a morphological operation [22,25] is performed on the latter masked map where a dilation process is used to generate another index map. The dilation operator enlarges the number of marked pixels (in black in Fig. II-4b). As is shown in Fig. II-4b, the object boundaries are reduced and the invalid pixel areas are expanded.
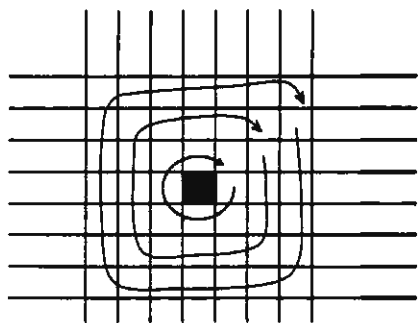
Fig. II-4a) Spiral scanning method. Unwrapping is carried out around a central reference pixel. The number of pixels that determine the phase of a pixel varies from 2 to 4.
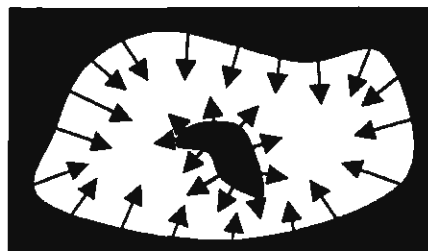
Fig. II-4b) Dilation process as expansion of the invalid-pixel zones (in black).

In **Chapter V**, we have used a path-independent unwrapping algorithm [26], the algorithm of Kerr et al [19], which produces better results than those obtained with the spiral algorithm but takes much more time. In order to verify consistent phase loops, the data is unwrapped by following all possible paths between any two pixels. In the implementation of this method, a phase-inconsistency map is first calculated, as was required in the spiral algorithm. This approach is based on a least-squares minimization technique using a fast discrete cosine transform. The quantity to be minimized is the difference between the gradients of wrapped neighboring pixels and unwrapped neighboring pixels. Phase gradients should be identical in both the wrapped and the unwrapped images. In order to eliminate phase inconsistencies, several iterations are

performed on the whole phase map.

II-1.2   Harmonic vibration measurements with CW ESPI

Assume that during a TV field a plane object vibrates at a sinusoidal frequency ω about a mean position with a periodic out-of-plane displacement $d(x,y,t)=a(x,y)cos(\omega t+\varphi(x,y))$, where $a(x,y)$ and $\varphi(x,y)$ are the amplitude and the phase of the vibration point (x,y). In such a case, the vibration optical interference phase becomes $\phi(x,y,t)=2k\,a(x,y)cos(\omega t+\varphi(x,y))$. Then the intensity at the CCD at time t is, using Eq. (II-4),

$$I(t,x,y) = I_o(x,y) + I_r(x,y) + 2\sqrt{I_o(x,y)I_r(x,y)}\cos[\psi(x,y) + 2ka(x,y)\cos(\omega t + \varphi(x,y))]. \qquad \text{(II-11)}$$

If the scanning time of the CCD is much greater than the period of vibration ($\tau=1/f=2\pi/\omega$), then the CCD will detect a continuous distribution of frozen interference patterns given by Eq. (II-11), corresponding to the object at various points in its vibration cycle. Under these conditions the actual intensity for each TV field is the average of $I(t,x,y)$ over the period τ [27,28]:

$$\bar{I}(x,y) = \bar{I}_o(x,y) + \bar{I}_r(x,y) + 2\sqrt{\bar{I}_o(x,y)\bar{I}_r(x,y)}\cos[\psi(x,y)]J_o[2ka(x,y)], \qquad \text{(II-12)}$$

Since this expression is modulated by a zero order Bessel function it is not suited to computer processing because the visibility of the higher-order fringes falls off rapidly. Furthermore, the resulting fringes represent only the amplitude and not the phase of the vibration. Following, it is mentioned how the use of pulsed lasers allows us to compensate for these disadvantages.

II-1.3   Pulsed ESPI

By using pulsed and stroboscopic light sources [29,30,31], freezing of the movement of the object enables us to measure large amplitude periodic displacements. In recent work [32,33,34], Nd:YAG and ruby lasers made possible the application of pulsed illumination sources operating at frequency rates of 50 Hz.

II-1.3.1   Fringe formation
When the movement of an object is frozen in time, the time-dependence of Eq. (II-11) is dropped and the previous analysis for static load holds for both subtraction and addition patterns [9], see Fig. II-5. Top line of Fig. II-5 shows the TV field rate represented by the CCD vertical synchronization signal. The second line shows the object motion at a particular point. The

periodic output of a pulsed laser is shown on the third line of Fig. II-5.
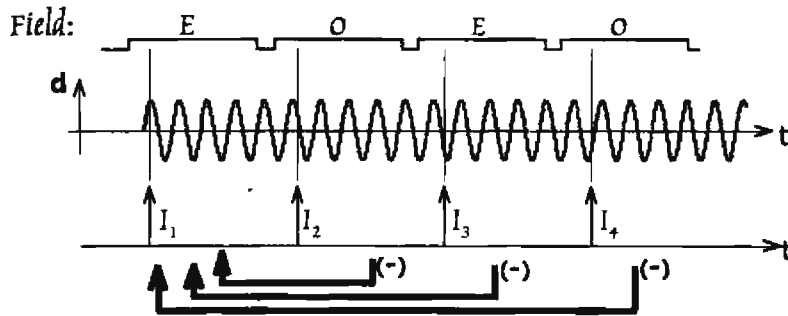
Fig. II-5. Subtraction pulsed ESPI. Top line: CCD rate; second line: Object displacement; bottom line: Pulsed laser output. I_1 is taken as the reference state. E and O stand for even and odd fields respectively.

Taking the reference displacement at $t=0$, subtraction of expressions of the type of Eq. (II-11) gives

$$I_{Sub}(x,y) = 4\sqrt{I_o I_r}\left|\sin\left[\psi + \frac{1}{2}(\Delta\psi_2 + \Delta\theta_2) + 2ka\cos[(\phi_1 + \phi_2)/2]\cos[(\phi_2 - \phi_1)/2]\right]\right| \times$$

$$\left|\sin\left[\frac{1}{2}(\Delta\psi_2 + \Delta\theta_2) + 2ka\sin[(\phi_1 + \phi_2)/2]\sin[(\phi_2 - \phi_1)/2]\right]\right|,$$

(II-13)

where the (x,y) dependence of all variables has been omitted. Here ϕ_1 and ϕ_2 represent the phase at a particular point in two consecutive fields, e.g. I_1 and I_2 in Fig. II-5, $\Delta\psi_2$ takes into account the rigid-body motion of the object between both acquisitions and $\Delta\theta_2$ is a phase term included between pulses for phase-stepping. Eq. (II-13) represents fringes corresponding to contours of constant displacement of the object between consecutive pulses, such as those produced from pulses 1 and 2 in Fig. II-5. These fringes can be formed if and only if the phase change due to rigid-body motion, $\Delta\psi_2$, is not sufficiently large to decorrelate the speckle patterns [30]. Since the time separation between consecutive TV fields is about 16.7 ms, this approach is still susceptible to instabilities, such as rigid-body motion and environmental disturbances. To reduce this effect, two single pulses are fired on both sides of the transfer period of the CCD [35-40], see Fig. II-6. The shortest time between pulses is therefore given by the type of CCD that is being used; for an interline-transfer CCD that time is ~1 μs, and ~300 μs for a frame transfer CCD. The greater drawback for this method is that we cannot measure deformations less than the transfer gate
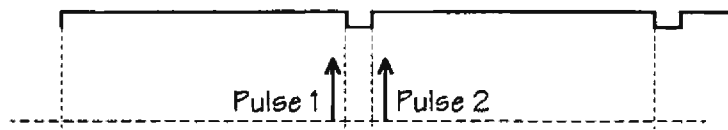
period.

Fig. II-6. Double-pulse subtraction. The separation between pulses is limited by the gate-transfer period (distance between dashed vertical lines).

On the other hand, by adding two phase-referenced intensity patterns on the camera sensor (see Fig. II-7), the resulting fringe pattern is expressed by

$$I_{Add}(x,y) = 2(I_o + I_r) + 4\sqrt{I_o I_r} \cos\left[\psi + \frac{1}{2}(\Delta\psi_2 + \Delta\theta_2) + 2ka\cos[(\phi_1 + \phi_2)/2]\cos[(\phi_2 - \phi_1)/2]\right] \times$$
$$\cos\left[\frac{1}{2}(\Delta\psi_2 + \Delta\theta_2) + 2ka\sin[(\phi_1 + \phi_2)/2]\sin[(\phi_2 - \phi_1)/2]\right].$$

(II-14)

The fringe pattern so obtained has poor contrast due to the additive noise represented by the first term of Eq. (II-14). Despite this, this is the most attractive method to be used in the presence of large amount of noise because we can make the separation between pulses arbitrarily small. Thus, many attempts to improve the quality of the fringes obtained by addition have been proposed [2,9,41-47,70]. Elimination of noise from the reference beam is one alternative for in-line focused image arrangements. For such cases, the reference beam is spatially filtered and the resulting correlation fringes are filtered using a high-pass filter [2.9]. If the spatial filtering is not possible because of high levels of pulsed intensity at the focal plane, the reference beam can be extracted from a preamplification stage of the laser system, ensuring better spatial quality [2.12].
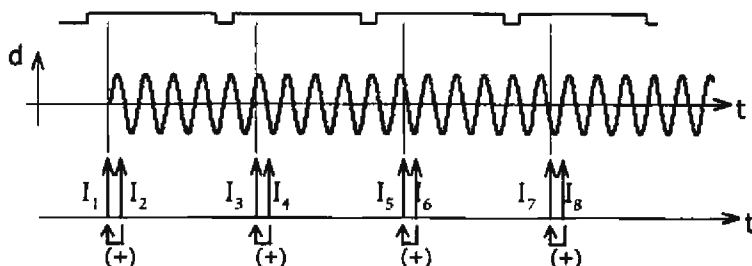
Fig. II-7. Addition pulsed ESPI. Top line: CCD rate; second line: Object displacement; bottom line: Double-pulsed laser output. $I_{1,3,5,7}$ are taken as the reference states. Separation between consecutive pulses (I_1-I_2), (I_3-I_4), (I_5-I_6), (I_7-I_8) is assumed to be constant.

As in the preceding section, the phase calculation may be carried out by means of a 4-step algorithm by POD, as it was shown in Fig. II-5. It is noticed that during at least 4 fields (4*16.7 ms) the object must remain unchanged and external disturbances kept to a minimum so as to calculate correctly the optical phase. Consequently, this procedure can not be employed to measure rapid transient events. This problem is analyzed in the following section.

II-1.3.2 Synchronization

To maintain a stationary fringe pattern in each camera field, the laser pulses are synchronized with the object vibration. In Figs. II-5 and II-7, there is no synchronization, the displacement between consecutive pulses is variable, and a stationary fringe pattern will not be observed neither in real-time subtraction nor in real-time addition. Fig. II-8 shows synchronization between the object motion and the firing of the Q-switched pulsed lasers for subtraction and addition, parts a) and b). Since the deformation is constant, by introducing a phase step between acquisitions, the optical phase can be extracted. Similarly, in part c) and d) the laser is fired at different deformation states but in this case there is a constant delay between consecutive pulses that enables us to observe an animated version of the harmonic motion on the monitor [33,48]. This situation will only be present if the object vibration frequency is close to a multiple of the CCD frame rate. Otherwise, each camera field will display a different fringe pattern.
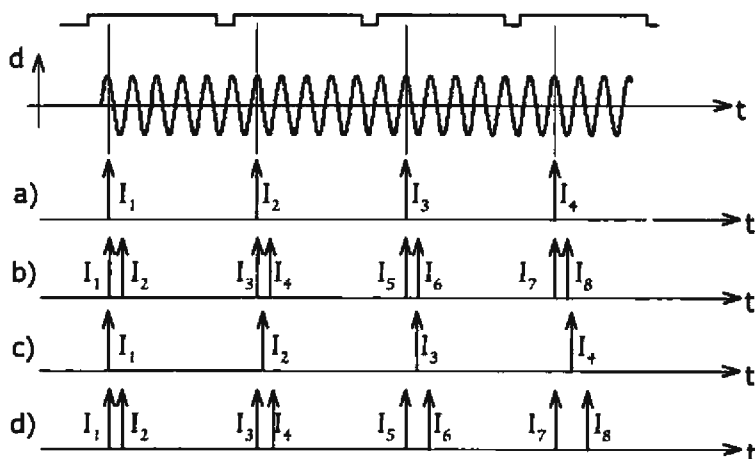
Fig. II-8. Synchronization of the object motion and the firing of Q-switched pulses. a), b) Stationary fringe patterns in real-time subtraction and real-time addition. c), d) Animated version of the harmonic displacement (real-time subtraction and live addition).

The laser must also be synchronized with the CCD camera whenever one pulse per field (or one double-pulse, in the addition case) is anticipated. This avoids observing dark fields in which no

laser pulses appear and bright fields when two or more pulses occur. A synchronization circuit sends a single pulse to the laser corresponding to the first object maximum occurring in each field. Subsequent maxima in the field are ignored until the start of the next field [9].

II-2   Spatial phase-stepping

II-2.1 Introduction

Temporal techniques for phase calculation consist of N steps in time. This means that they require a certain time to be done, e.g. the 4-step technique takes 4*16.7 ms. They are therefore susceptible to external disturbances when their frequencies are close to the CCD rate and measurements of transient events cannot be carried out. In connection with this problem, spatial techniques have been developed. In this case, the acquisitions are carried out simultaneously in time but located at N different spatial positions and along the same optical path. However, detectors with better resolution are required than those used with temporal techniques, because at least three interferograms are acquired in the same sensor [49-54,39]. We may use as many low-resolution detectors as the number of spatial steps, but this would represent an additional source of errors due to calibration [31,55-60]. Many different optical elements enable us to obtain N steps simultaneously. Among these we may mention: polarization elements [55,56,58], diffraction gratings [32,49-54,59], delay plate structures [57,60], and computer-generated holograms (CGHs) [61]. These methods have a lower accuracy than that obtained for temporal methods because a larger source of errors are present, namely phase errors arising from detector nonlinearities, incorrect rotation of polarizer-analyzer, detector miscalibration, intensity normalization, pixel mismatch, etc.

II-2.2   Polarization techniques

The heterodyne technique is a temporal technique based on a polarization two-beam interferometer with rotating wave plates. The object and reference beams have orthogonal linear or circular polarizations. Rotating wave plates or rotating analyzers will produce a frequency shift of the interferometer output at a multiple of the frequency of the rotating elements. Its analysis can be carried out using Jones calculus [62]. The interference phase is electronically calculated by comparison with a reference point [63-68]. The main disadvantage of this method is the use of bulky polarization parts, electro-optical devices and rotating mechanical elements. Furthermore, these techniques usually measure phase with electronics at a single image point. In order to measure over an area, a scanning detector must be used.

We can implement spatial phase shifting using polarization techniques [56,58]. In [56], four signals in quadrature, separated 90° in phase, were obtained. Fig. II-9 shows a top view of the configuration they used. After the polarizing beam splitter (PBS) we obtain the reference and the object beams (orthogonally polarized) after the half wave plate, which is oriented at +22.5° (ccw) with respect to the x-axis, as: $E_{ref} = \frac{a_r}{\sqrt{2}} [+1,-1]^T e^{-i(\omega t + \pi/2)}$, and $E_{obj} = \frac{a_o}{\sqrt{2}} [1,1]^T e^{-i(\omega t - \psi + \pi/2)}$, where ψ is the optical phase between the two beams. Therefore, this element rotates the polarizations so that they are at 45° to the axes of the PBS located before the CCD. The intensities at CCD1, CCD2, CCD3, and CCD4 are, $I_1 = T(E_{ref} + E_{obj})$, $I_2 = R(E_{ref} + E_{obj})$, $I_3 = TQ(45)(E_{ref} + E_{obj})$, and $I_4 = RQ(45)(E_{ref} + E_{obj})$, i.e.,

$$I_1 = \tfrac{1}{2}(a_r^2 + a_o^2) + a_r a_o \cos\psi, \qquad I_2 = \tfrac{1}{2}(a_r^2 + a_o^2) + a_r a_o \cos(\psi + \pi), \qquad (\text{II-15})$$

$$I_3 = \tfrac{1}{2}(a_r^2 + a_o^2) + a_r a_o \cos(\psi + 3\pi/2), \qquad I_4 = \tfrac{1}{2}(a_r^2 + a_o^2) + a_r a_o \cos(\psi + \pi/2),$$

where T, R and Q represent the Jones matrixes for the transmission and reflection of the PBS and the quarter wave plate [62], respectively. Apart from some normalizing factors, Eq. (II-15) represent four signals separated spatially and by angle. The phase ψ can be now calculated using a four-step phase-shifting method. The main disadvantage of this technique is the use of multiple detectors.
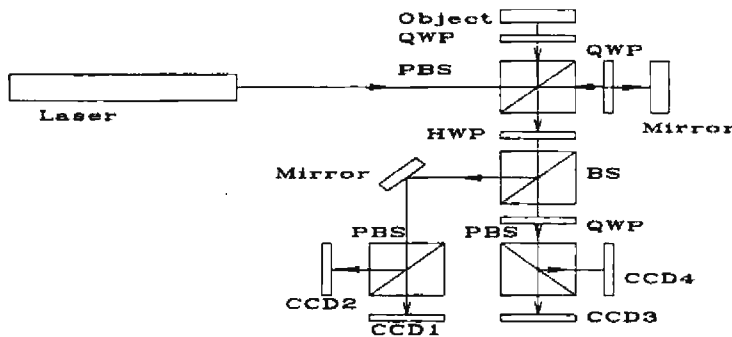
Fig. II-9. Direct phase-measurement interferometer, 4 signals in quadrature are produced.

II-2.3   Grating techniques

Recently, a remarkably simple approach was used for optical phase measurement, using either sinusoidal gratings [31,49-54,59] or CGHs [61]. These elements may serve two purposes. They split an image beam into N copies and may introduce a phase step among the N images. It is not necessary to use a polarizing component. The grating frequency determines the spatial separation of the copies. When a sinusoidal grating is inserted into the object beam, the phase

steps arise from a transverse movement Δx of the grating between consecutive acquisitions, where $\Delta x = \Delta\theta\, d_g/(2\pi)$ with d_g being the grating period and $\Delta\theta$, the required phase step. The N interferograms are generally recorded at different locations on the same detector. When analyzing rapid transient events, the shift of the grating must be done in a very short time, from ms down to ns. Thus, the response time of the moving element (generally a PZT transducer) should be fast enough.

In [61], by using a CGH, four phase steps have been obtained in parallel without any other external phase modulation of the reference path in a Twyman-Green interferometer. If both amplitude and phase are included in the design of the CGH, tilts of the hologram and inhomogeneities of the substrate thickness become critical. As a consequence, the required phase steps were attained by a relative lateral shift of two identical CGHs, located in the reference and object beams. After superposition of these beams at a quadrant photodiode, the intensities can be read simultaneously and the interference phase extracted. The measurements were made one point at a time.

II-3   Spatial phase step with CGH

In [8,52] the analysis of transient events was restricted to recording in time three interference patterns within a particular reference state, and one interference pattern after deformation. Then by POD the phase was calculated. This procedure can not handle the analysis of object deformation that takes place between two arbitrary epochs during a transient event. The use of gratings relieves this problem, but the separation between acquisitions is restricted by the response time of the moving device (as was explained above).

On the other hand, the use of special CGHs in ESPI (gratings which include phase step in their design) or three consecutive pixel lines [39] enables us to study rapid transient phenomena because no moving device is used; in one CCD field N stepped images of a whole object may be grabbed. In this way, deformation between any two points of a transient event can be calculated by either DOP or POD —both in subtraction mode. In the DOP method, one initial phase map is calculated by means of any phase-shifting algorithm, and after deformation, another phase map is determined. The difference between these two determines the interference phase. On the other hand, in the POD method, the reference intensity image can be any of the reference N-

interference patterns. Once the object is deformed, the corresponding intensities in the N-interference patterns are subtracted from the reference, yielding N stepped fringe patterns. By any phase-shifting algorithm the interference phase is recovered. In the case of addition, as it was already noted, POD is the only method that can be applied. This may be implemented by using a phase-stepped CGH in a reference recording and a non-stepping CGH during a second recording. These techniques are discussed further in **Chapter IV**. However, the technique by Pedrini et al [38] cannot handle with this situation since the phase stepping keeps unchanged during the undeformed and deformed acquisitions.

II-4   References

[01] R. Jones and C. Wykes, *Holographic and Speckle Interferometry: A discussion of the theory, practice and application of the techniques*, CUP, U. K. (1983).

[02] T. J. Cookson, J. N. Butters, H. C. Pollard, "Pulsed lasers in electronic speckle pattern interferometry," Opt. and Laser Tech. **10** 119-124 (1978).

[03] J. E. Greivenkamp, "Generalized data reduction for heterodyne interferometry," Opt. Eng. **23**(4), 350-352 (1984).

[04] Y. Y. Cheng and J. C. Wyant, "Phase shifter calibration in phase-shifting interferometry," App. Opt. **24**(18), 3-49-3052 (1985).

[05] D. W. Robinson and D. C. Williams, "Digital phase stepping speckle interferometry," Opt. Comm. **57**(1) 26-30 (1985).

[06] K. Creath, "Phase-shifting speckle interferometry," App. Opt. **24**(18) 3053-3058 (1985).

[07] A. J. Moore, J. R. Tyrer, and F. Mendoza S., "Phase extraction from electronic speckle interferometry addition fringes," App. Opt. **33**(31) 7312-7320 (1994).

[08] S. Nakadate and H. Saito, "Fringe scanning speckle-pattern interferometry," App. Opt. **24**(14) 2172-2180 (1985).

[09] A. J. Moore and C. Pérez-López. "Fringe enhancement and phase calculations in double-pulsed addition ESPI," J. Mod. Opt., **43** 1829-1844 (1996).

[10] P. Carré, "Installlation et utilisation du comparateur photoélectrique et interférentiel du Bureau International des Poids et Mesures," Metrologia **2,** 13-23 (1966).

[11] D. W. Robinson, "Phase unwrapping methods," in *Interferogram Analysis: Digital fringe pattern measurement techniques*, D. W. Robinson and G. T. Reid, Eds., IOP London 194-229 (1993).

[12] J. E. Greivenkamp and J. H. Bruning, "Phase-shifting interferometry," in *Optical Shop Testing*, D. Malacara (Ed.), Wiley N. Y. 2nd Ed., 501-598 (1992).

[13] K. H. Womack, "Interferometric phase measurement using spatial synchronous detection," Opt. Eng., **23** 391-395 (1984).

[14] A. J. Moore and F. Mendoza S., "Phase demodulation in the space domain without a fringe carrier," Opt. and Lasers in Eng., **23**, 319-330 (1995).

[15] M. Takeda, H. Ina and S. Kobayashi, "Fourier-Transform method of fringe-pattern analysis for computer-based topography and interferometry," J.O.S.A., **72**, 156-160 (1982).

[16] A. J. Moore and C. Pérez-López, "Fringe carrier methods in double-pulsed

addition ESPI," Opt. Comm., Opt., **141**, p. 203-212 (1997).

[17] T. Kreis, "Digital holographic interference-phase measurement using the Fourier-transform method," J.O.S.A., **A3** 847-855 (1986).

[18] W. W. Macy, Jr., "Two-dimensional fringe-pattern analysis," App. Opt. **22**(23) 3898-3901 (1983).

[19] D. Kerr, G. H. Kaufmann, and G. E. Galizzi, " Unwrapping of interferometric phase-fringe maps by the discrete cosine transform," App. Opt. **35**(5) 810-816 (1996).

[20] J. M. Huntley, "Noise-immune phase unwrapping algorithm," App. Opt. **28**(15) 3268-3270 (1989).

[21] M. Servin, D. Malacara, and F. J. Cuevas, "Direct-phase detection of modulated Ronchi rulings using a phase-locked loop," Opt. Eng. **33**(4) 1193-1199 (1994).

[22] Y. Xu and C. Ai, "Simple and effective phase unwrapping technique," SPIE **2003** 254-263 (1993).

[23] J. M. Huntley, "Random phase measurement errors in digital speckle pattern interferometry," SPIE **2544** 246-257 (1990).

[24] D. W. Robinson, "Phase unwrapping methods," in *Interferogram Analysis: Digital fringe pattern measurement techniques*, D. W. Robinson and G. T. Reid, Eds., IOP London 194-229 (1993).

[25] R. M. Haralick, S. R. Stenberg, and X. Zhuang, "Image analysis using mathematical morphology," IEEE Trans. on Pattern Analysis and Machine Intelligence, PAMI-**9**(4), 532-550 (1987).

[26] D. C. Ghilia, G. A. Mastin, and L. A. Romero, "Robust two-dimensional weighted and unweighted phase unwrapping that uses fast transforms and iterative methods," J.O.S.A., A **11** (1) 107-117 (1987).

[27] K. J. Gasvik, Optical Metrology, Wiley & Sons 109-111 USA (1985).

[28] R. K. Erf, "Speckle metrology," Academic Press Inc. 128-129 USA (1978).

[29] P. Hariharan, B. F. Oreb, and C. H. Freund, "Stroboscopic holographic interferometry: measurements of vector components of a vibration," App. Opt. **26**(18) 3899-3903 (1987).

[30] B. F. Pouet, S. Krishnaswamy, "Additive/subtractive decorrelated electronic speckle pattern interferometry," Opt. Eng. **32**(6) 1360-1368 (1993).

[31] O. Y. Kwon, D. M. Shough, and R. A. Williams, "Stroboscopic phase-shifting interferometry," Opt. Lett. **12**(11) 855-857 (1987).

[32] A. Hirai, T. Akatsu, and Y. Horii, "Dynamic motion measurement using digital TV speckle interferometry," SPIE **549** 86-93 (1985).

[33] J. R. Tyrer, "Application of pulsed holography and double pulse electronic speckle pattern interferometry to large vibrating engineering structures," SPIE **599** 181-188 (1985).

[34] W. F. Fagan and R. W. T. Preater, "Video holographic interferometry," SPIE **746** 58-60 (1987).

[35] R. Spooren, "TV-holography using a double pulsed single oscillator Nd:YAG laser; restrictions and possibilities," In Hologram Interferometry and Speckle Metrology, ed. K.A. Stetson & R. J. Pryputnievwicz. Society of Experim. Mech. 260-267 (1990).

[36] R. Spooren, "Fringe quality in pulsed TV holography," SPIE **1508** 118-127 (1991).

[37] R. Spooren, "Double-pulse characteristics of a single-oscillator Nd:YAG laser affecting its performance in TV holography," App. Opt. **31**(2) 208-216 (1992).

[38] R. Spooren, "Double-pulse subtraction TV holography," Opt. Eng. **31**(5) 1000-1007 (1992).

[39] G. Pedrini, B. Pfister and H. Tiziani, "Double pulse-electronic speckle interferometry," J. Mod. Opt. **40**(1) 89-96 (1993).

[40] G. Pedrini and H. Tiziani, "Double-pulse electronic speckle interferometry for vibration analysis," App. Opt. **33**(34) 7857-7863 (1994).

[41] M. C. Shellabear, F. Mendoza S., and J. R. Tyrer, "Processing of addition and subtraction fringes from pulsed ESPI for the study of vibrations," In Hologram Interferometry and Speckle Metrology, ed. K.A. Stetson & R. J. Pryputnievwicz. Society of Experim. Mech. 238-244 (1990).

[42] D. Kerr, F. Mendoza S., and J. R. Tyrer, "Extraction of phase data from electronic speckle pattern interferometric fringes using a single-phase-stepped method: a novel approach," J.O.S.A. A **7** 820-826 (1990).

[43] F. Mendoza S., M. C. Shellaebar, and J. R. Tyrer, "Whole field in-plane vibration analysis using pulsed phase-stepped ESPI," App. Opt. **30**, 717-721 (1991).

[44] F. Mendoza S., A.. J. Moore, J. R Tyrer, and N. Alcala O., "Noise reduction in twin-pulsed addition electronic speckle pattern interferometry fringe patterns," Opt. Eng. **33**(5) 1712-1716 (1994).

[45] G. H. Kaufmann, D. Kerr and A. Halliwell, "Contrast enhancement of pulsed ESPI addition fringes," Opt. and Lasers in Eng. **20** 25-34 (1994).

[46] A. Davila, D. Kerr, and H. Kaufmann, "Digital processing of electronic speckle interferometry addition fringes," App. Opt. **33**(25) 5964-5969 (1994).

[47] G. A. Slettemoen, "General analysis fringe contrast in electronic speckle pattern interferometry," Opt. Acta **26**(3), 313-327 (1979).

[48] F. Mendoza S., J. R. Tyrer, T. C. West, and D. Kerr, "Vibration analysis using phase-stepped pulsed electronic speckle pattern interferometry," SPIE **1084** 262-278 (1989).

[49] O. Y. Kwon, "Multichannel phase-shifted interferometry," Opt. Lett. **9** 59-61 (1984).

[50] O. Y. Kwon and D. M. Shough, "Multichannel grating phase-shift interferometers," SPIE **599** 273-279 (1985).

[51] M. Kujawinska and D.W. Robinson, "Multichannel phase-stepped holographic interferometry," App. Opt. **27**(2) 312-320 (1988).

[52] M. Kujawinska, A. Spik, and D. W. Robinson, "Analysis of ESPI interferograms by phase stepping techniques," in *Proceedings of the Fourth International Conference on Fringe Analysis* (Fringe Analysis Special Interest Group, Loughborough University, UK, 1989).

[53] L. Salbut and K. Patorski, "Polarization phase shifting method for moire interferometry and flatness testing," App. Opt. **29**(10) 1471-1473 (1990).

[54] T. D. Upton and D. W. Watt, "Optical and electronic design of a calibrated multichannel electronic interferometer for quantitative flow visualization," App. Opt. **34**(25) 5602-5610 (1995).

[55] A. J. P. Haasteren and H. J. Frankena, "Real-time displacement measurement using a multicamera phase-stepping speckle interferometer," App. Opt. **33** 4137-4142 (1994).

[56] R. Smythe and R. Moore, "Instantaneous phase measuring interferometry," Opt. Eng. **23** 361-364 (1984).

[57] V. Greco, C. Iemmi, S. Ledesma, A. Mannoni, G. Molesini, and F. Quercioli, "Multiphase homodyne displacement sensor," Optik **97**(1) 15-18 (1994).

[58] N. Bareket, "Three-channel phase detector for pulsed wavefront sensing," SPIE **551** 12-16 (1985).

[59] L. Salbut, K. Patorski, and M. Kujawinska, "Polarization approach to high-

sensitivity moiré interferometry," Opt. Eng. **31**(3) 434-439 (1992).

[60] V. Greco, C. Iemmi, S. Ledesma, G. Molesini, and F. Quercioli, "Multiphase homodyne interferometry: analysis of some error sources," Appl. Opt. **34**(13) 2207-2213 (1995).

[61] M. Deininger, L. Wang, K. Gerstner, and T. Tschudi, "Optical phase step method for absolute ranging interferometry using computer-generated holograms," App. Opt. **34** 5620-5623 (1995).

[62] R. C. Jones, "A new calculus for the treatment of optical systems," J.O.S.A. **31** 488-493 (1941).

[63] R. Crane, "Interference phase measurement," App. Opt. **8** 538-542 (1969).

[64] G. E. Sommargren, "Up/down frequency shifter for optical heterodyne interferometry," J.O.S.A. **65** 960-961 (1975).

[65] R. N. Shagam and J. C. Wyant, "Optical frequency shifter for heterodyne interferometers using multiple rotating polarization retarders," App. Opt. **17** 3034-3037 (1978).

[66] M. P. Kothiyal and C. Delisle, "Optical frequency shifter for heterodyne interferometry using counterrotating wave plates," Opt. Lett. **9** 319-32 (1984).

[67] H. Z. Hu, "Polarization heterodyne interferometry using a simple rotating analyzer. 1. Theory and error analysis," App. Opt. **22** 2052-2056 (1983).

[68] K. Creath, "Temporal phase measurement methods," in *Interferogram Analysis: Digital fringe pattern measurement techniques*, D. W. Robinson and G. T. Reid, Eds., IOP London 94-140 (1993).

[69] A. Davila, D. Kerr and G. H. Kaufmann, "Fast electro-optical system for pulsed ESPI carier frige generation", Opt. Comm. **123**(1) 457-464 (1996).

[70] A. Davila, D. Kerr and G. H. Kaufmann, "Digital processing of electronic speckle pattern interferometry addition fringes", App. Opt. **13**(25) 5964-5969 (1994).

[71] G. E. Sommargren, "Double exposure holographic interferometry using common path reference waves", App. Opt. **16**(6) 1736-1741 (1977).

[72] Sciamarella C. A., "a numerical technique of data retrieval form moie or photoelastic patterns", Pattern Recognition Studies, SPIE **18**, 92-101 (1969).

[73] D. Malacara, M. Servín, Z. Malacara, *Interferogram analysis for optical testing*, Marcel Dekker Inc., U. S. A. (1998).

Chapter III   Design and performance of a computer-generated hologram

In this chapter, the design and use of a Computer-Generated Hologram (CGH) are discussed. In a first approximation, our CGHs consist of two crossed gratings that produce four far-field diffraction orders around the order zero. These components are of fundamental importance to the techniques that we are investigating. Their analysis and characterization are complemented in **Appendix C**.

We have also included a review of the methods for designing CGHs and some basic examples that help us understand the fabrication of these optical elements. The CGHs that we have used were made at **The Institute of Applied Physics, Darmstadt, Germany**.

III-1   Introduction

A CGH transforms by diffraction an input light beam into a pre-established light distribution at an image plane, as shown in Fig. III-1. If the diffractive structure is used on-axis (in-line), the intensity distribution is expected to fall around the optical axis. The manufacturing process of CGHs requires ['] maximum optical efficiency and a simple fabrication method. The former requirement leads to phase structures, and to satisfy the latter, stepped (digital or discrete) surface-relief structures are selected.
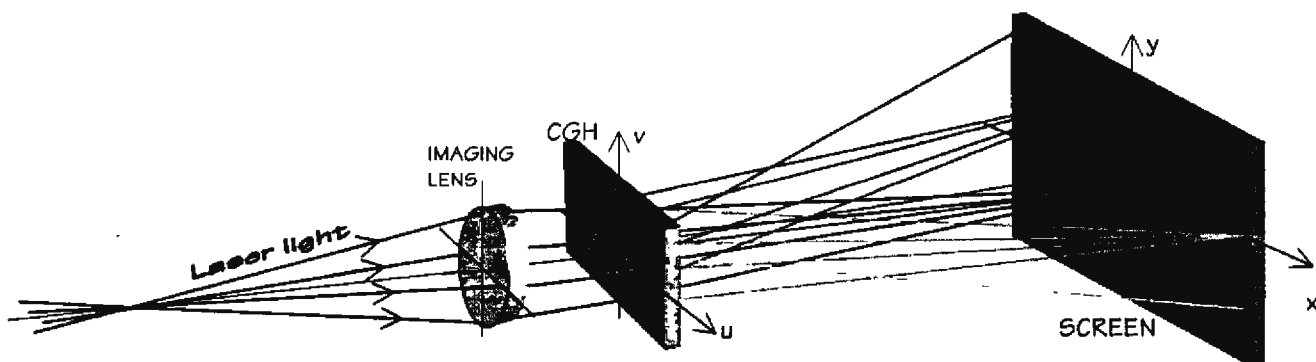
Fig. III-1. A CGH is designed in accordance with a predefined intensity distribution at the image plane (screen). In general, the CGH is designed such that the order zero does not carry any light.

The calculation of the structure that gives rise to a pre-established light distribution at the image

plane is a problem that has not been solved analytically. When analytical methods fail, it is often possible to use iterative methods [2]. However, these methods do not guarantee a global solution, that is, they do not yield a unique error minimization function [3]. In Fig. III-1, the intensity distribution at the screen represents the desired field distribution, which can be represented by

$$b(x,y) = \sum_{m=1}^{M}\sum_{n=1}^{N} a_{mn} e^{i\phi_{mn}} \delta(x - x_m, y - y_n) \, , \tag{III-1}$$

where $b(x,y)$ is a complex-valued amplitude field, δ_{mn} is the Kronecker delta symbol, a_{mn} is the sampled amplitude containing the image information and ϕ_{mn} is the phase function. Here (x_m, y_n) is the position of the (mth,nth) spot of the sampled 2D image (image in Fig. III-1 is MxN=3x3). The field distribution $B(\chi,\xi)$ at the grating plane is related to the field $b(x,y)$ by a Fourier transform:

$$\Im\{b(x,y)\} = B(\chi,\xi) e^{i\psi(\chi,\xi)} = \int_{-\infty}^{\infty}\int_{-\infty}^{\infty} b(x,y) e^{-i\frac{2\pi}{\lambda\zeta}(x\chi + y\xi)} dx\,dy$$

$$= \sum_{m=1}^{M}\sum_{n=1}^{N} a_{mn} e^{i\phi_{mn}} e^{-i\frac{2\pi}{\lambda\zeta}(x_m\chi + y_n\xi)} \, , \tag{III-2}$$

where $\lambda\zeta$ is a scale factor that relates the CGH-to-screen distance and the wavelength of the light used in the reconstruction of the image, (χ,ξ) are the coordinates in the frequency domain at the CGH position. The coordinates (u,v) at the CGH plane are related to the spatial frequencies (χ,ξ) by $u=\lambda f\chi$ and $v=\lambda f\xi$, where f is the focal distance of the imaging lens, so $\zeta\approx f(m+1)$, with m denoting the magnification of the imaging lens. Thus the separation between the centers of two adjacent diffraction orders is given by $s_x=\lambda f/\delta u$ and $s_y=\lambda f/\delta v$, where δu and δv denote the grating periods in the u- and v-directions, respectively.

In order to reconstruct $b(x,y)$, the structure of the phase structure should be proportional to $|B(\chi,\xi)|$. Since $b(x,y)$ and $B(\chi,\xi)$ are spatial limited (e.g., $b(x,y)$ is identically zero outside a particular region), a bandlimited solution cannot be attained; hence the CGH structure will be at most an approximation to $B(\chi,\xi)$. In order to obtain the highest efficiency, which is defined as the ratio of the diffracted light-power in N central diffraction orders to the light-power of the illuminating beam [1], a phase element is chosen [1-6] and the amplitude distribution at the CGH is clipped to $B(\chi,\xi)=const$. This latter assumption introduces further errors to the reconstructed image. There

exist several methods that enables us to obtain the required CGH, binary gratings [4,7], kinoforms [5,8,9], continuous-relief gratings [3,6], phase detour (blaze transmission) gratings [1,4,9] and multilevel structures [1-3,10]. Furthermore, the phase distribution can be computed in accordance with the variable we want to optimize: the minimum of the maxima of the CGH spectrum [11], difference of the light-spots intensity [3], the shape of the basic CGHs cell [7], the phases of point array distributions [6], the quantizing (binarization) effects and clipping of the amplitude [1,2,5], the location of the apertures in a basic cell [1,12], etc. In our case, an iterative input-output method [2] based on a Fourier-transform error-reduction [13] (Gerchberg-Saxton algorithm) was used to compute the desired hologram structure [14]. The Gerchberg–Saxton algorithm was originally used to solve a problem in electron microscopy in which only the modulus of a complex-valued image and the modulus of its Fourier transform were available. The aim was to reconstruct the phase in both the spatial and the frequency domains.

In a reconstruction problem, generally, only partial information in each domain is available. Given limited information (such as the width of the image, the number of quantizing levels, etc) the problem consists of reconstructing either $b(x,y)$ and $B(\chi,\xi)$. In the case of CGHs, only a sampled version of the image and partial information of its Fourier transform are available.

The Gerchberg-Saxton algorithm is explained by the block diagram of Fig. III-2. One iteration proceeds as follows. The initial sampled amplitudes of the image are set to 1 (diffraction orders with identical intensities) with random phase values within the interval π, $-\pi$. An estimate of the image $b(x,y)$ is Fourier-transformed. The phase of the discrete complex function, $\psi(\chi,\xi)$, must accomplish with certain constraints, such as the number of discrete levels. Hence we substitute $\psi(\chi,\xi)$ for $\psi'(\chi,\xi)$, which is the desirable quantized phase at a particular position (e.g. for a binary CGH, the phase values are rounded off to 0 or π). For phase holograms, we set $B(\chi,\xi)=const$. This means that the magnitude is quantized to a single level, i.e. the case of a transparent grating. In this case, the exponential term in Eq. (III-2), $e^{i\psi(\chi,\xi)}$, is called the kinoform of the image $b(x,y)$. Gallagher and Liu [5] explained how the errors arising from quantizing and clipping $B(\chi,\xi)=const$ influence on the error of the actual image and on $k(x,y)$, which is the image calculated from the Fourier transform of $const \cdot \psi'(\chi,\xi)$. This error is calculated as

$$e = \frac{\int\limits_{-\infty}^{\infty} |b(x,y) - h(x,y)|^2 \, dxdy}{\int\limits_{-\infty}^{\infty} |h(x,y)|^2 \, dxdy} \qquad (\text{III-3})$$

Eq. (III-3) provides the criterion for deciding when a solution has been found. This algorithm has been used for other problems, namely spectrum shaping [2], inverse filters [4,10], image reconstruction [2], pattern recognition [4], optical multiplexers [1], color splitters [1], gratings for interferometry [14-19], etc.
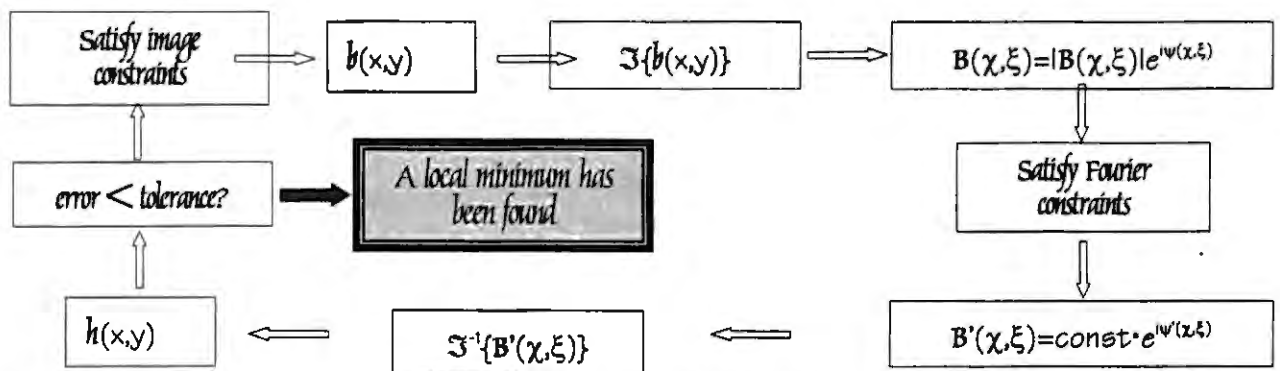
Fig. III-2. Block diagram of the Gerchberg-Saxton algorithm. Here $h(xy)$ approximates $b(xy)$ after amplitude-clipping and quantizing (Fourier-domain constraints, e.g. for a binary grating, two stepped phase values and maximum resolution are desired). Then, $h(xy)$ is further modified so that identical image spots are obtained (image constraints). Since any image phase, ϕ_{mn}, is allowable (within π and $-\pi$), there is an infinity of changes in the output $h(xy)$ that would satisfy it.

The fabrication of the phase structure may be done by several methods. Lohmann [4] plotted $B(\chi,\xi)$ by a gray-scale plotter, in which the size and position of an aperture in a cell accounted for the amplitude and phase, respectively. The gain in brightness is increased 4 times if the phase step is π (binarization, black or white) [4]. The plot was then photographed and bleached, and the thickness of the resulting transparency was proportional to $B(\chi,\xi)$. The surface-relief profile of a binary grating can be made by using microlithographic technology, which is widely known from Very Large-Scale Integration techniques [6,20] (VLSI, which consists of the incorporation of thousands of electronic components on a chip). Several processes and materials (glass, fused silica, silicon nitride, sapphire, silver halide, photoreactive polymers and photoresists) have been

applied in the fabrication of transmission gratings. Reflection-type structures can also be fabricated with the same materials provided that the grating is coated with a thin metal film that can be subjected to chemical etching (chemical removal of material). Fig. III-3 shows a basic design of transmission and reflection binary CGHs according to Dammann [1].
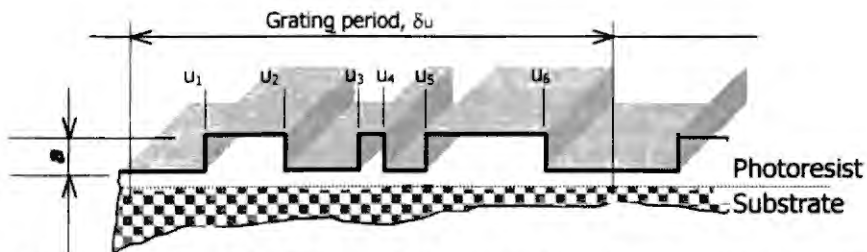
Fig. III-3. Binary phase grating. Each grating period is divided into various sections with alternating geometrical steps. The phase-delays for transmission and reflection are $\varphi=2\pi(n-1)a/\lambda$ and $\varphi=4\pi a/\lambda$ where n is the index of refraction of the photoresist (~1.65), a is the step-height (which corresponds to a phase change of π, and ~5 μm) and λ is the wavelength of the reconstructing light. The CGH phase data is converted into microrelief profile by taking into account the refractive index of the final microstructure and the readout wavelength. In general, glass or fused silica is used as the substrate.

Photoresists are one of the most common materials for surface-relief [21]. Since they are light-sensitive, they can form surface-relief patterns upon exposure and development. There are two types of photoresists, negative and positive. In positive photoresists the exposed areas become soluble as they absorb light so that after development they are dissolved away. In negative ones, the opposite is true, resembling the standard photographic process [21,22]. The choice of photoresists for recording surface-relief structures is based on a tradeoff among sensitivity, resolution capability (~μm) and ease of application and processing. When the resist adheres to the substrate, positive resists are recommended, since they do not have to form cross linkages among their molecules. Common substrates are glass, silicon and quartz. Photoresists are commonly adhered to the substrate by spinning at rates of the order of 1000 rpm as to get a uniform layer. After spinning deposition, adherence is increased by baking at ~120 °C. The most widely studied photoresists are those manufactured by the Shipley Co., Kodak Co., and Afga Co. Their characteristics are described by a change in layer thickness, Δa, caused by exposure E [23]:

$$\Delta a = T(r_1 - \Delta r e^{-\alpha_o E}), \tag{III-4}$$

where T is the development time, α_o is the absorption cross section of the molecule, r_1 represents

the rate of removal (etching) of absorbed molecules during development (nm/s). Furthermore, $\Delta r = r_1 - r_2$, where r_2 is the rate of removal of unexposed portions. In the case of positive photoresists, if E is large then $\Delta a \sim r_1 T$, and the etched material is determined only by the absorbed etch-rate. The uncertainty of the writing process and characterization of the photoresists cause errors in the relief of at least ±6%; this problem affects mainly the uniformity of the intensity distribution of the image [3]. To overcome this problem the idealized phase profile is recorded in photoresist by a step-and-repeat process, where several surface-relief measurements are done during the exposition process.

Cheap replicas of surface-relief structures are obtained by means of photopolimerization (2P process), in which a liquid plastic material (e.g., polymethil methacrylate, PVC, etc) is put onto the surface-relief and hardened. This process may involve embossing or stamping and casting or injection moulding (as in the production of compact disks). After exposing the surface-relief to UV light, it hardens and a negative copy with the same optical properties of the master structure is obtained [6].

III-2   Design

In our case, two different CGHs were designed and fabricated at The Institute of Applied Physics, Darmstadt, Germany. A nonstepping hologram and a stepping hologram were fabricated. The latter incorporates a linear phase step between each field. Both gratings were calculated to produce four images in the far field of an imaging lens and were designed by the Gerchberg-Saxton algorithm. They were made by spinning Shipley S1400-17 negative photoresist onto a glass substrate and exposed to UV light (He:Cd laser) through an amplitude mask. The binary depth was 408 nm for use at 532 nm. When He-Ne light (633 nm) is used, the efficiency of the grating decreases (<20%) because of the considerable residual power in the order zero. The calculated phase delays in the four first orders (quadrants) of the stepping CGH were 0, $\pi/2$, π, $3\pi/2$ radians, starting at the top left-hand corner and proceeding clockwise. In practice, these values may vary due to tilt and in-plane rotation of the hologram. The gratings are therefore mounted such that equal phase steps between fields are obtained. The CGH only needs to be positioned once, when setting up the appropriate geometry.

Lateral displacements of the hologram (Δu, Δv) give rise to phase shifts of the diffracted orders

relative to the order zero, as shown in Fig. III-4, given by [19]:

$$\delta_\chi = 2\pi \frac{\Delta u}{\delta u} \quad and \quad \delta_\xi = 2\pi \frac{\Delta v}{\delta v}, \qquad\qquad\qquad (III\text{-}5)$$
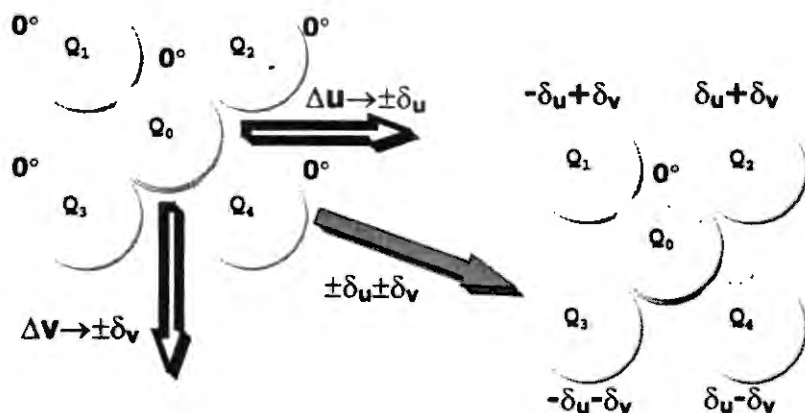
Fig. III-4. Generated phase-stepping after transverse movements of the CGH. Image quadrants are denoted by Q_n. For a stepping CGH, each quadrant has a step phase noted as interferes with a coherent reference beam. By using the Fourier translation theorem, a combination of lateral movements corresponds to an addition of phase steps.

where δu and δv denote the grating spatial periods in the u- and v-directions, and are related to the maximum resolution of the manufacturing process. Should the phase shift be $\pi/2$ in the u-direction, then $\Delta u = \delta u/4$. In **chapter IV, Section IV-3**, we used $\Delta u = \delta u/4$ and $\Delta v = \delta v/8$, so the stepping resulted in $-\pi/4$, $3\pi/4$, $-3\pi/4$, and $\pi/4$. As explained in *Appendix C*, this stepping corresponds to any possible combination of the diffraction orders. As the stepping departs from $\pi/2$ rad (due to misalignment), only one of these combinations will be adequate to the data.

III-3   Usage and performance

The holograms were first characterized by illuminating with collimated light, as shown in Fig. III-5. The two holograms showed similar diffraction divergence. Considering Fig. III-6, objects should be imaged at most 6.6 mm; for example, the largest radius that can be accommodated in the CCD sensor area is 1.375 mm. In **Ch. IV**, a radius of 1.2375 mm was used.
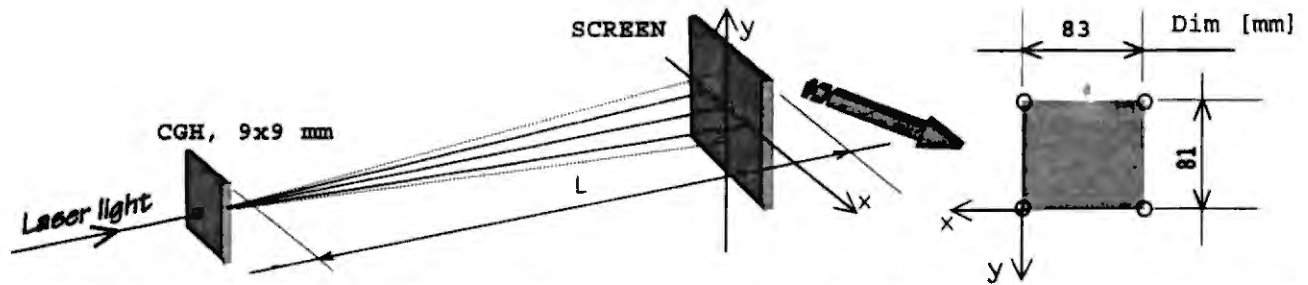
Fig. III-5. Measurement of the CGHs divergence, with L=5936 mm. The CGHs are illuminated with an unexpanded He-Ne beam.
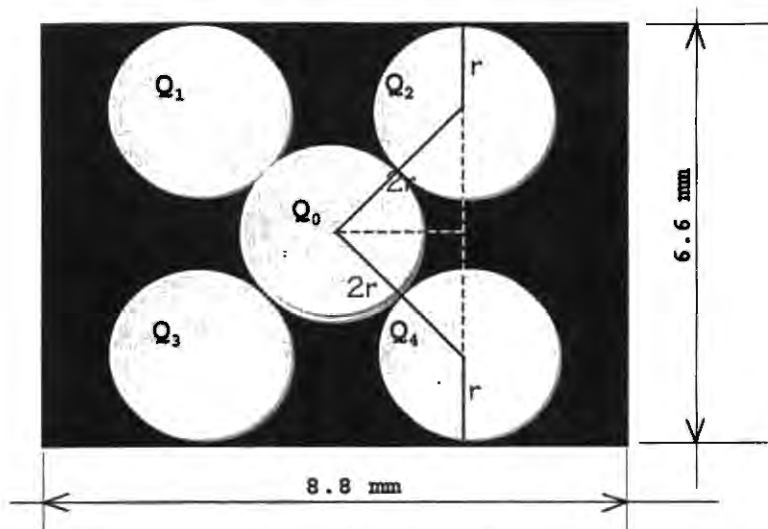
Fig. III-6. Dimensions of CCD (512H480V pixels). The maximum radius r that fits this area is 1.375 mm.

Substitution of the values shown in Fig. III-5 into the grating equation ($\theta=\lambda/\delta u$, where θ is the angle of diffraction and δu the period of the grating), the spatial periods in the u- and v-directions result in 90.5μm and 92.8μm, respectively. If the image at the CCD is kept unchanged, then the CGH-to-screen distance, $L\equiv\zeta$, varies inversely with the wavelength in accordance with the grating equation, i.e. $L_N/L_H=\lambda_H/\lambda_N$ is satisfied for two arbitrary wavelengths, H and N.

The light distribution of an ideal structure is shown in Fig. III-7a. A point light source is assumed. The actual distribution is shown in Fig. III-7b. Note that the zero order is present and that the positions of the diffraction images are asymmetric with respect to lines A, B, C and D and to the center. These errors arise from the manufacturing process of the hologram. Furthermore, it is

noted that the second diffraction orders carry some energy as well.
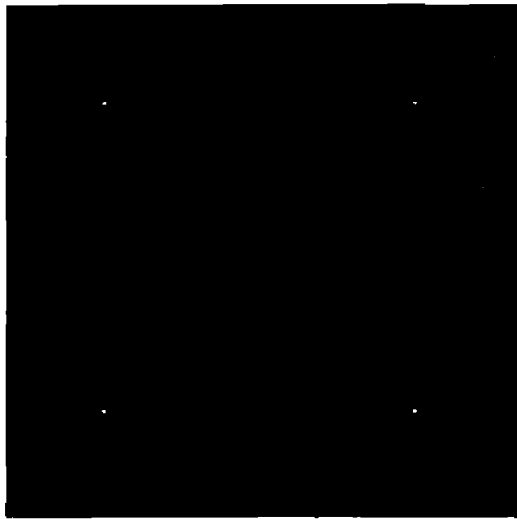
Fig. III-7a)
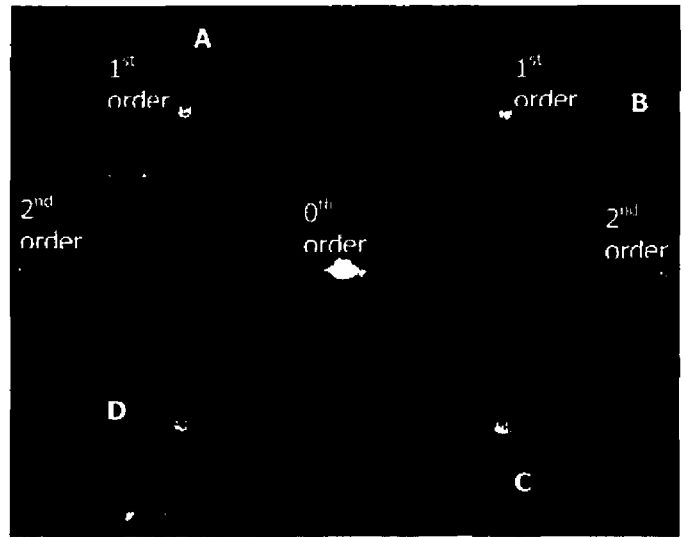
Fig. III-7b)

Fig. III-7. a) Ideal intensity distribution. Absence of zero order. b) Actual light distribution. Two negative lenses and a zoom lens were used with Nd:YAG light. Notice the presence of the zero and second orders.

A very simple example of the required CGHs structure is presented in Fig. III-8. In obtaining this image, first the light distribution shown in Fig. III-7a is multiplied by a Gaussian filter [24] and propagated backwards a distance $\zeta=246$ mm. The result is then Fourier transformed. After transforming, the amplitude and phase of the light at the hologram plane are attained. This represents half an iteration of the diagram in Fig. III-2. Figs. 8a and 8b show this result for a stepping and for a nonstepping CGH, respectively. If we continued with the iterative algorithm explained earlier, this transformed function would then be changed in order to satisfy the frequency-domain conditions, such as constant amplitude and discrete phase values. To complete one iteration, we would get the inverse Fourier transform of the latter function and propagate it forwards. The resulting image distribution would be made satisfy the image constraints, such as identical amplitude diffraction orders, and arbitrary phase for a nonstepping CGH or different phase values between the four orders for a stepping CGH. This process would be repeated until a system solution was found. In Fig. III-8, both the spatial and frequency domains were divided into 128x128 pixel cells. Notice that their intensity profiles are different. Both structures have 100x100 intensity peaks. The actual holograms have 98 spatial periods.
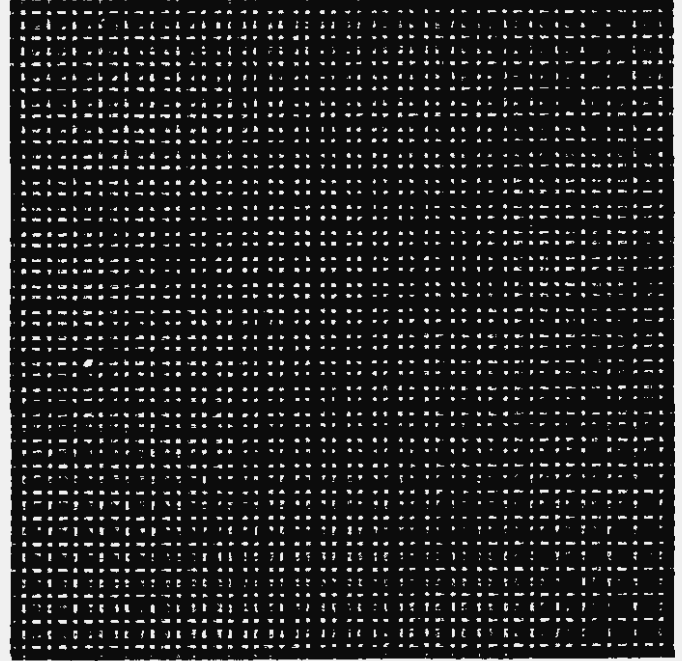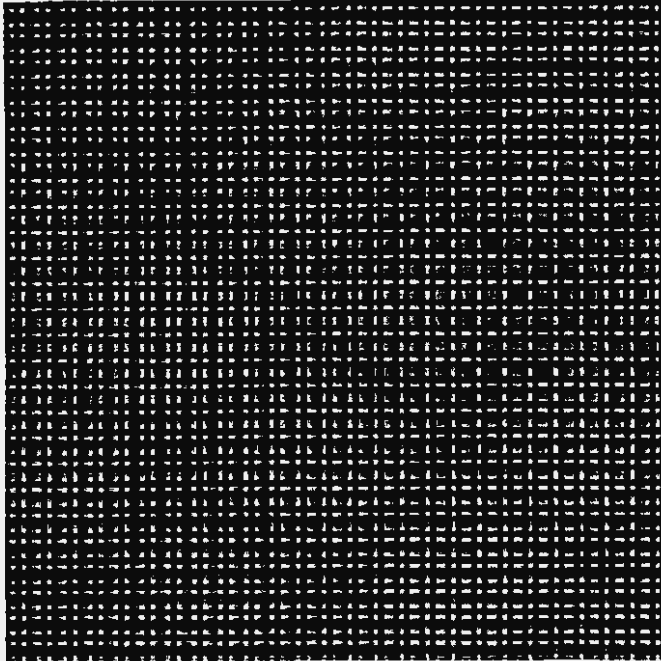
Fig. III-8a)   **Fig. III-8b)**

Fig. III-8. Ideal hologram structures. Only the magnitude is shown. a) Stepping CGH. b) Nonstepping CGH. Number of cells = 128x128, 255 gray levels or equivalently 255 stepped surface-relieves for a phase hologram.

III-4   References

[01] H. Dammann, "Synthetic digital-phase gratings –design, features, applications," SPIE **437** International Conference on Computer-Generated Holography, 72-78 (1983).

[02] J. R. Fienup, "Iterative method applied to image reconstruction and to computer-generated holograms," Opt. Eng. **19**(3) 297-305 (1980).

[03] D. Daly, S. M. Hodson and M. C. Hutley, "Fan-out gratings with a continuous profile," Opt. Comm. **82**(3) 183-187 (1991).

[04] A. W. Lohmann and D. P. Paris, "Binary Fraunhofer Holograms, generated by computer," App. Opt. **6**(10) 1739 1748 (1967).

[05] N. C. Gallagher and B. Liu, "Method for computing kinoforms that reduces image reconstruction error," App. Opt. **12**(10) 2328-2335 (1973).

[06] M. T. Gale, M. Rossi, H. Schütz, P. Ehbets, H. P. Herzig, and D. Prongué, "Continuous-relief diffractive optical elements for two-dimensional array generation," App. Opt. **32**(4) 2526-2533 (1993).

[07] A. Vasara, M. Taghizadeh, J. Turunen, J. Westerholm, E. Noponen, H. Ichikawa, J. M. Miller, T. Jaakkola, and S. Kuisma, "Binary surface-relief gratings for array illumination in digital optics," App. Opt. **31**(17) 3320-3336 (1992).

[08] D. Prongué, H. P. Herzig, R. Danliker, and M. T. Gale, "Optimized kinoform structures for highly efficient fan-out elements," App. Opt. **31** 5706-5711 (1992).

[09] M. Larsson, M. Ekberg, f. Nokolajeff, and S. Hard, "Successive development of

resist kinoforms manufactured with direct-writing, electron-beam lithography,"
App. Opt. **33**(7) 1176-1179 (1994).

[10] F. Wyrowski, "Digital phase-encoded inverse filter for optical pattern
recognition," App. Opt. **30**(32) 4650-4657 (1991).

[11] J. P. Allebach and B. Liu, "Minimax spectrum shaping with a bandwidth
constraint," App. Opt. **14**(12) 3062-3072 (1975).

[12] B. R. Brown and A. W. Lohmann, "Computer-generated binary holograms," SPIE
Milestone Series *Computer-Generated Holograms and Diffractive Optics*, S. H.
Lee (Ed.) **33** pp. 13-21 (1992).

[13] R. W. Gerchgerg and W. O. Saxton, "A practical algorithm for the determination
of phase from image and diffraction plane pictures," Optik **35**, 237-246 (1972).

[14] M. Deininger, L. Wang, K. Gerstner, and T. Tschudi, "Optical phase step method
for absolute ranging interferometry using computer-generated holograms," App.
Opt. 34(25) 5620-5623 (1995).

[15] K. Patorski, "Generation of the derivative of out-of-plane displacements using
conjugate shear and moire interferometry," App. Opt. **25**(18) 3146-3151 (1986).

[16] O. Y. Kwon and D. M. Shough, "Multichannel grating phase-shift
interferometers," SPIE **599**, 273-279 (1985).

[17] M. Kujawinska and D. W. Robinson, "Multichannel phase-stepped holographic
interferometry," App. Opt. **27**(2) 312-320 (1988).

[18] M. Kujawinska, A. Spik, and D. W. Robinson, "Analysis of ESPI interferograms
by phase stepping techniques," in *Proceedings of the Fourth International
Conference on Fringe Analysis* (Fringe Analysis Special Interest Group,
Loughborough University, UK, 1989).

[19] O. Y. Kwon, D. M. Shough, and R. A. Williams, "Stroboscopic phase-shifting
interferometry," Opt. Lett. **12**(11) 855-857 (1987).

[20] C. A. Spence and R. A. Ferguson, "Some experimental techniques for
characterizing photoresists," SPIE 1466 324-**335** (1991).

[21] K. Lizuka, *Optical Sicences: Engineering Optics*, T. Tamir, Ed., Springer-
Verlag 2nd Ed., Germany (1987).

[22] K. Othmer, Encyclopedia of Chemical Technology, John Wiley & Sons, 2nd Ed. Vol.
15, USA (1968).

[23] R. A. Bartolini, "Photoresists," in *Topics in Applied Physics: Holographic
Recording Materials*, H. M. Smith, Ed., Springer-Verlag, Vol. 20, Germany
(1977).

[24] R. Y. Chiao, "Scanning tomographic acoustic microscopy," IEEE Transactions on
Image Processing **4**(3), 358-369 (1995).

Chapter IV   Implementation. Proofs of method

This chapter contains the results related to the use of CGHs in conjunction with a CW laser. The CGHs diffract the light into four copies. One of the CGHs corresponds to a modified phase grating that does not need to be translated in order to introduce a phase step between diffracted fields. A single CCD detector records the four image copies. All the information needed to analyze a phase-referenced speckle pattern is available in any TV field.

Measurements of out-of-plane rotation of a 45-mm aluminum disk are included. The rotations are of the order of a few seconds of arc. The precision (3 times the rms error) is about **0.15λ**, or equivalently, a fraction of a second of arc for our setup.

Experimental results related to the dynamics of a plume stemming from a soldering iron confirm the utility of the method and its potential to be applied in transient ESPI.

IV-1   Introduction

In this chapter, we describe a new spatial phase-stepping technique. The technique is based on a CGH similar to that used for point range measurements in a Twyman-Green interferometer [1]. In that system, two holograms were calculated to diffract the incident light into four points in the far field. One of the gratings was laterally shifted to produce a phase shift between the four orders. We have used similar holograms but they include phase step Furthermore, full-field deformations are available.

Here, firstly, we used a single nonstepping CGH that served only as a separator of the object beam into four copies, and where the phase-stepping between consecutive copies arises from two simultaneous transverse movements of the CGH, as in [1]. Next, we used a stepping CGH, which apart from diffracting the light into four separate fields it also introduces a phase change between these fields. Thus, in such a case there is no need to transversally move the CGH to introduce a phase change. Finally, operation is also demonstrated by using a nonstepping CGH during a reference acquisition and a stepping CGH in a second one.

All the results presented in this chapter assume the use of a CW He:Ne laser emitting at 632.8 nm. The changing and moving of holograms were implemented by manual control. The main aim was to prove the feasibility of the method.

IV-2   Experimental system

Our system comprises a standard out-of-plane ESPI interferometer, Fig. IV-1. A CW helium-neon laser illuminates a test object, which is imaged by a combination of two identical lenses ($f_1=f_2=-50$ mm) and a SLR zoom lens, to a CCD camera. The sensor is a frame-transfer COHU 4810 CCD with an active imaging area of 8.8mmx6.6mm (TV format 3:4) and an array of 754x488 (HxV) picture elements. Camera scanning is 2:1 interlace (2 fields=1 frame) to EIA RS-170 (60 Hz, 525 lines, 64 μs per line). The gain is not compensated. A frame grabber (VFG) digitizes the input signal using a 512x480 pix image area. This image may be displayed on a compatible monitor with the same format. The vertical blanking period of the CCD is ~300 μs and the horizontal blanking, ~5 μs. Every pixel takes 71.43 ns.
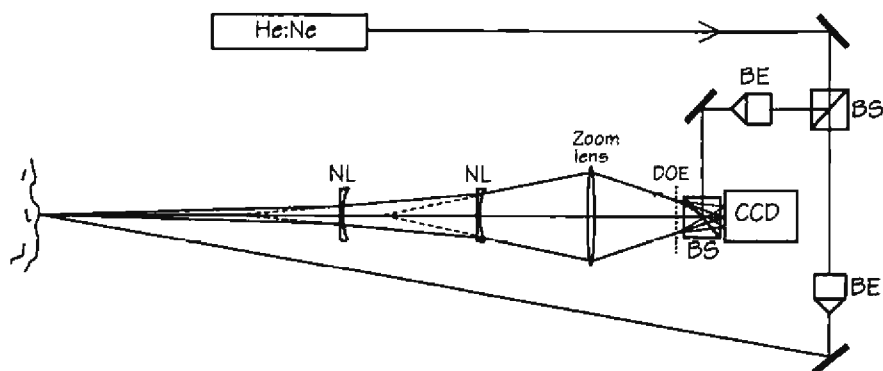
Fig. IV-1. ESPI arrangement with out-of-plane sensitivity. BS: Beam splitter; BE: Beam expander; NL: Negative lens.

Considering the divergence of the ± 1 orders (7.2 mrad), the CCD-to-CGH distance was calculated as 246 mm. For zoom-to-object distances within 1 meter, the object size that can be accommodated on the CCD is 7 mm (no negative lenses), see *Appendix A*. The introduction of two identical negative lenses between the zoom and the object allowed us to reduce the magnification of the system. In this way the optical system was designed by taking into account the object-to-CCD distance, U (Fig. IV-2), which was minimized according to the following expressions:

$$u_1 = u_2 = f_1(\sqrt{\frac{v\, s_o}{u\, s_i}} - 1),$$

$$v_1 = \frac{u_1 f_1}{u_1 + f_1}, \qquad d = \frac{u_1^2}{u_1 + f_1},$$

$$c = u - v_1, \qquad U = u + \frac{2u_1^2}{u_1 + f_1},$$

(IV-1)

Each quadrant image on the CCD covered a 2.475-mm diameter region that is equivalent to a rectangle of 145x181 pix. The zoom lens was modeled as a thin lens (see **Appendix A**), working with a magnification, m, of 1.189 and with a zoom-to-CCD distance, v, of 260 mm. The size of the object, s_o, was 45 mm. Then, U was determined from Eq. (IV-1) as 854.2 mm. Fig. IV-3 shows two sample images at the CCD position using these parameters. As it is explained in **appendix A**, varying distance c implies focussing of the object, whereas a variation of distance d is reflected as a change of the magnification of the system. The addition of the inherent flexibility of the zoom to the latter variations results in a very flexible optical system.
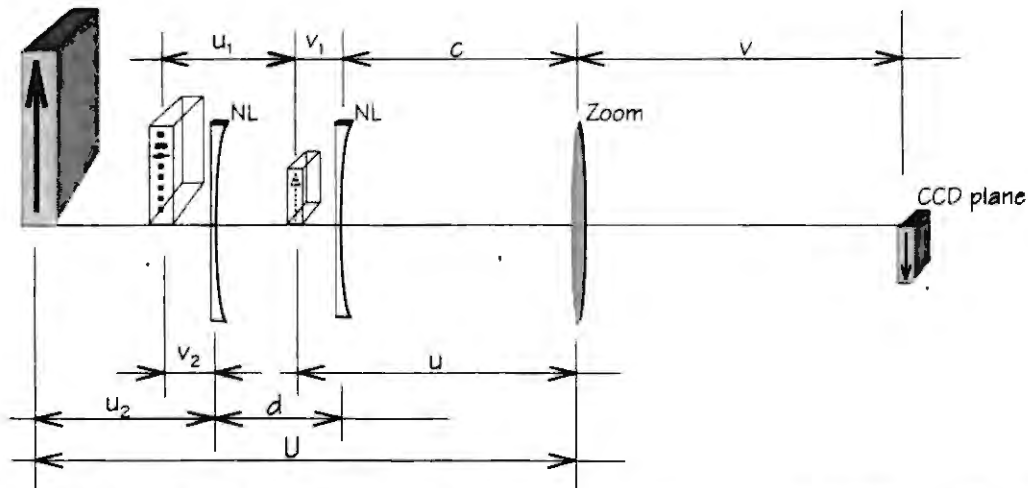
Fig. IV-2. Geometry of the light-collecting system: combination of two negative lenses and zoom lens.

A beamsplitter positioned between the zoom lens and the CCD camera introduces a spherical reference wavefront coherent with the light scattered from the object. The dynamic range of the CCD requires that the sum of the object beam and the reference beam should not exceed the saturation intensity if the camera is not to be overloaded and signal information lost.

The holograms are placed approximately 2 mm behind the rear element of the zoom lens, at this position a slight quantity of astigmatism is originated [2]. The reference beam is expanded and oriented so that it appears to diverge from the center of the viewing aperture [3]. Object and reference beams showed a departure from conjugacy of ±1mm in the transverse direction and ±7 mm along the optical axis when Q_1 (see Fig. IV-3a) was correlated with the rest of the diffraction orders (POD [4], see also Fig. IV-4.) These tolerances are related to the visibility of the fringes and were much more critical for POD than for DOP. In **Chapter V** this topic is treated further. The angle between the object beam and the observation direction was measured as 11°, so every fringe practically represents a displacement of λ/2.
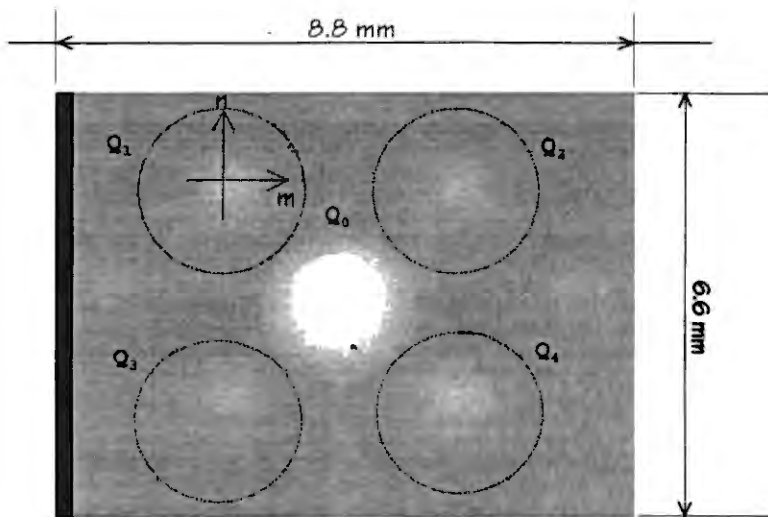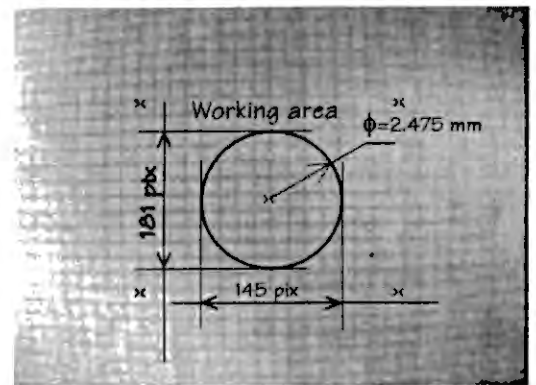
Fig. IV-3a)

Fig. IV-3b)

Fig. IV-3. Two auxiliary images. a) The order zero shows considerable residual power. This image was used to calculate normalization coefficients (see next section). Q stands for quadrant. b) The hologram was removed to check (with white light) correct focussing. It is noted a great deal of barrel aberration at the edges ($m_x/m_y=1.106$). However, in the working area (a 2.475-mm circle in the center) the aberrations are not significant ($m_x/m_y=1.037$). The aspect ratio (4:5) is of shear importance when dealing with TV images.

Following, the three approaches mentioned in the introduction section are analyzed. The first one assumes the use of a nonstepping CGH and transverse movements of the kind described in Ref. 1 for point measurements. The two other methods refer to new methods potentially feasible to be used in transient event measurements.

IV-3   Nonstepping CGH
IV-3.1   Theory

We denote each of the first far-field diffraction orders (quadrant images) by the subscript k. A local coordinate system is assigned to each quadrant image whose origin is at the corresponding center point of each quadrant. The intensity at any pixel (m,n) in the k'th quadrant, for a reference speckle pattern, can be approximated by:

$$I_{ref,k}(m,n) = I_{0,k}(m,n) + I_{R,k}(m,n) + 2\sqrt{I_{0,k}(m,n)I_{R,k}(m,n)}\cos(\psi(m,n)), \tag{IV-2}$$

where $I_0(m,n)$ and $I_R(m,n)$ are the object and reference intensities respectively, and $\psi(m,n)$ is the random phase between them. Here k takes on the values 1, 2, 3, 4. Due to imperfections in the CGH, the light is not equally divided between each of the four first-order diffraction fields. Furthermore, the reference beam intensity may vary over the detector. Thus, $I_0(m,n)$ and $I_R(m,n)$ are measured experimentally in two calibration images from which normalizing factors between the four quadrants are calculated at each pixel. For each CGH, these factors are referenced with respect to Q1 as $K_{0,k} = <I_{0,1}(m,n)>/<I_{0,k}(m,n)>$ and $K_{R,k}(m,n) = I_{R,1}(m,n)/I_{r,k}(m,n)$, where <> denotes the mean value. Then, normalization of Eq. (IV-2) gives

$$I'_{ref,k}(m,n) = \sqrt{K_{0,k}K_{R,k}(m,n)}\,(I_{ref,k}(m,n) - I_{0,k}(m,n) - I_{R,k}(m,n)). \tag{IV-3}$$

Since the reference beam does not pass through the CGH, $K_{R,k}(m,n)$, unlike $K_{0,k}$, is identical for both the nonstepping CGH and the stepping CGH.

At this stage, a correspondence function between pixels of different orders must be found (see *Appendix B*). We have assumed that the orders have the same shape. The shape differences actually are of the order of fractions of pixel, so this represented a negligible source of error.

For a second capture, after introducing two lateral shifts of the hologram in the x- and y-directions (see **Chapter III**), we have

$$I_{def,k}(m,n) = I_{0,k}(m,n) + I_{R,k}(m,n) + 2\sqrt{I_{0,k}(m,n)I_{R,k}(m,n)}\cos\bigl(\psi(m,n) + \phi(m,n) + (k-1)2\alpha\bigr), \tag{IV-4}$$

where 2α corresponds to a constant phase-stepping term between consecutive quadrants (see also **Appendix C**). By obtaining subtraction correlation fringes from Eq. (IV-3) and a normalized version of Eq. (IV-4), POD method, the optical phase $\phi(m,n)$ may be computed by any four-step algorithm using the normalized values $(I'_{def,k} - I'_{ref,k})$, see Fig. IV-4. For this purpose, we chose the Carré algorithm for two reasons, the actual size of the applied phase step does not need to be known and the reference beam may be spherical. Therefore, every pixel has a particular phase step and then is treated as an individual interferometer.

The alignment of the CGH must be kept strictly identical during the time interval of consecutive acquisitions in order to avoid the introduction of phase errors in the calculations. This step was checked by subtracting a reference interference speckle pattern (Eq. (IV-2)) from another recorded after laterally moving the CGH but before applying any deformation, Eq. (IV-4) with $\phi(m,n)=0$. The resulting correlation fringe pattern should not show any carrier fringes.

For transient measurements, this method is limited by the response of the grating moving device in double-pulse addition. This means that if a PZT device is used, analyses of transient events shorter than ~ 200 μs cannot be carried out.
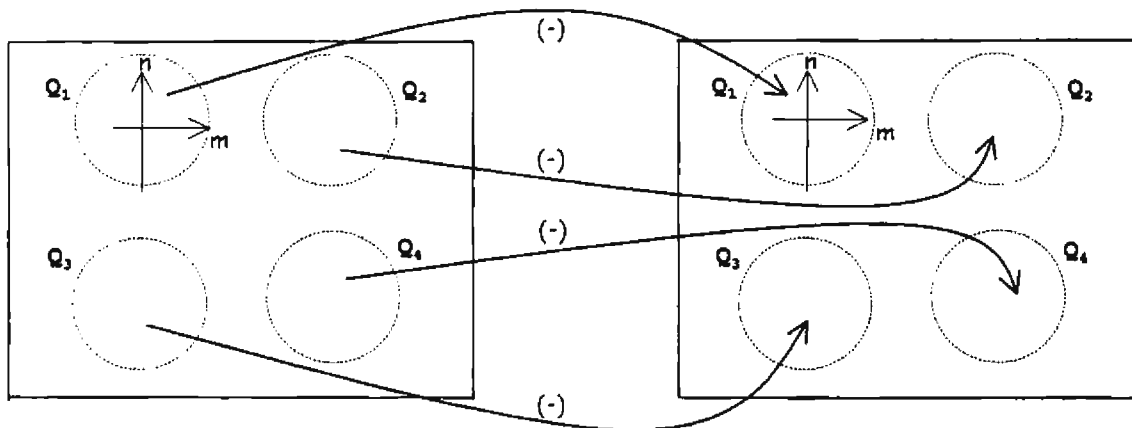
Fig. IV-4. POD subtraction correlation fringes. The left image corresponds to an undeformed state and the right one to a deformation state (subtraction on a quadrant basis, for nonstepping CGH -this section- and combined use of holograms -**Section IV-5.**) A correspondence function between the 4 pairs of quadrants is assumed.

IV-3.2 Experimental results

Figure IV-5a shows a phase-referenced speckle pattern represented by Eq. (IV-2). The low efficiency of the CGH at 633 nm is evident: considerable light energy exists in the order zero as well as to a less extent in the ±2 orders. Software was written to isolate the ±1 diffraction fields. The test object is an aluminum circular disk of diameter 45 mm and 12-mm thickness. The disk was sprayed white and mounted on a rotary stage with its axis of rotation passing vertically through the plane of the disk.

For each measurement, in the reference state, a set of three images is recorded: an initial phase-referenced speckle pattern, Fig. IV-5a, Eq. (IV-2), an object image (Fig. IV-5b), and a reference-beam image (Fig. IV-5c). In a subsequent state, only one phase-referenced image is grabbed, Fig. IV-5d, Eq. (IV-4). When calibrating the setup, a fifth image is necessary. This image is a phase-referenced speckle pattern taken before applying any deformation.

The coarse details of Fig. IV-5a correspond to noise introduced by the reference beam. In subtraction, this noise is not critical, but some pixels may become saturated.
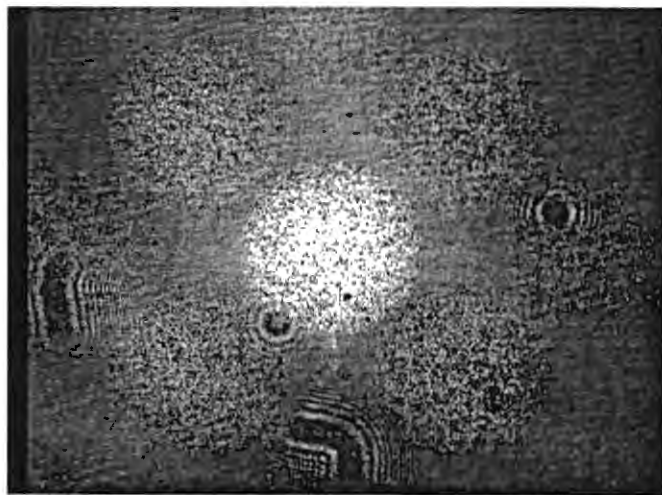
Fig. IV-5a)
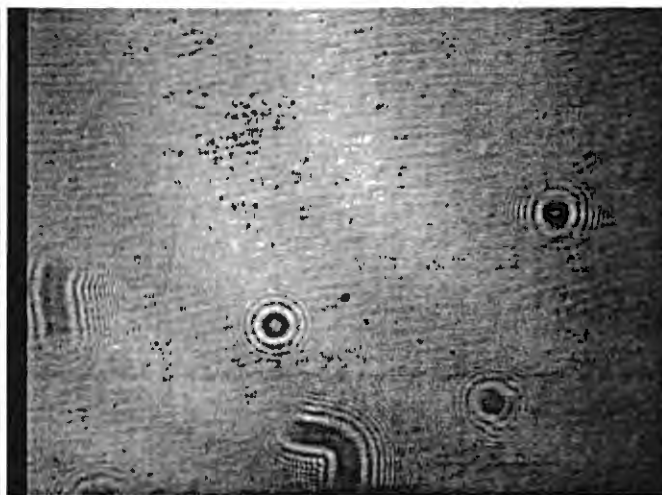
Fig. IV-5b)
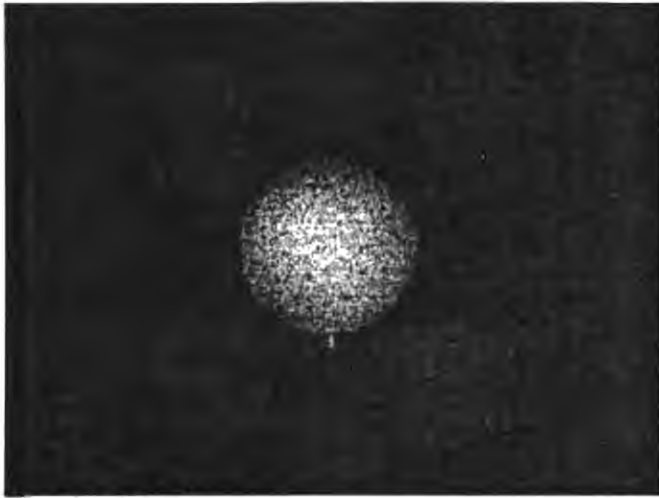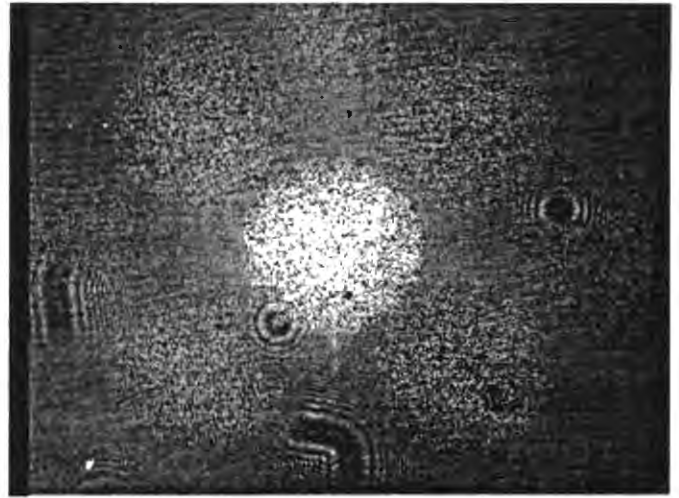
Fig. IV-5c)   Fig. IV-5d)

Fig. IV-5. For each measurement, 4 images are recorded. a) Initial phase-referenced speckle pattern. b) Spatial-filtered reference beam. c) Object beam. d) Phase-referenced speckle pattern with deformation.

Subtraction correlation fringes corresponding to out-of-plane rotation are shown in Fig. IV-6a, where the phase step between orders is clearly noticed. The transverse movements correspond to 22.5 μm in the x- direction and 11.25 μm in the y- direction. They give a phase stepping of $\pi/2$ rad.

Five iterations of an averaging filter within a 3x3 sample area are performed on the pattern of Fig. IV-6a. Then the optical phase is calculated modulo 2π rad, Fig. IV-6b. Subsequently, a spiral unwrapping algorithm is used to obtain the amount of out-of-plane tilt of the disk, which is displayed in gray levels, Fig. IV-6c, and in 3D representation, Fig. IV-6d.

By least-squares analysis the error is found as three times the standard deviation $3\sigma=\pm1.5494$ rad = ±0.2466 fringe =±0.1233 λ= ±0.0780 μm=±0.3575". Thus the computed displacement will deviate from its fit value by more than three standard deviations only 0.27% of the time. The total displacement is 1. 4895 μm. This value represents an out-of-plane rotation of 6.8274"±0.3575". This value is in agreement with the expected value, ~6.5".

The number of valid pixels related to the stepping and the phase were found to be 9102 and 16781 out of 20327 respectively; see **Appendix C** for thresholding criteria.
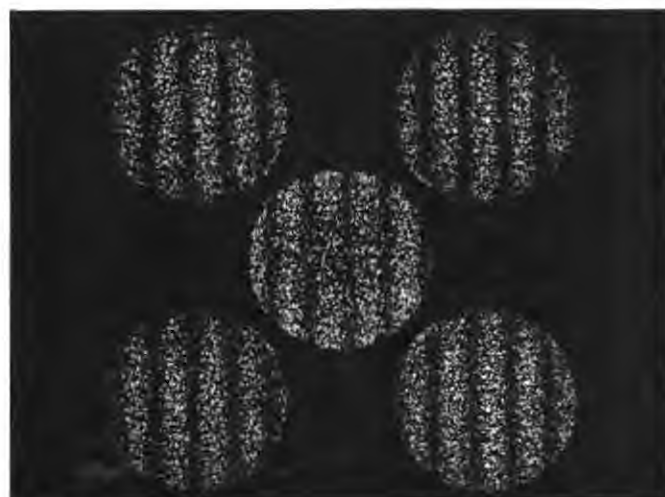
Fig. IV-6a)
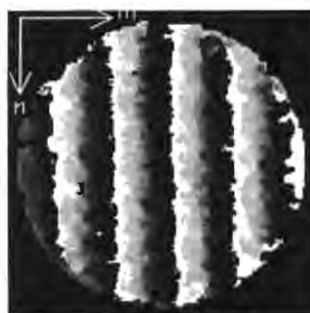
Fig. IV-6b)

Fig. IV-6c)
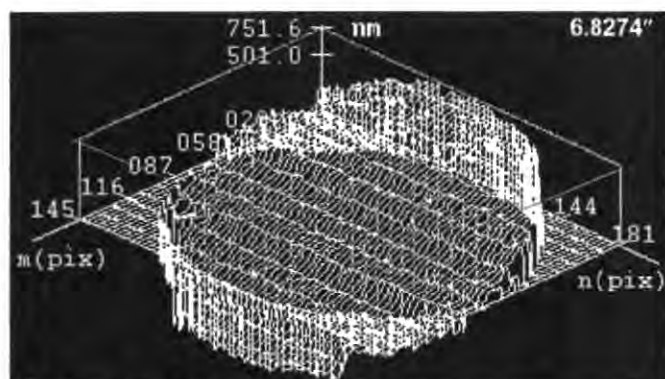
Fig. IV-6d)
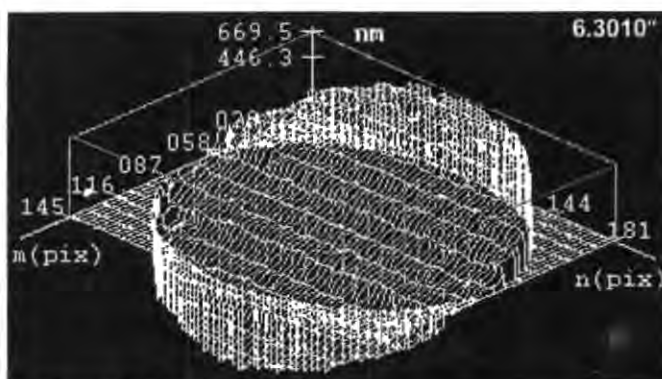
Fig. IV-6e)

Fig. IV-6. a) Subtraction correlation fringes. b) Phase map from Fig. **IV-6a**, modulo 2π. c) Resulting rotation in gray levels. d) Perspective representation of the rotation. e) Displacement map with iterative unwrapping algorithm.

Only for comparison purposes, Fig. IV-6e shows the displacement map calculated by an iterative unwrapping method (30 iterations), where 2 iterations of a median 3x3 filter were first performed on the phase map of Fig. IV-6b. The deviation is $3\sigma= \pm 1.4154\ rad = \pm 0.2253\ fringe =\pm 0.1126\lambda= \pm 0.0713\ \mu m=\pm 0.3268''$. In general, the latter unwrapping is better than the spiral one, but it is much more time-consuming. Since the precision for both algorithms is similar (considering the results of only this chapter), only the spiral algorithm will be used further.

In this example, noise is more noticeable in those regions where the phase becomes unambiguous, that is where there is a difference of 2π rad between adjacent pixels.

Experimental data always contain phase errors caused by decorrelation and by those points whose modulation amplitude is insufficient to calculate the phase with the desired precision.

IV-4   Stepping CGH

IV-4.1   Theory .

As above, the intensity at pixel (m,n) in the k'th quadrant, for a reference speckle pattern, can be represented as:

$$I_{ref,k}(m,n)=I_{0,k}(m,n)+I_{R,k}(m,n)+2\sqrt{I_{0,k}(mn,)I_{R,k}(m,n)}\,\cos\big(\psi(m,n)+(k-1)2\alpha(m,n)\big), \qquad \text{(IV-5)}$$

where $2\alpha(m,n)$ is the phase step introduced between each of the four images by a stepping CGH and $k =\{1,2,3,4\}$. Notice that unlike the previous case, the phase step depends on the position and therefore transverse movements are not needed. On account that the actual CGH phase step at 633 nm is unknown and different from its phase step at the designed wavelength 532 nm (of $\pi/2$), the optical interference phase $\psi(m,n)$ is extracted using the Carré algorithm. Normalized values of Eq. (IV-5), $I'_{ref,1}, ...,I'_{ref,4}$, are computed. If the object deforms, the intensity can be represented by:

$$I_{def,k}(m,n)=I_{0,k}(m,n)+I_{R,k}(m,n)+2\sqrt{I_{0,k}(m,n)I_{R,k}(m,n)}\,\cos\big(\psi(m,n)+\phi(m,n)+(k-1)2\alpha(m,n)\big) \qquad \text{(IV-6)}$$

from which the interference phase $[\psi(m,n) + \phi(m,n)]$ can be calculated using the normalized values $I'_{def,1},...,I'_{def,4}$. The phase difference $\{[\psi(m,n)+\phi(m,n))]- \psi(m,n)\}$ obtained from phase measurements made before and after deformation yields the interference phase due to object deformation $\phi(m,n)$ -DOP method. This technique cannot be used in addition mode and is limited by the TV field period. However, as shown in **Chapter V**, this technique can be used for the analysis of very rapid transient events.

It is possible to calculate ESPI correlation fringes directly. If TV fields recorded before and after deformation are subtracted on a pixel by pixel basis, we have:

$$I_k(m,n)=\left| I_{def,k}(m,n)-I_{ref,k}(m,n)\right|$$

$$=4\sqrt{I_{0,k}(m,n)I_{R,k}(m,n)}\left| \sin\left(\psi(m,n)+\frac{\phi(m,n)}{2}+(k-1)\alpha(mn,)\right)\sin\left(\frac{\phi(m,n)}{2}\right)\right| \qquad \text{(IV-7)}$$

As can be seen, the phase step for subtraction correlation fringes is cancelled at each pixel. If we wish to view phase-stepped correlation fringes, we must subtract the normalized intensities between orders. Using order k=1 as reference gives -see Fig. IV-7:

$$I_k(m,n) = \left| \sqrt{K_{O,k} K_{R,k}(m,n)}\, I'_{def,k}(m,n) - I'_{ref,1}(m,n) \right|$$

$$= 4\sqrt{I_{0,1}(m,n) I_{R,1}(m,n)} \left| \sin\left(\psi(m,n) + \frac{\phi(m,n)}{2} + (k-1)\alpha \right) \sin\left(\frac{\phi(m,n)}{2} + (k-1)\alpha(m,n) \right) \right| \qquad (IV-8)$$
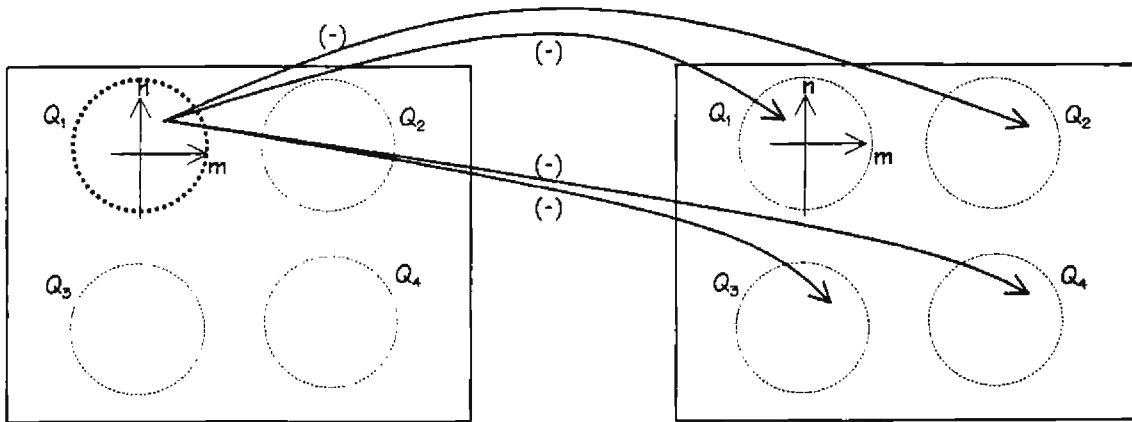
Fig. IV-7. POD subtraction correlation fringes. The left image corresponds to an undeformed state and the right one to a deformation state (stepping CGH.) The reference image is Q_1. A correspondence function is assumed between the five quadrants. This subtracting method is also used for checking correct alignment of the stepping CGH.

IV-4.2   Experimental results
IV-4.2.1   Static object

As in the previous section, this technique is used in the measurement of rotation. Fig. IV-8f shows direct subtraction fringes. As expressed by Eq. (IV-7), the fringe pattern does not show any relative phase step. Unlike this, when taking quadrant k=1 as the reference speckle pattern phase-stepped fringes are obtained according to Eq. (IV-8). However, this method is much more susceptible to departure from in-line conjugacy than the DOP method. Furthermore, the DOP method has been shown to give better results than those calculated with POD [4]. Therefore, the DOP method will be employed in conjunction with this technique.

The phase-referenced speckle pattern shown in Fig. IV-5a is used to calculate a phase map (shown in Fig. IV-8a), using the normalized values of Eq. (IV-5). A second phase-referenced speckle pattern (Fig. IV-5d) is then used to calculate a second phase map (see Fig. IV-8b) after

object deformation in accordance with a normalized version of Eq. (IV-6). The difference of these two phase maps yields the optical phase due to object deformation, Fig. IV-8c. Only 62.8% of the data were found to be valid. The optical phase is low-pass filtered by applying a 3x3 median filter twice, Fig. IV-8d. Next, the result of unwrapping the latter fringe pattern gives the quantification of the aluminum disk displacement, Fig. IV-8e. The estimated error is $3\sigma = \pm2.0403$ rad $= \pm0.3247$ fringe $=\pm0.1623$ $\lambda = \pm0.1028$ μm. The displacement map represents a rotation of 8.2451"$\pm$0.4712".
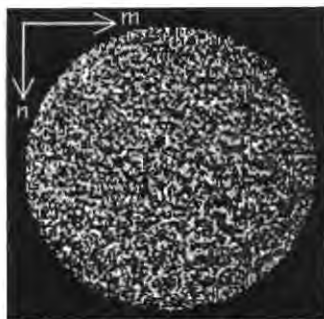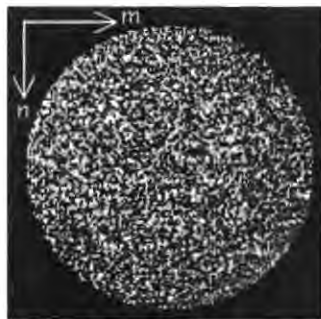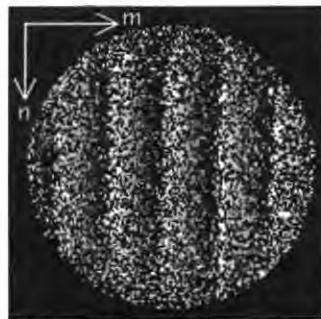
Fig. IV-8a)   Fig. IV-8b)   Fig. IV-8c)   Fig. IV-8d)
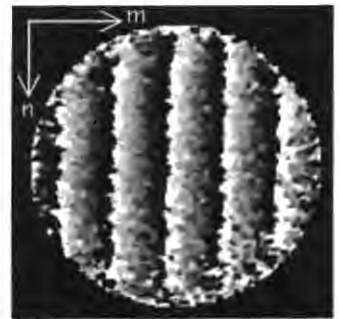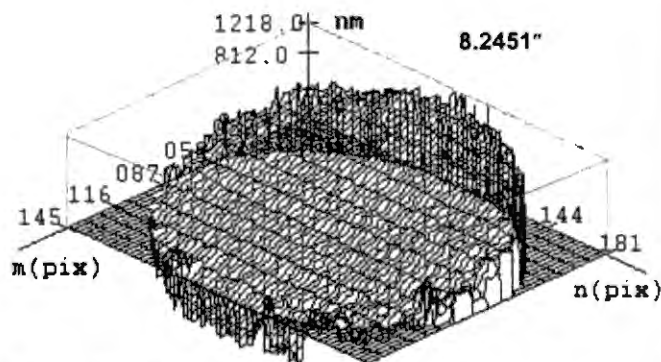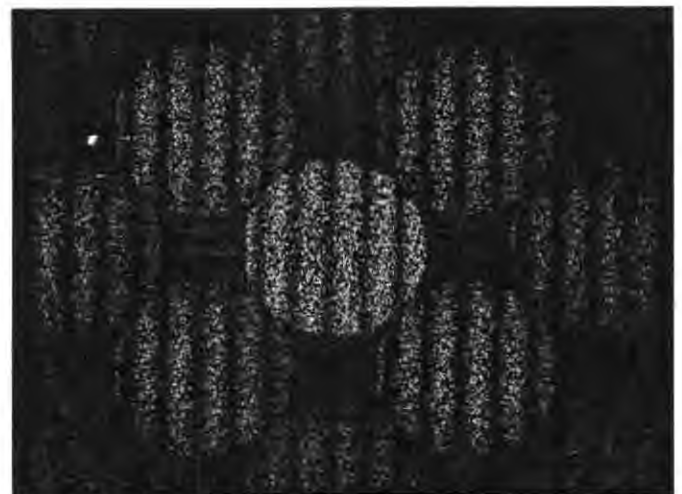
Fig. IV-8e)   Fig. IV-8f)

Fig. IV-8. Processing of DOP fringes. a) Initial phase map modulo 2π rad, obtained from speckle pattern of Fig. IV-5a. b) Deformation phase map. c) Subtraction of phase maps of a) and b). d) Correlation fringe map of c) after being median-filtered. e) Perspective representation of the out-of-plane tilt, in nm, after unwrapping the fringe pattern on d). f) Fringe map obtained by direct subtraction, application of Eq. (IV-7).

IV-4.2.2   Dynamic object

By activating a soldering iron located in front of the aluminum disk, we can change the index of refraction in that particular volume, Fig. IV-9. The quantity to be measured corresponds to a change in optical path difference (OPD) arising from variations in the index of refraction in that particular volume. This quantity includes an integrated value through the object volume along the light beam, see Fig. IV-9b. The refractive index in the first exposure is assumed to be uniform and denoted by n_o. During a second exposition, the soldering iron is switched on and the refractive index then changes to $n(x,y,z)$. The phase difference from both recordings is given as

$$\phi(x,y) = 2k \int \left(n(x,y,z) - n_o \right) dz, \qquad (IV-9)$$

where k is the propagation vector. We have assumed both plane object wave illumination along the z-axis and observation along the z-axis.
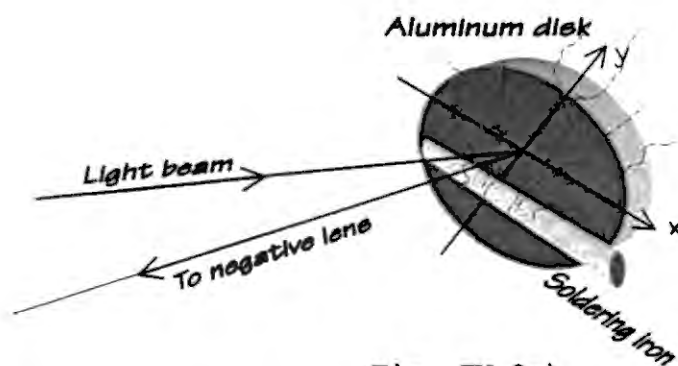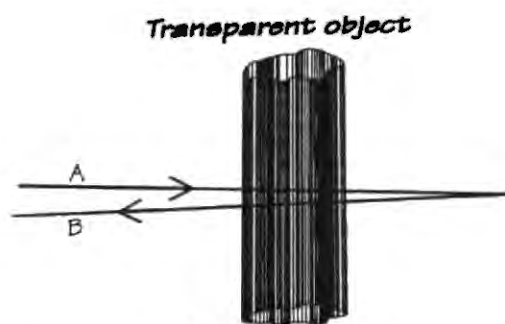
Fig. IV-9a)   Fig. IV-9b)

Fig. IV-9. Setup for analysis of phase objects. a) When the soldering iron is switched on produces a change of the refractive index of the medium in front of the disk. b) Transparent object.

A series of phase-referenced speckle patterns were recorded as the soldering iron heated up. A phase map was calculated from each of the images and compared to a reference phase map. The result is a time history of the temporally varying thermal plume which could not be measured with standard temporal phase-stepping techniques. The captures were taken at 5, 10 and 15 s. The soldering part was placed in the lower part of the circle of interest. Fig. IV-10d contains stepped-subtraction fringes for the event at 10 s (Eq. (IV-8), see Fig. IV-7). Figs. IV-10a, IV-10b and IV-10c show the corresponding 3x3 median-filtered optical phase maps. After unwrapping, maps representing the OPD associated with the convection flow are obtained

(Figs. IV-10e, IV-10f and IV-10g). The hottest zone is identified in the surroundings of the soldering part. According to the ideal gas equation, the temperature varies inversely with density. On the other hand, the density of a fluid is proportional to its refractive index (Gladstone-Dale equation [5]). Thus, the temperature is inversely proportional to the OPD, and consequently the light travels faster inside the plume.
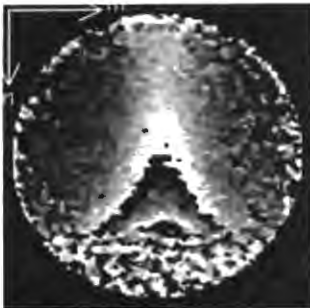
Fig. IV-10a)

Fig. IV-10b)
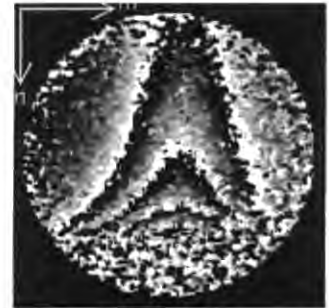
Fig. IV-10c)
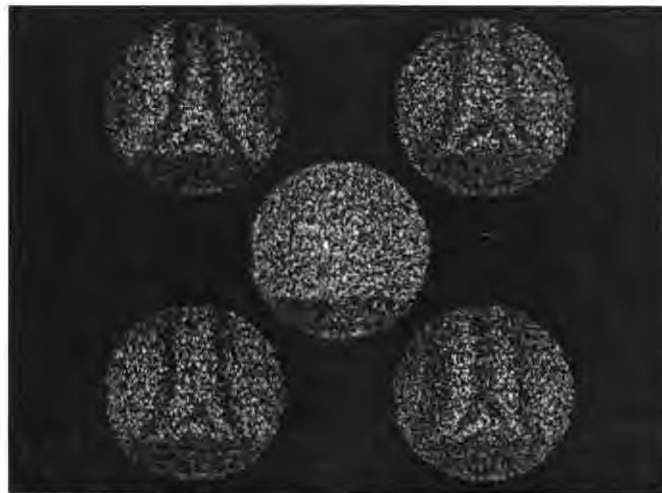
Fig. IV-10d)
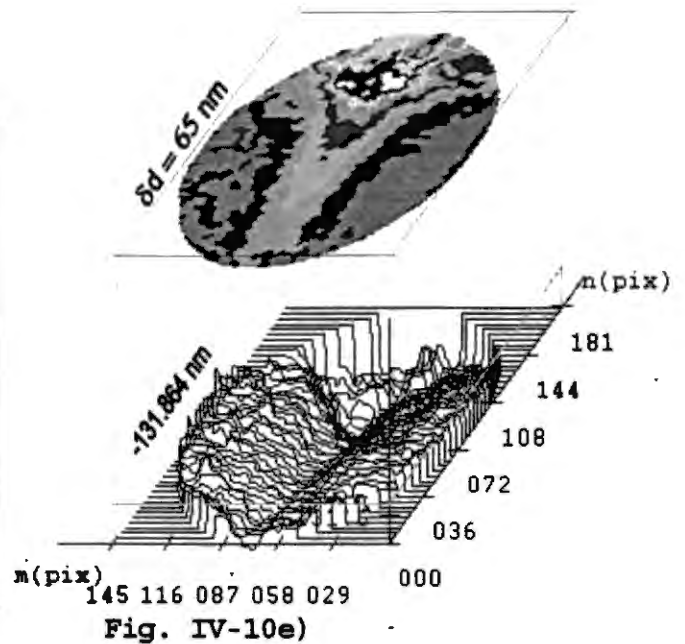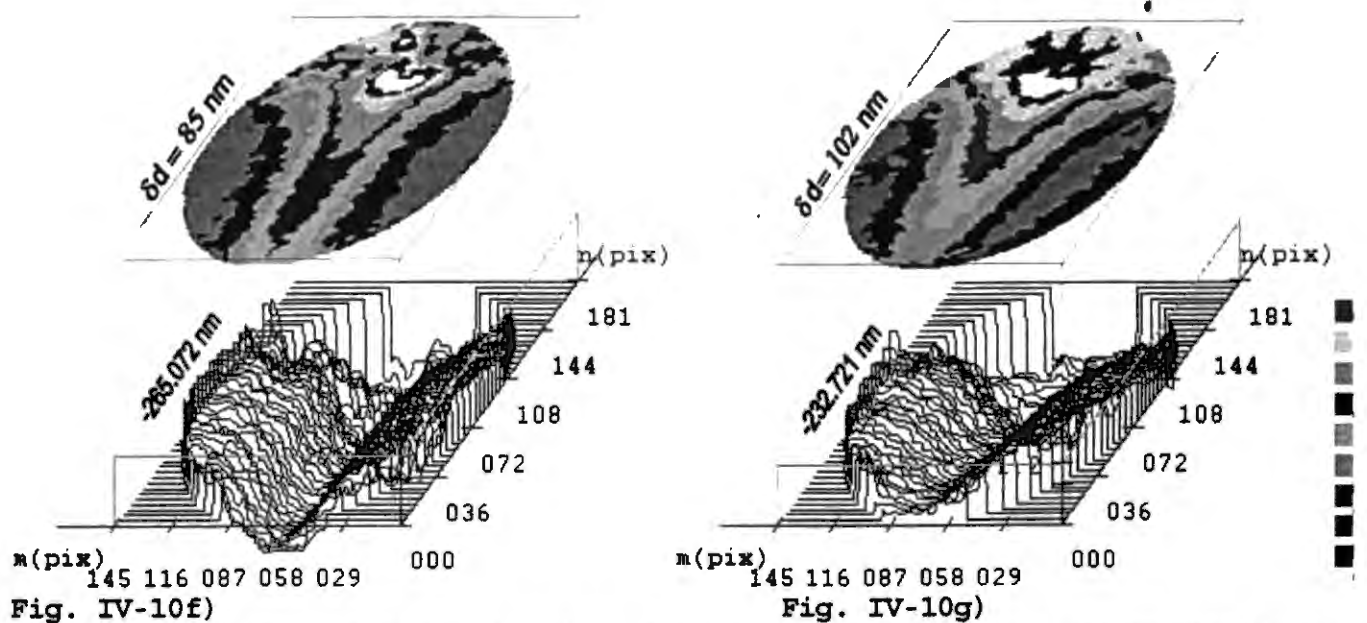
Fig. IV-10e)

Fig. IV-10f)   **Fig. IV-10g)**

Fig. IV-10. Analysis of a transient event. The phase object corresponds to a change in the refractive index of the air in front of an aluminum disk. a)-c) OPD optical phase, at **5, 10** and **15 s**, respectively. d) POD subtraction fringes, 10 seg. e)-g) OPD maps at **5, 10** and **15** s in **nm**.

The error in the measurements is the same as that calculated in the static case. The numbers included in the perspective figures indicate the contour interval (δd) and the value of the OPD at the center of the disk. The sequence of phase maps and OPD maps clearly show the development of the thermal plume generated by convection effects as the air moves upwards.

IV-5   Combined use of nonstepping and stepping CGHs

IV-5.1   Theory

This method assumes that the reference speckle pattern is recorded using a nonstepping CGH and that the second image is recorded using a stepping CGH. Concerning the mathematical treatment, the order of grabbing is not important. In the second capture, unlike **Section IV-3**, phase-stepping does not arise from transverse movements but from the stepping CGH. The reference image has the next form

$$I'_{ref,k}(m,n) = \sqrt{\frac{K_{O,k}K_{R,k}(m,n)}{K_1}}\left(I_{ref,k}(m,n) - I_{O,k}(m,n) - I_{R,k}(m,n)\right) \tag{IV-10}$$

where $K_1 = <I_{0,1}(m,n)>/<I_{S0,1}(m,n)>$ accounts for the ratio of the nonstepping CGH intensity and the stepping CGH intensity, for Q_1, and $K_{0,k} = <I_{0,1}(m,n)>/<I_{0,k}(m,n)>$ refers to the nonstepping hologram normalization factors. This new factor accounts for the slight difference in the diffraction fields for each hologram. The reference beam is the same for both CGHs and needs no further normalization.

On the other hand, for the second recording using the stepping CGH, the normalized intensity at pixel (m,n) is given by

$$I'_{def,k}(m,n) = \sqrt{K_{S0,k} K_{R,k}(m,n)} \left(I_{def,k}(m,n) - I_{0,k}(m,n) - I_{R,k}(m,n) \right), \qquad \text{(IV-11)}$$

where $K_{S0,k} = <I_{S0,1}(m,n)>/<I_{S0,k}(m,n)>$, with subscript S standing for the stepping CGH. The phase stepping due to the stepping CGH is included implicitly in the term $I_{def,k}$. The phase reduction is performed as in **Section IV-3** by the POD method. No reference quadrant needs to be selected because subtraction is made on a quadrant by quadrant basis (see also Fig. IV-4.)

To verify that no spurious carrier fringes are introduced while changing holograms (because of tilt, different transverse position and/or rotation of the CGHs) an auxiliary object is used. By this second object, correct phase stepping is checked for each CGH. When the position of the stepping hologram is correct, the secondary object is removed and the aluminum disk is incorporated. As in **Section IV-3**, when subtracting the reference pattern from a second acquisition with $\phi(m,n)$ set to zero (after replacing holograms, but before deforming the object), the resulting correlation map must present no correlation fringes at all.

If this technique is to be applied in the analysis of transient phenomena, it will be limited only by the response of a Pockels cell, should a polarization technique is to be used. Furthermore, this technique, unlike **Section IV-4** method, can also be implemented in double-pulsed addition.

IV-5.2   Experimental results

In the first recording a stepping CGH is used. Firstly, correct phase-stepping is checked. To carry this out, we used an auxiliary object (a beam in cantilever). The resulting phase and displacement maps are shown in Figs. IV-11a and IV-11b. It can be noticed that the deformation

only includes the auxiliary object. To obtain this result, the technique **in Section IV-4** is used. Once the hologram has been positioned correctly, the auxiliary object is removed and the aluminum disk is incorporated. At this point, the state of the disk is taken as the reference undeformed image, Eq. (IV-10).
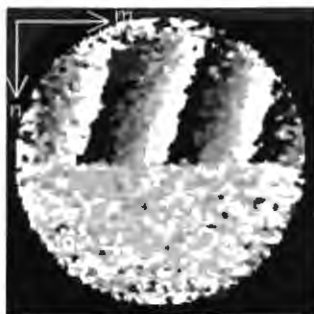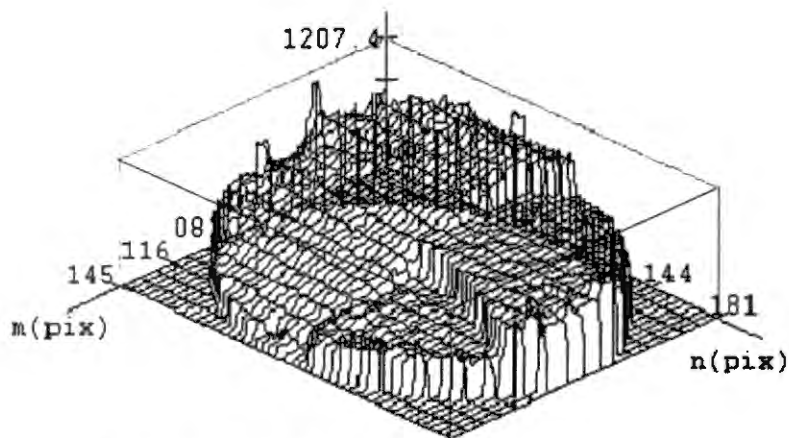
Fig. IV-11a)   **Fig. IV-11b)**

Fig. IV-11. Inspection of the first state of the measurement, done by technique in **Section IV-4** with DOP. Auxiliary object. a) DOP phase map. b) Displacement map. The auxiliary object corresponds only to the left part of the images.

Before deforming the object, the stepping CGH is replaced by the nonstepping CGH, and its position is checked by obtaining correlation fringes for the auxiliary object, and verifying that the phase-stepping is null, Fig. IV-12a. Then, after removing the auxiliary object, another image of the disk is captured (before being subjected to deformation). Next, the aluminum disk is rotated about a vertical axis and the image with deformation is captured, Eq. (IV-11). For this image, null stepping is again checked by obtaining subtraction correlation fringes, Fig. IV-12b, where the reference image is the one captured before the rotation of the disk. Finally, according to Eq. (IV-10) and (IV-11), captures before and after rotation are subtracted, Fig. IV-13a, and the phase extracted, Fig. IV-13c. Fig. IV-13d shows the corresponding displacement map.

This technique presented the highest error $(3\sigma= \pm2.26\ rad = \pm0.3549\ fringe = \pm0.1799\ \lambda= \pm0.1139\ \mu m)$, and therefore the displacement map shows several discontinuities. The error stems mainly from the replacing of holograms. In spite of this, the measured rotation, $8.1635''\pm0.5220''$ agrees well with the applied rotation ~8″.

This was the most difficult technique to implement. Two considerations have to be kept in mind. The CGHs must present neither tilt nor rotation, and the shifting of the holograms must not introduce spurious carrier fringes due to a different position of the spatial period of one CGH with respect to the other. This means that if the alignment of the holograms is correct, then by subtracting the undeformed image (reference image) from the image before rotation (after the shifting of holograms), the result should not show any spurious carrier fringes. This fact is shown in Fig. IV-13b (according to diagram in Fig. IV-4).
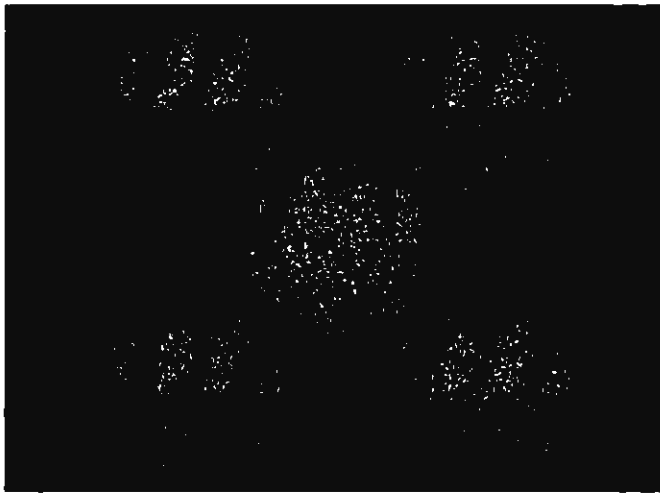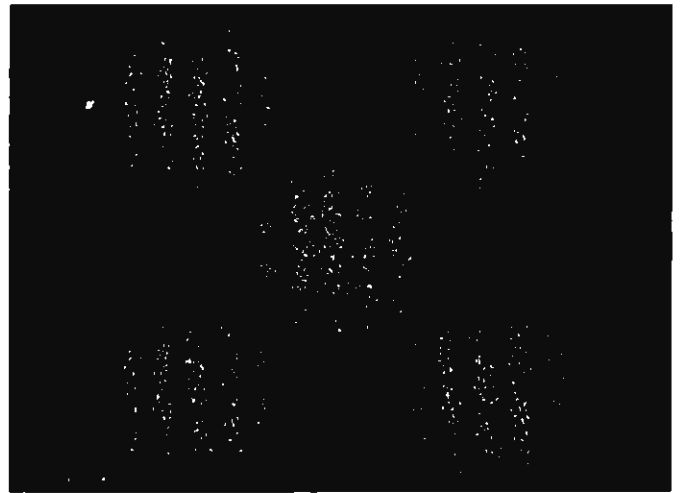
Fig. IV-12a)   Fig. IV-12b)

Fig. IV-12. Inspection of correct nonstepping-hologram position during the deformation state, done by obtaining subtraction correlation fringes by diagram of **Fig. IV-7.** a) Auxiliary object. b) Aluminum disk, out-of-plane rotation. Phase can not be obtained because the phase-stepping is null.
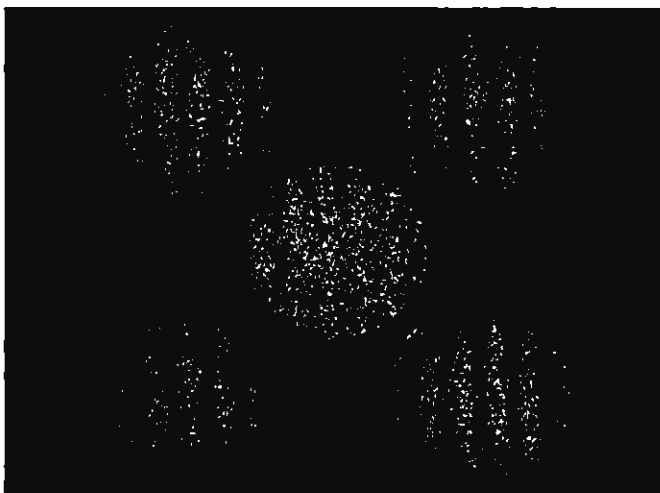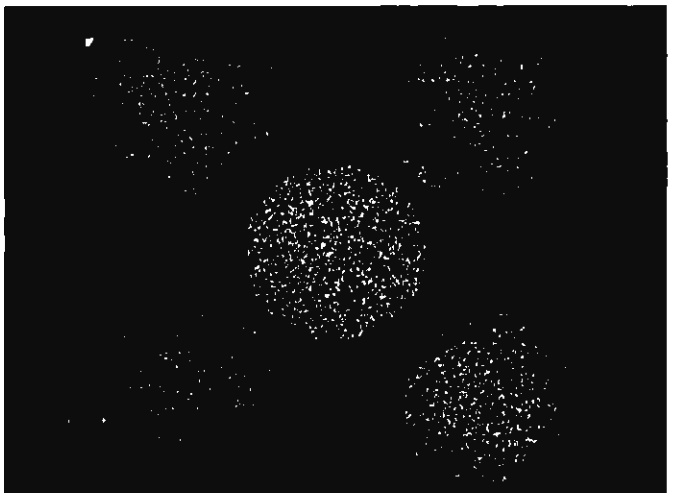
Fig. IV-13a)   Fig. IV-13b)
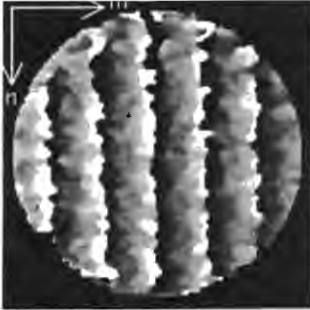
Fig. IV-13c)
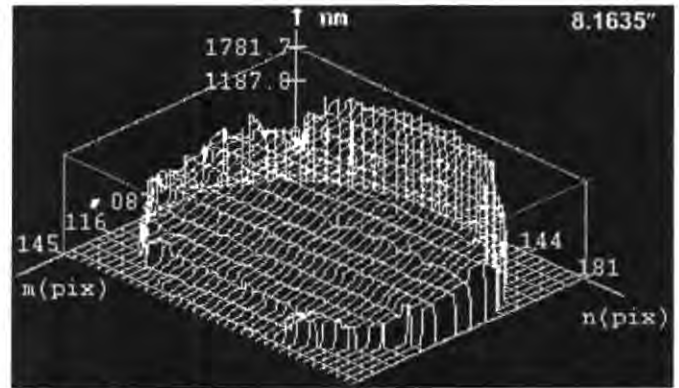
Fig. IV-13d)

Fig. IV-13. Results by combining holograms, POD method. a) Subtraction fringes. b) Error arising from a combination of air turbulence, distinct diffraction of CGHs, and replacing of holograms. Subtraction on a quadrant basis. Stretching of the gray-level is assumed. c) Phase map modulo 2π. It was calculated after having applied 6 iterations of a 3x3 averaging filter to fringes of Fig. **IV-13a**. d) Displacement map, obtained from Fig. **IV-13c**.

On the other hand, if Q_1 of the nonstepping CGH is correlated with the stepping CGH we get the results shown in Fig. IV-14 —see diagram in Fig. IV-7. Results employing this technique ($3\sigma = \pm 1.932$ rad = ± 0.3075 fringe = ± 0.1535 $\lambda = \pm 0.0973$ μm) are better than those obtained in the preceding paragraphs and similar to those obtained in **Sections IV-3** and **IV-4** (with an error of $\pm 0.15\lambda$). The errors obtained in this section are greater than those from the two previous sections. This is because apart from including errors due to turbulence of air and difference in the intensity diffraction orders for each hologram, they include errors due to the difference in the intensity diffraction orders for different holograms as well as those due to the replacement of the CGHs.
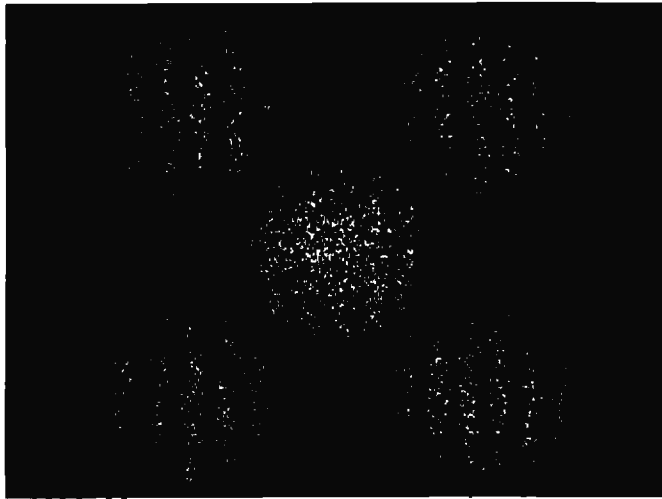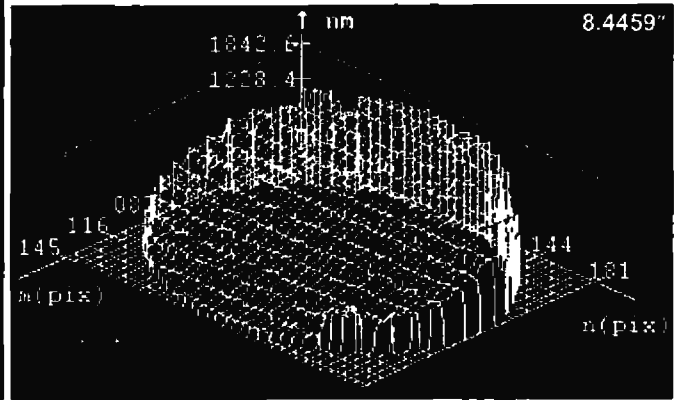
Fig. IV-14a)   Fig. IV-14b)

Fig. IV-14. The reference speckle pattern corresponds to Q_1 of the nonstepping CGH. a) Current example with second state deformed. b) Displacement map. The out-of-plane rotation is $8.4459''\pm0.4460''$.

IV-6   Summary

Concerning the techniques presented in this chapter, the main sources of error in the measurements include movements of holograms, departure of conjugacy, and diffraction differences. The quality of the measurements near the edge of the disk was further reduced due to the Gaussian feature of the beam. The low-quality of the results was reflected in the total number of valid pixels, which was around 65% for DOP.

One of the main source of errors stems from the movement of the holograms before deformation. Thus, results given in **Section IV-3**, when a stepping CGH was employed, the computations showed a higher signal-to-noise ratio since only one hologram is used and its position remains unchanged throughout the experiment. This means that phase errors stemming from tilt and rotation of the CGH are eliminated. However, pixel-matching between the 4 quadrants is time-consuming since it involves a preprocessing of the images which consists of obtaining correlation patterns for pixels in a certain boundary (3x3 pix); the pattern with the highest contrast is chosen and the corresponding coordinate for each point obtained.

The three techniques can be used for the analysis of transient events where the separation between consecutive events can be reduced with no limit as it is shown in **Chapter V**. However, the second method would be the simplest since the hologram does not need to be

moved between consecutive captures. A limitation of this method is that it cannot be used in the addition mode. In contrast, the other two methods would only be limited by the response time of the device used to move the holograms between consecutive captures (of the order of µs). These techniques offer several cost-advantages over multi-channel camera systems. The observed precision, in general, is ~±0.15 λ.

IV-7   References

[01] M. Deininger, L. L. Wang, K. Gerstner and T. Tschudi, "Optical phase step method for absolute ranging interferometry using computer-generated holograms," App. Opt. **34**(25) 5620-5623 (1995).

[02] M.V.R.K Murty, "Use of convergent and divergent illumination with plane gratings", J.O.S.A. **52**, 768-773 (1962).

[03] R. Jones and C. Wykes, *Holographic and Speckle Interferometry*, CUP, London (1983).

[04] A. J. Moore, J. R. Tyrer, and F. Mendoza-Santoyo, "Phase extraction from electronic speckle pattern interferometry addiiton fringes", App. Opt. **33**(31) 7312-7320 (1994).

[05] C. M. Vest, *Holographic Interferometry*, John Wiley & Sons, U.S.A. (1979).

Chapter V   Application of ESPI to transient events

The main goal of this investigation was the measurement of transient events. In this chapter, preliminary results are reported. They are related to dynamic processes of the order of a few microseconds: an aluminum plate was given an impact and the originated mechanical wave was quantified at several time positions. We have only used the method described in **Section IV-4** of **Chapter IV**, i.e. use of a stepping CGH with no transverse movements. We chose an iterative unwrapping algorithm (refer to **Chapter II**) to quantify the deformations. The attained overall precision was ~0.15λ.

Firstly, the synchronization scheme is explained. We have used practically the same setup than in **Chapter IV**. In this case, we used a doubled-frequency Nd:YAG laser. As it was explained in **Chapter II**, as the wavelength decreases, the divergence is reduced proportionally; therefore, the CGH-to-CCD distance increases. This means that the alignment of the CGH is more demanding. In addition to this, only half the full vertical resolution was used (263 lines per image). Consequently, the quality of the phase maps is lower than those obtained in the previous chapter. However, the use of the iterative unwrapping algorithm partially relieved this drawback.

V-1   Setup and synchronization scheme

A similar setup than that used in the previous chapter is employed, as shown in Fig. V-1. The object-beam expander is a negative lens with short focal distance. Due to the pulsed mode of the Nd:YAG, air may become ionized if a microscope objective is used, with consequent spatial degradation of the beam. Some important distance values in Fig. V-1 are given in Table 5A.

Table 5A

	OBJECT-NL$_1$	NL$_1$-NL$_2$	NL$_2$-ZOOM	ZOOM-CCD	BC-CCD	SF-BC	CGH-ZOOM
Distance [mm]	550	118	265	341	40	300	2

The angle between the optical axis and the object beam was measured as 8°. An F number of 8 was used with an f=161 mm. The conjugacy tolerances were ±5 mm and ±1 mm along the axis and transversally, respectively. The distances zoom-to-BC and SF-to-BC are essentially identical. This ensures longitudinal conjugacy. One sample image detected by a slightly different system is shown in Fig. V-2. The object length is 90 mm. A halo surrounding the central zone is noticed. This is because the NL_1-to-NL_2 distance was so long that the image of the first lens is partially collected by the second negative lens. Fig. V-3 shows one object image with the parameters of Fig. V-1, which corresponds to a calibration image (noticed that the speckle structure is similar to the four quadrant images). This image was stretched for visualization purposes. This figure also shows that considerable energy is lost through the order zero.
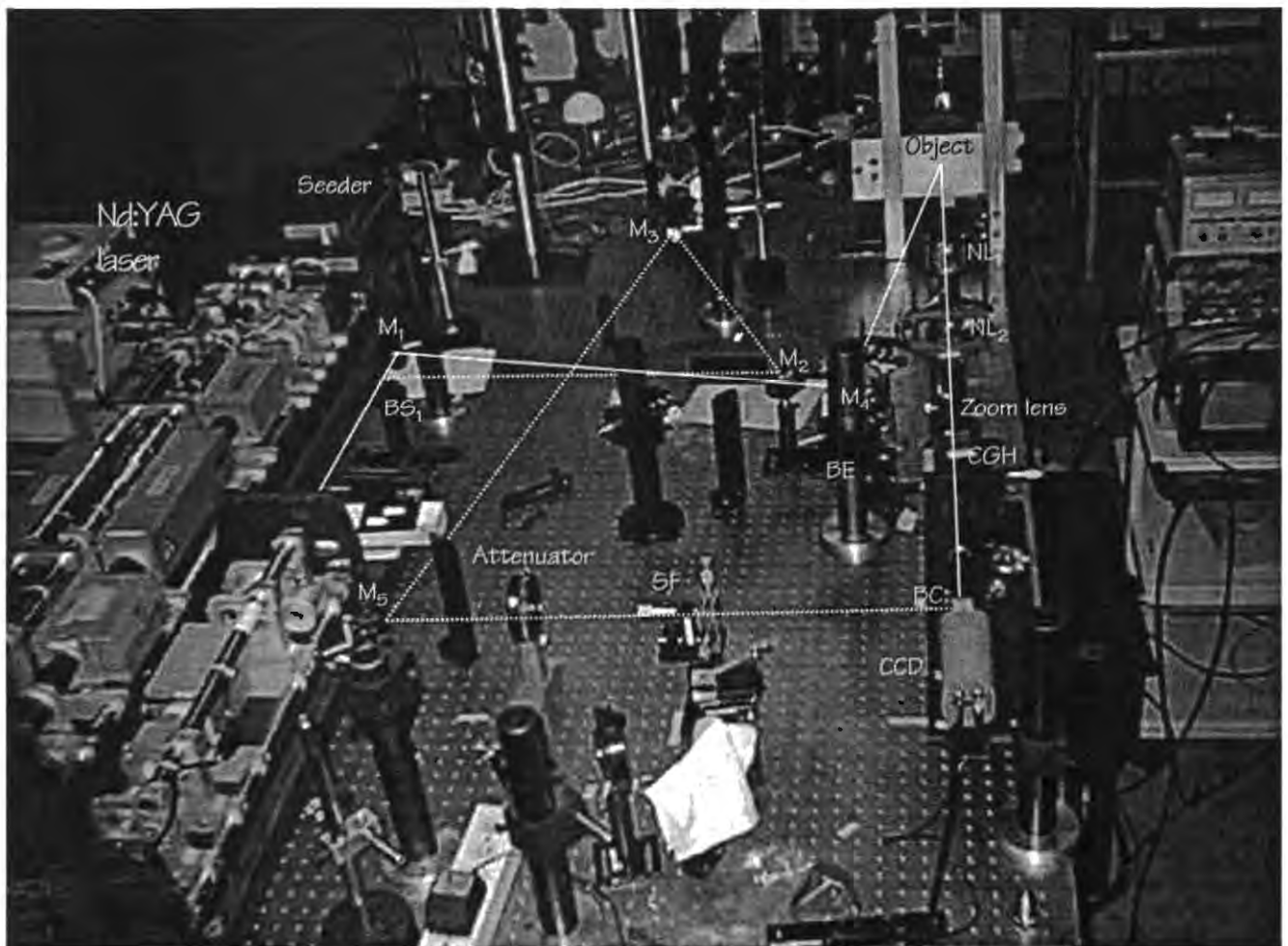
Fig. V-1. ESPI arrangement with out-of-plane sensitivity. BS: Beam splitter; BE: Beam expander; SF: Spatial filter, NL: Negative lenses; BC: Beam coupler.
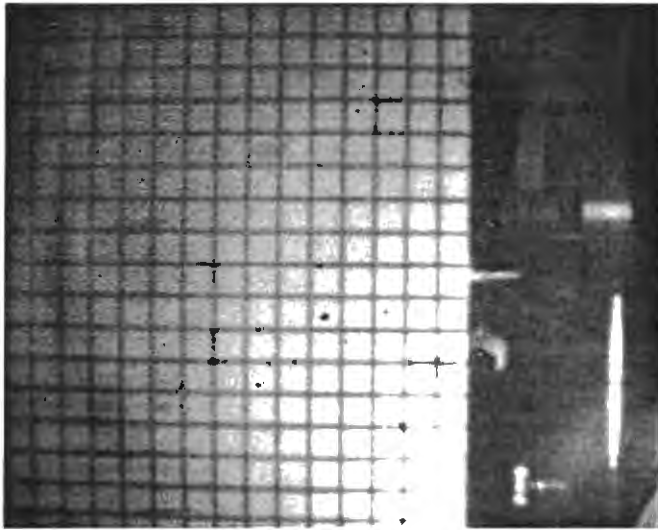
Fig. V-2. Sample image obtained by setup of Fig. **V-1.** For subsequent images, the **NL₁-to-NL₂** distance was shortened to avoid imaging the first negative lens (NL₁).
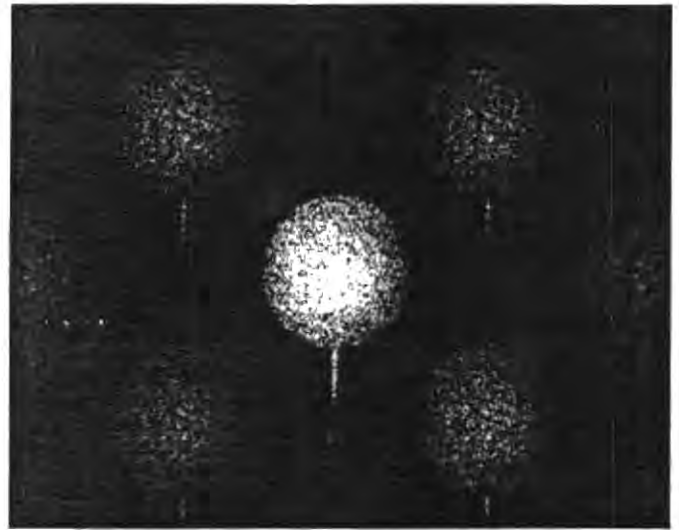
Fig. V-3. Image obtained by the optical system of Fig. **V-1.** The speckle structure is similar to the four quadrant images.

When there is not longitudinal conjugacy, carrier fringes are introduced as we subtract reference Q_1 from the quadrants of a subsequent capture with no deformation (see diagram in Fig. IV-7, **Ch. IV**), shown in Fig. V-4a. Thus, when the second capture contains deformation, the result is misled, yet the order zero, Fig. V-4b. If the position of the reference point source is placed at infinity by replacing the SF by a collimator, no deformation correlation fringes are obtained by this method. However, direct subtraction is not influenced by this effect. Hence, correct conjugacy was verified simultaneously when calibrating the optical system. The error analysis is given in a subsequent section.
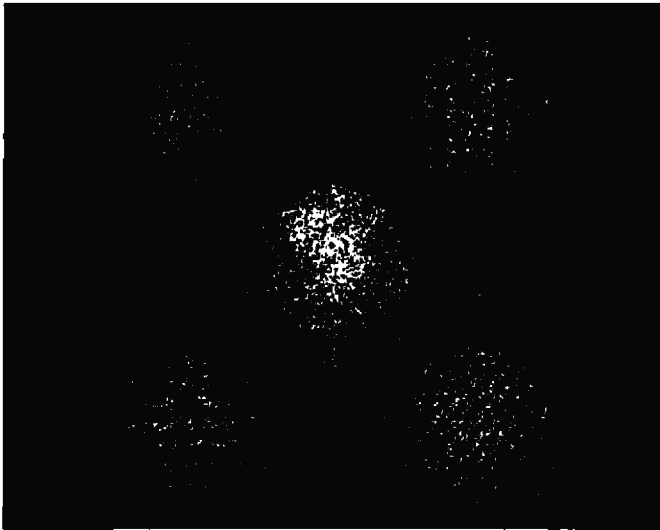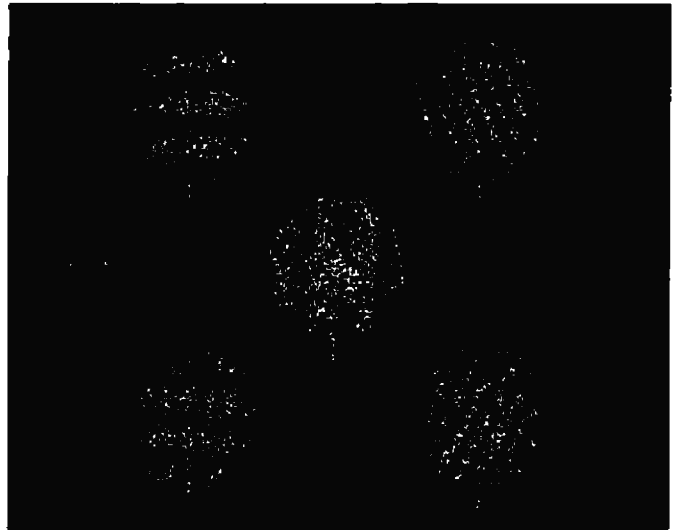
Fig. V-4a)   **Fig. V-4b)**

Fig. V-4. Incorrect conjugacy. a) No deformation is introduced, but spurious fringes appeared as a result of departure of conjugacy. b) Second state with deformation. All the quadrant correlation images have different carrier frequencies, the zeroeth order inclusive.

In the following series of measurements two different objects are used (aluminum plates in cantilever sprayed white), Fig. V-5. They have a different notch. The notches are expected to modify the propagation of the mechanical wave. The region of interest was limited by an aperture placed after expanding the object beam, and corresponded to a circle of diameter 19 mm. Use of two negative lenses enables larger fields of view. The zoom-to-negative-lens distance shortens when only one negative lens is used, only if the object position remains unchanged. In this case, results are better because of the higher resolution.

The object is hit by a 2-mm-diameter metal rod attached to a loudspeaker. The rod is placed at 2 mm behind the object and strikes the plate at 2 mm at the right of the rectangular notch (1mmx6mmx5/32"), Fig. V-5a, and at 7 mm below the circular notch, Fig. V-5b. We varied the impact duration from 100 to 150 μs. The duration of the event is within the range of a few seconds.
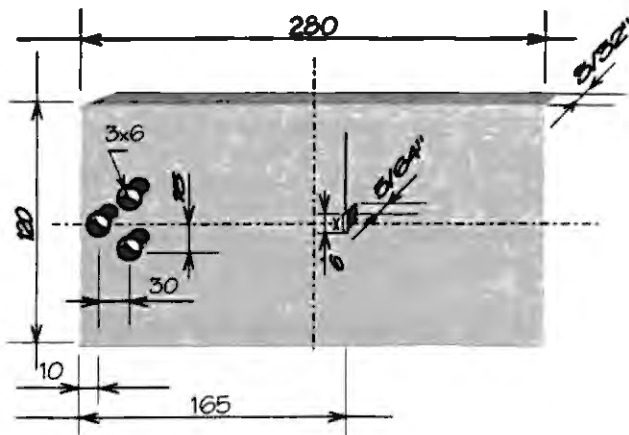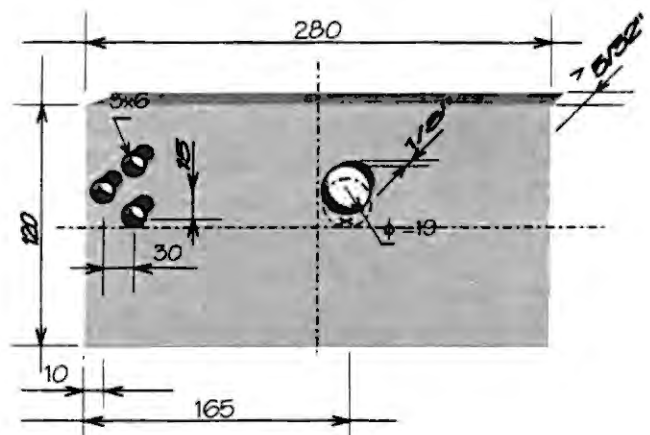
Fig. V-5a)   **Fig. V-5b)**

Fig. V-5. Aluminum plates with notch. Views from behind. a) The impact is at 2mm at the right of the rectangular notch. b) The impact is given at 7 mm below the circular notch and is located at 2.4 mm from the bottom edge of the 19-mm-diameter observation region. The impact is indicated by a cross. The dashed circle corresponds to the region of interest. The plate is clamped at its left side through 3 screws.

Next, the synchronization scheme is discussed [1]. A video source contains both video and timing information. The timing information corresponds to the vertical (60 Hz, 5V TTL) and horizontal signals. The former, also known as the transfer-gate period, is the reference signal to the whole system, as shown in Fig. V-6, and is input to the host computer via a digitizing board (VFG) and to the synchronization circuit via a BNC connector. By means of the computer, an operator can then initiate the acquisition of images at valid time positions, i.e. avoiding acquisitions at the vertical blanking period. On the other hand, the synchronization circuit can drive the laser at valid time positions as well, at a frequency of one Q-switched pulse per field.

Software acquisition routines perform the digitization of images within two consecutive fields (working with consecutive fields reduces the influence of external disturbances). Only the odd lines of each field are used (263 lines per field). Through this software, a starting signal is sent to the synchronization circuit via the parallel port of the host computer (at 5V).
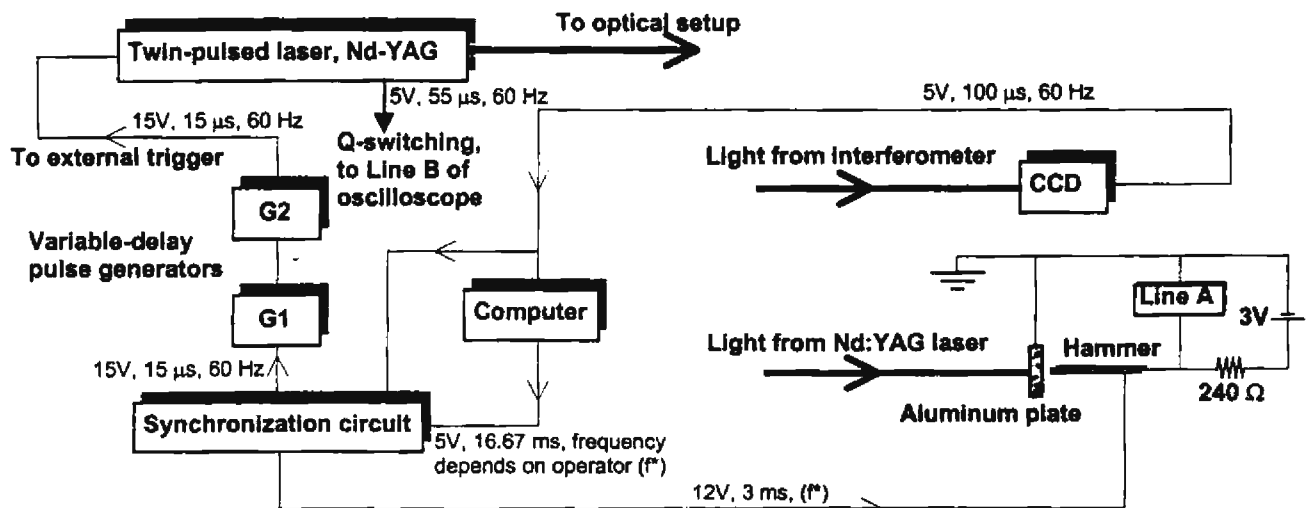
Fig. V-6. Synchronization circuit. **G1** and **G2** control the delay of triggering, coarse delay (~µm) and fine tuning (tens of ns), respectively. Both the Q-switching signal and the signal obtained from the battery-and-resistor circuit are presented simultaneously on an oscilloscope display. The synchronization circuit and the variable-delay pulse generators can vary the time between the onset of the impact (close circuit) and the illumination of the object.

The synchronization circuit reinforces the parallel port signal and, depending on the vertical signal (logic AND), activates the loudspeaker. Furthermore, it generates a 15-µs pulse (triggering pulse) that is input to two variable-delay pulse generators at a rate of 60 Hz. The pulse generators are used only for delaying purposes. The first one, $G1$, allows us to delay the triggering pulse by a few µs, whereas $G2$ by tens of ns. This pulse is input to the external trigger of the Nd:YAG laser, which consequently initiates the light pulse formation. Since the time it takes the laser to produce a Q-switched pulse is different from that it takes the loudspeaker to hit the aluminum plate, we can not know the actual delay between the onset of the impact and the illumination of the object. Thus, a monitoring circuit is implemented. When the hammer strikes the aluminum plate, it closes the battery-and-resistor circuit and the signal goes to 0 V. Pre-energizing the battery-and-resistor electric circuit warranties that no spurious signals can be mixed with the signal that is being monitored. Fig. V-7 shows the oscilloscope display (on Line A) as the plate undergoes the transient load. The time at which the object is illuminated is detected by means of the Q-switching signal of the laser. This signal is taken from the laser and directly passed to Line B of the oscilloscope. Hence, both signals are detected simultaneously and the delay between the onset of the impact and the illumination of

the object t_d can be measured, as is shown in Fig. V-7. This delay can be varied by the pulse generators. A typical value for the impact duration, t_i, was 100 µs. This value was controlled by varying either the width of the voltage pulse applied to the loudspeaker or the distance between the plate and the metal rod tip. The delay time was varied from 0 to 2700 µs. The HWHM of the laser pulses and the Q-switching signal are 20 ns and 55 µs respectively.
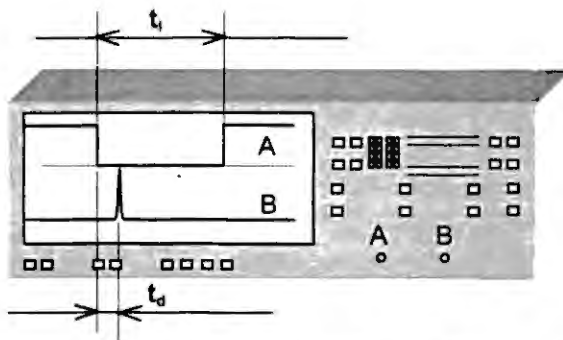
Fig. V-7. Monitoring of the times at which the laser illuminates the object and that at which the hammer strikes the aluminum plate. The Q-switched pulsewidth is 55 µs (displayed on channel B). t_i is the impact duration and t_d is the delay between the two signals. The signal on channel A is driven to 0 V while the impact takes place.

The first acquisition is carried out in odd field I, as shown in Fig. V-8. Then, at the next field (II), the plate is hit and the plate illuminated. The impact is given at 5 ms after the blanking time. The light pulse position then is varied from the impact position onwards. Since the reference and the second exposures are separated by 16.7 ms, external disturbances are reduced.
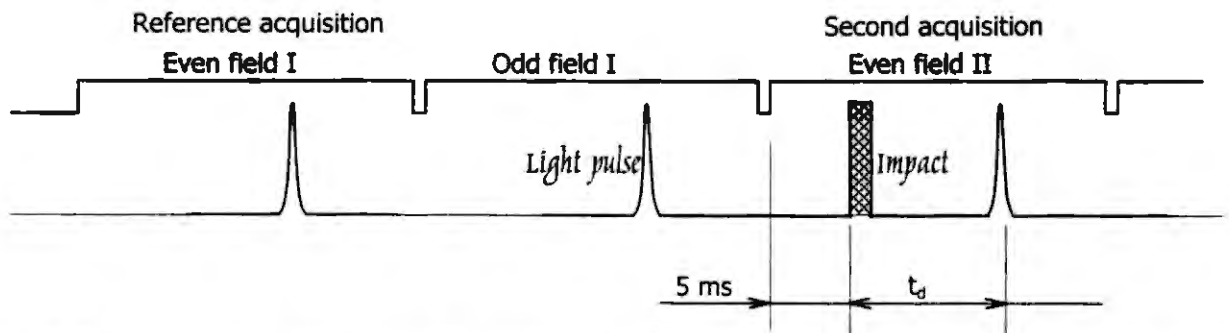
Fig. V-8. Relative times. The impact is given at 5 ms after the blanking period. The laser pulse illuminates the object at a variable time after the 5-ms offset. It may occur in subsequent fields inclusive. Enabling one light pulse per field avoids instabilities in the laser output [2].

V-2   Results

Method of **Section IV-4** is used throughout this chapter. For each measurement, four images are needed, the object image, the reference-beam image, the undeformed speckle pattern, and the speckle pattern with deformation, see Fig. V-9. At the start of a series of measurements (which include the same object at different times t_d) we get the first two images. Then, the other two are captured as is shown in Fig. V-8. We captured a reference speckle pattern with no deformation at each t_d as to reduce air disturbances. We observed that capturing the four images at each t_d was not necessary since both the object and the reference-beam images are hardly influenced by external disturbances. Therefore, the images shown in Figs. V-9a and V-9b are valid for the complete series. We have assumed that the experiment shows repeatability. We verified this by carrying out the experiment many times at a particular delay and checking that the correlation fringe map remained unchanged.

All the phase maps are given modulo 2π. Two iterations of a 3x3 median filter are then applied to the phase maps. Next, we employ an iterative unwrapping algorithm [3] to get the corresponding displacement maps, which are median-filtered as well.

As was shown in the previous chapter, DOP results are better than those obtained by POD. Due to this, only the DOP method will be considered further in this chapter.
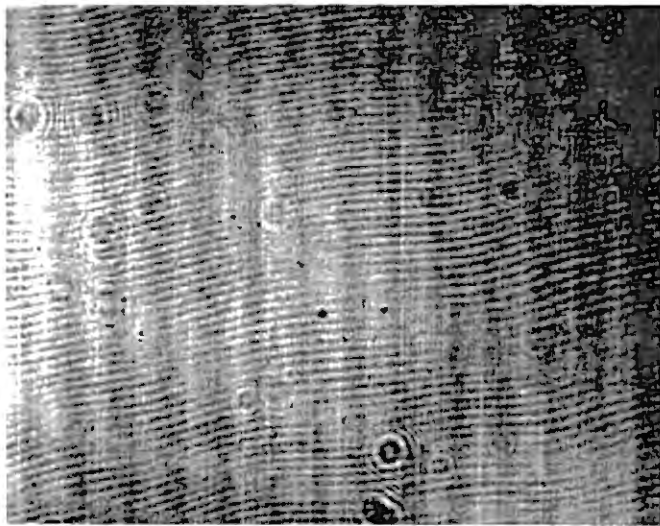
Fig. V-9a)
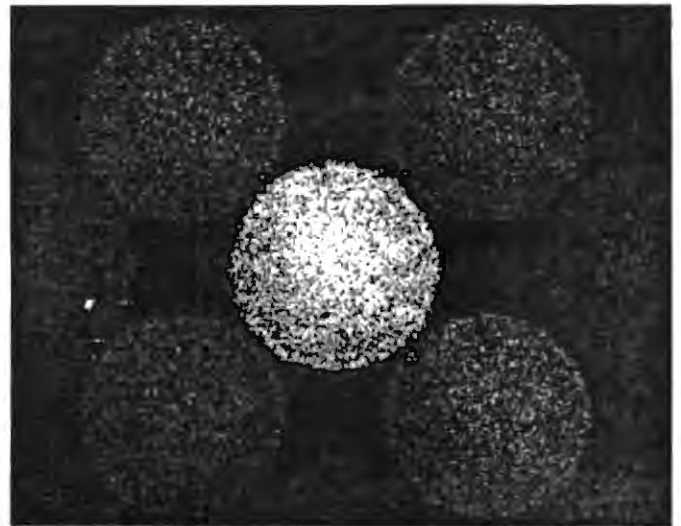
Fig. V-9b)
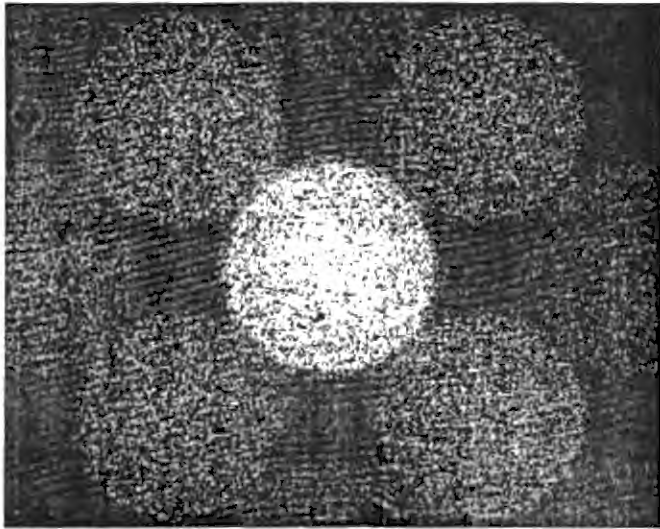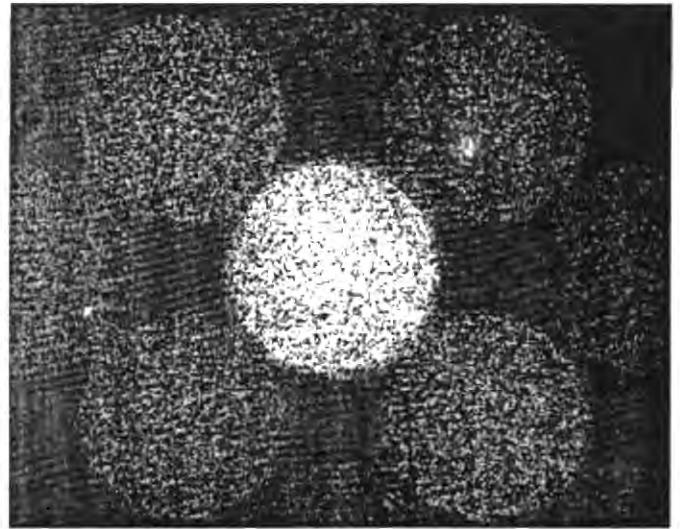
Fig. V-9c)   Fig. V-9d)

Fig. V-9. Images needed to measure deformation at a particular delay. a) The reference-beam image. b) The object beam image. c) The undeformed speckle pattern. d) Speckle pattern with deformation. In this case $t_d=8\ \mu s$. Images V-9a and V-9b are valid for the measurements shown in **Fig.** V-10.

V-2.1   Aluminum plate with no notch

We consider the object of Fig. V-5a which has no notch. An F number of 8 was used. The laser flash lamps were fed at 952 V. Only one negative lens was used and the region of interest corresponded to a 19-mm-diameter circle centered in the rectangular notch (or equivalently a 2.75-mm-diameter circle at the CCD).

Fig. V-10 shows direct subtraction maps at various delays. Figs. V-11a-d show some of the corresponding optical phase maps. From this latter figure, it is noticed that the mechanical wave propagates homogeneously in all directions.

At delays greater than 21 µs, the number of inconsistencies increases so much that unwrapping is not possible. This effect has to do with the high number of fringes arising from the increasing deformation. However, it is possible to compute their displacement maps by calculating the deformation between consecutive states and summing this result to the updated reference [4], as in Figs. V-11g and V-11h, at 21µs and 27 µs respectively.
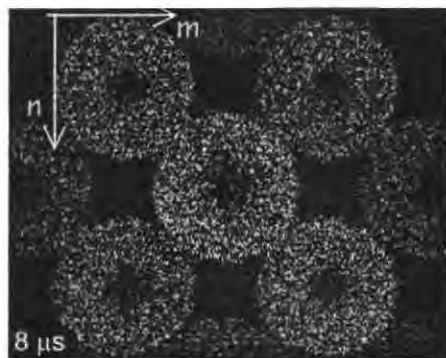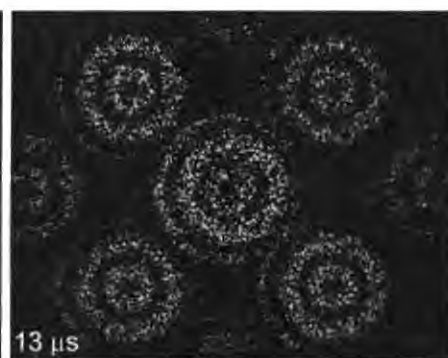
Fig. V-10a)   Fig. V-10b)   Fig. V-10c)
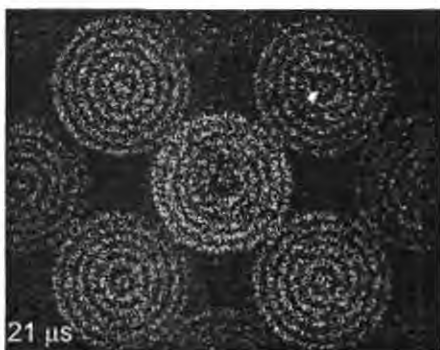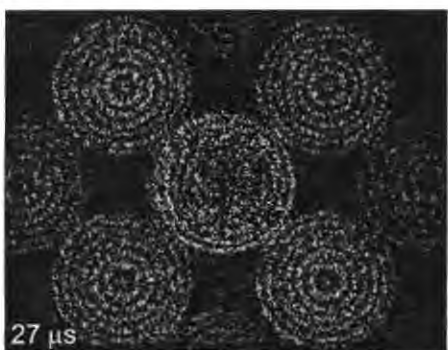
Fig. V-10d)   Fig. V-10e)   Fig. V-10f)

Fig. V-10. Subtraction correlation maps at several times after the impact. a) t_d= **8 μs**. b) t_d= **10 μs**. c) t_d= **13 μs**. d) t_d= **17 μs**. e) t_d= **21 μs**. f) t_d= **27 μs**. They correspond to the rectangular plate of **Fig.** *V*-**5a** with no notch.
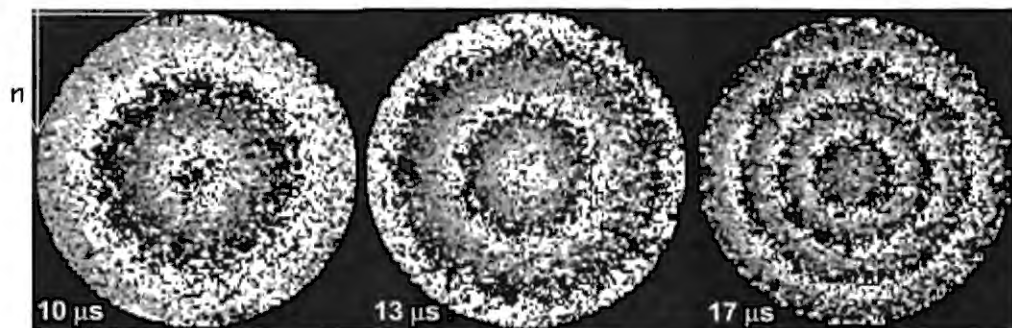
Fig. V-11a)   Fig. V-11b)   Fig. V-11c)   Fig. V-11d)
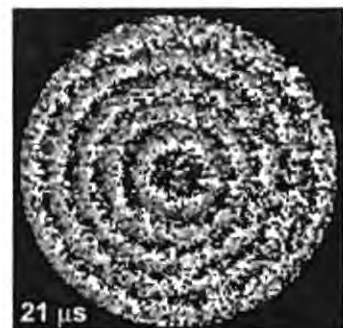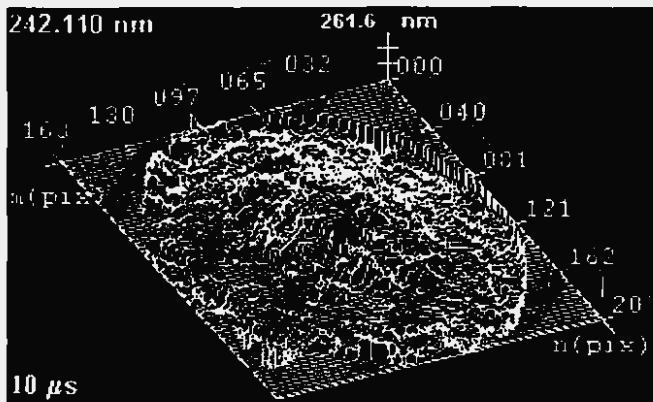
Fig. V-11e)
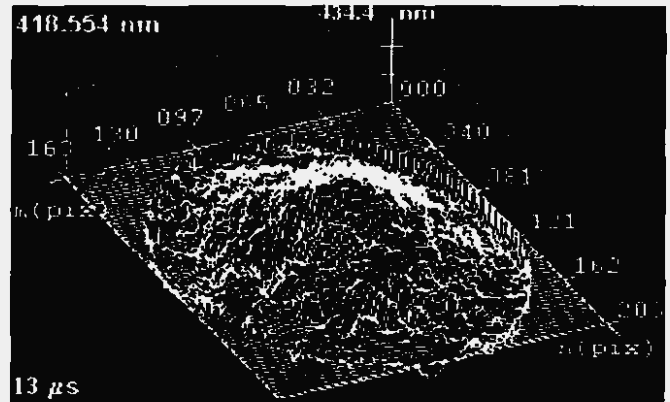
Fig. V-11f)
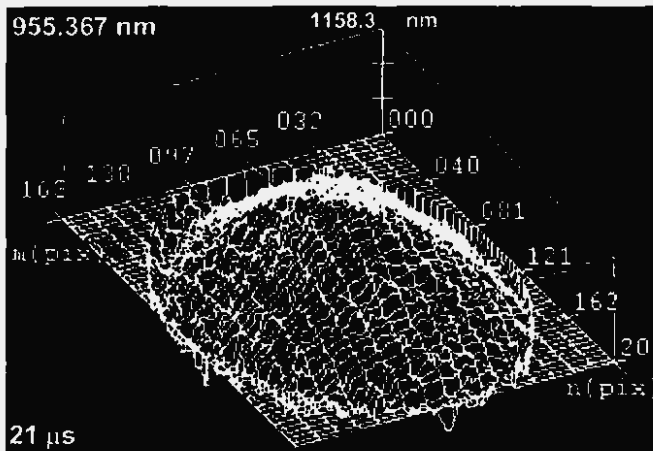
Fig. V-11g)
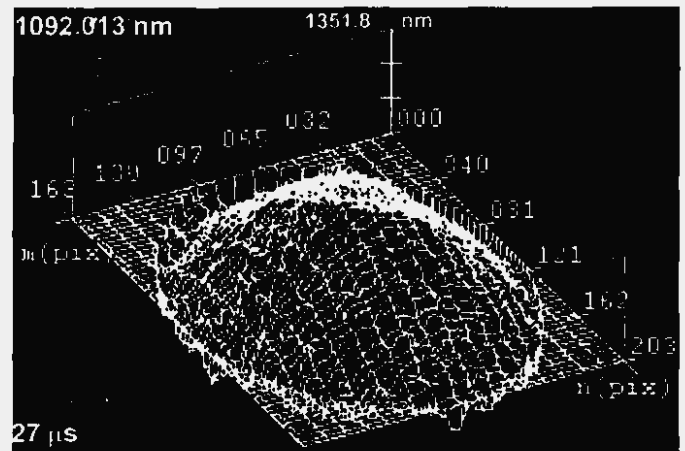
Fig. V-11h)

Fig. V-11. Optical phase maps at: a) t_d= **10 μs**. b) t_d= **13 μs**. c) t_d= **17 μs**. d) t_d= **21 μs**. Corresponding displacement maps at: e) t_d= **10 μs** (0.3184,-0.2667 μm, 2.2 fringes). f) t_d= **13 μs** (0.5275,-0.2549 μm, 2.9 fringes). g) t_d= **21 μs** (1.1583,-0.4907 μm, 6.2 fringes). h) t_d= **27 μs** (1.3518,-0.5660 μm, 7.2 fringes).The pair of numbers for each part represents the maximum and minimum displacement values before being filtered. The number in the top left-hand corner of each figure indicates the deformation at the center of the observed area.

The analysis of the plate showed that its behavior consisted of two parts. In the transient time, times less than 2500 μs, the plate can be studied as it were constrained along its four sides, whereas in the stationary part as is actually constrained, that is, in cantilever.

V-2.2   Aluminum plate with rectangular notch

In this section the object shown in Fig. V-5a is considered. Fig. V-12 shows the presence of local perturbations in the fringe patterns, elongation towards the right, due to the inclusion of the surface defect, even though is not visible (it is placed in the back of the specimen). As it

has already been shown, this is a useful technique for surface defect detection [1]. In Figs. V-12a and V-13b, the relative positions of the impact and the rectangular notch are indicated by a solid circle and a cross, respectively.
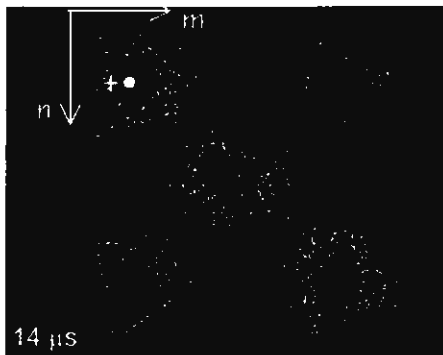
Fig. V-12a)
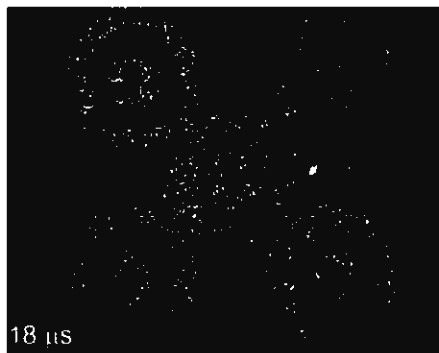
Fig. V-12b)

Fig. V-12c)
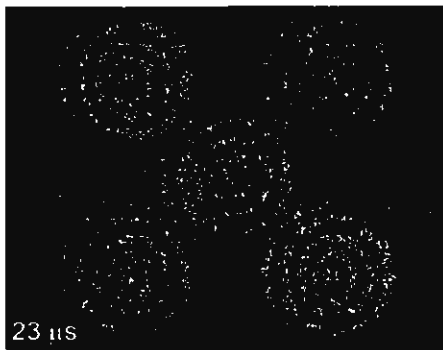
Fig. V-12d)
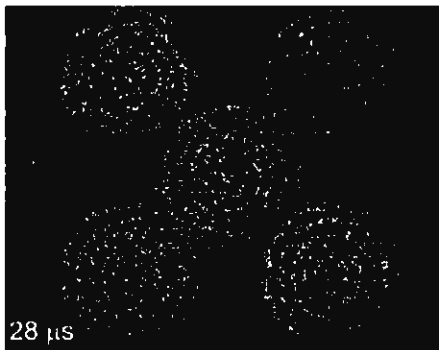
Fig. V-12e)
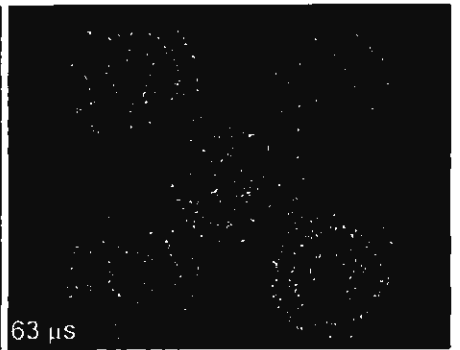
Fig. V-12f)
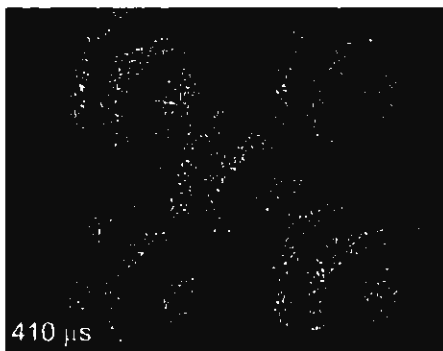
Fig. V-12g)
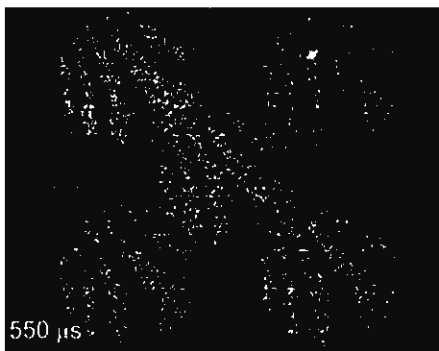
Fig. V-12h)
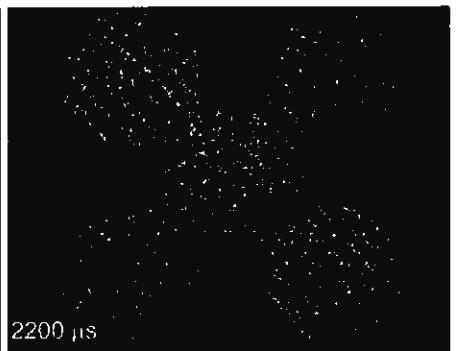
Fig. V-12i)

Fig. V-12. Fringe patterns at various t_d. a) t_d= 14 µs. b) t_d= 18 µs. c) t_d= 20 µs. d) t_d= 23 µs. e) t_d= 28 µs. f) t_d= 63 µs. g) t_d= 410 µs. h) t_d= 550 µs. i) t_d= 2200 µs. The observed area corresponds to a 19-mm-diameter circle at the object plane (1.375-mm-radius circle at the image plane.)

The series in Fig. V-12 shows the deformation time history of the plate. The differences with respect to the previous case, particularly the onset of the event, arise from the fact that in the present case a smaller force was applied.

Considering that the duration of the impact is 100 μs, the event is analized as the response of a mechanical system to a 100-μs step function (non-harmonic load). A first approximation to the solution to the motion equation is the Duhamel's integral [5], which is an analytical method used to determine the response of linear structures. This method assumes that the physical properties of the material are independent of time and any applied load. The displacement at a particular point as a function of time is given by:

$$y(t) = \frac{1}{m\omega_D} \int_o^t F(\tau) e^{-\xi\omega(t-\tau)} \sin(\omega_D(t-\tau)) d\tau,$$ (V-1)

where m is the mass of the body, ω is the natural frequency, ω_D denotes the damped frequency of the system, $F(t)$ is a general excitation and ξ is the damping ratio, which is defined as $c/(2m\omega)$, where c is the damping coefficient. More sophisticated methods used for the analysis of this problem involve wave propagation and structural dynamics, e.g. finite-element methods. The first field considers the study of wave generation after the application of a dynamic load on an object and the latter is concerned with reflected and refracted waves. Figs. V-12a to V-12f (and Figs. V-13a to V-13f) show the formation of a deformation peak at the center of the plate, e.g Fig. V-13i. This period of time has to do only with wave propagation. The notch introduces a delay in the wavefront propagating to the left (approaching perpendicularly to the n-axis). This gives rise to a greater deformation slope in this direction than in the right direction (receding from the n-axis). At times greater than 35 μs (Figs. V-12f and V-13f), the deformation peak starts decreasing -an oscillatory behaviour is reached. At later times (>100 μs), a mix of propagating and reflected waves occurs, as shown in Figs. V-12g-12i and V-13g, V-13h and V-13j. At the end of the transient, hyperbolic and straigth fringe patterns are produced as in stationary deformation, Figs. V-12h and V-13j and Fig. V-12i, respectively. The event dissapears in the observed area at about 2700 μs.

Fig. V-13a)   Fig. V-13b)   Fig. V-13c)   Fig. V-13d)

Fig. V-13e)   Fig. V-13f)   Fig. V-13g)   Fig. V-13h)

Fig. V-13i)   Fig. V-13j)
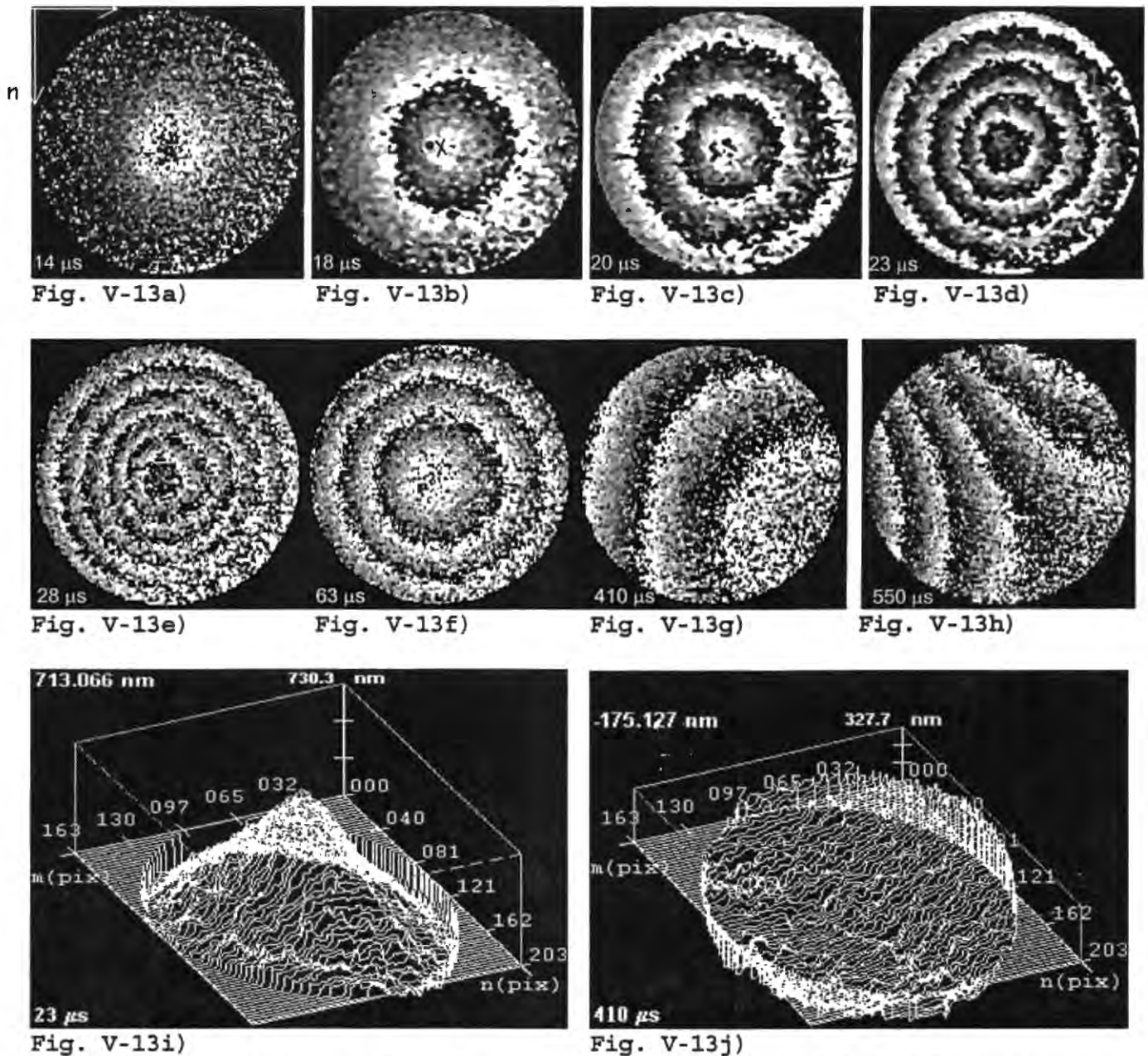
Fig. V-13. Optical phase maps associated with the fringe patterns of Fig. V-12. a) t_d= **14** μs. b) t_d= 18 μs. c) t_d= **20** μs. d) t_d= **23** μs. e) t_d= **28** μs. f) t_d= **63** μs. g) t_d= **410** μs. h) t_d= **550** μs. Displacement maps at: i) t_d= **23** μs 0.7303,-0.2472 μm). j) t_d= **410** μs (0.3277, -0.3116 μm).

V-2.3 Aluminum plate with circular notch

Results related to the aluminum plate of Fig. V-5b are presented. The region of interest corresponds to a 19-mm-diameter circle at the object plane or equivalently a 1.375-mm-radius circle at the CCD plane. The circular notch affects in two ways the mechanical perturbation: introduces a delay in the vertical direction (the notch works as an obstacle to the propagation) and produces reflected and refracted waves. The locations of the impact and the circular

notch are indicated by a full circle and a dashed arc in Figs. V-14a, V-15e and V-15g. The circle with continuous line indicates the observed area while a cross indicates the impact position.

Figs. V-14a-14c show the perturbation propagating upwards but delayed by the circular notch. At later times the fringe patterns consist of a mix of propagating and reflected waves, Figs. V-14d-14f. For t_d>12 µs, a depression zone starts forming in the upper part of the observed area, Fig. V-15e. At 19 µs the depression has almost reached the upper edge of the circular notch (approaching the m-axis), Figs. V-15f and V-15h.
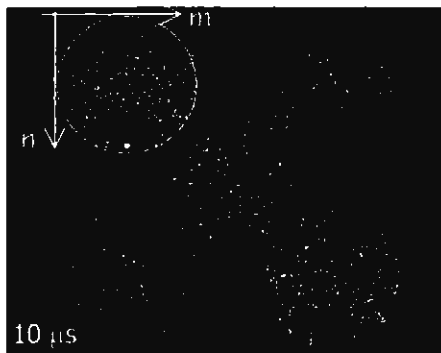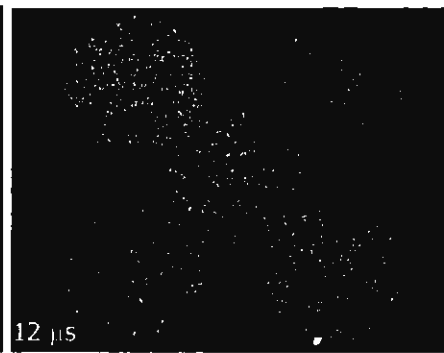
Fig. V-14a)   Fig. V-14b)   Fig. V-14c)
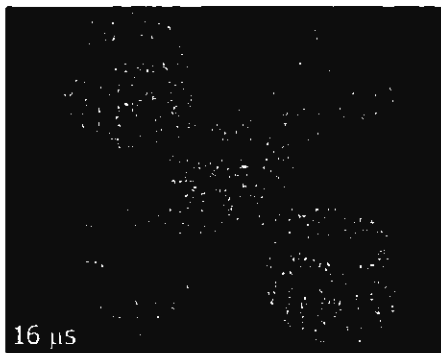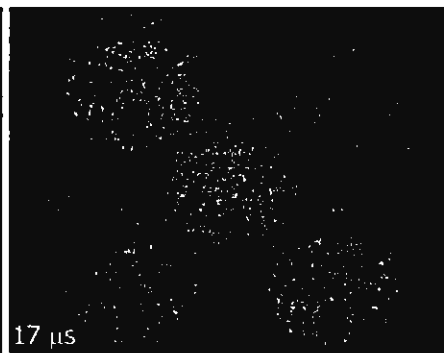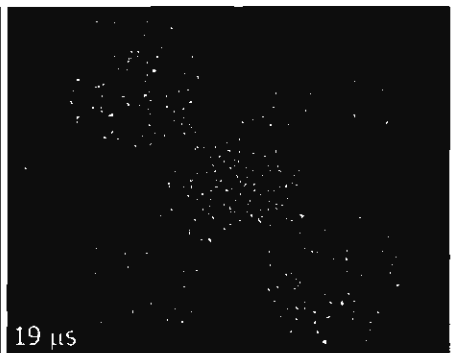
Fig. V-14d)   Fig. V-14e)   Fig. V-14f)

Fig. V-14. Fringe patterns at various t_d. a) t_d= 10 µs. b) t_d= 12 µs. c) t_d= 15 µs. d) t_d= 16 µs. e) t_d= 17 µs. f) t_d= 19 µs. The region of interest corresponds to a 19-mm-diameter circle at the object plane (1.375-mm circle at the image plane), indicated in a) by a solid circle. The electric hammer acted at 2 mm above the bottom edge of the region of interest and 7 mm below the bottom edge of the circular notch (indicated in a) by a dashed circle).

Fig. V-15a)   Fig. V-15b)   Fig. V-15c)   Fig. V-15d)

Fig. V-15e)   Fig. V-15f)

Fig. V-15g)   Fig. V-15h)
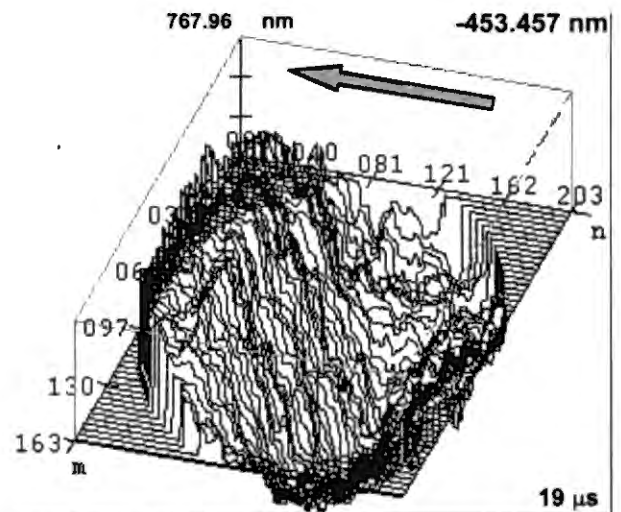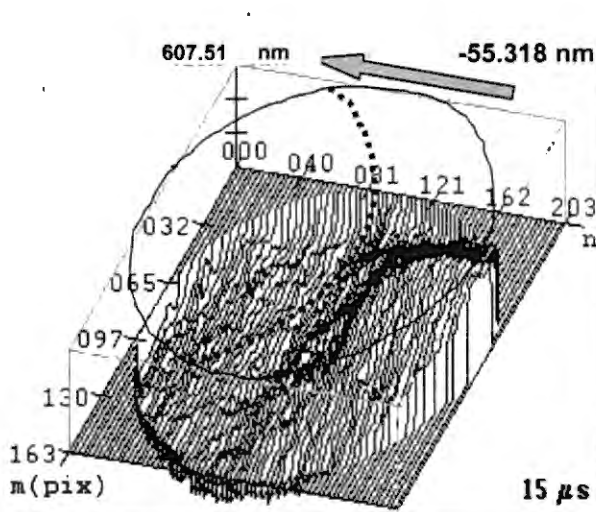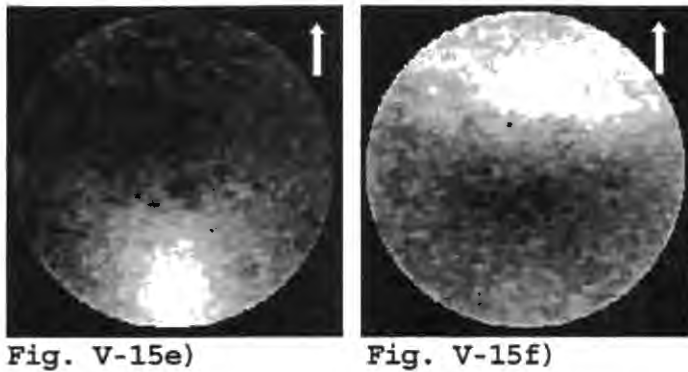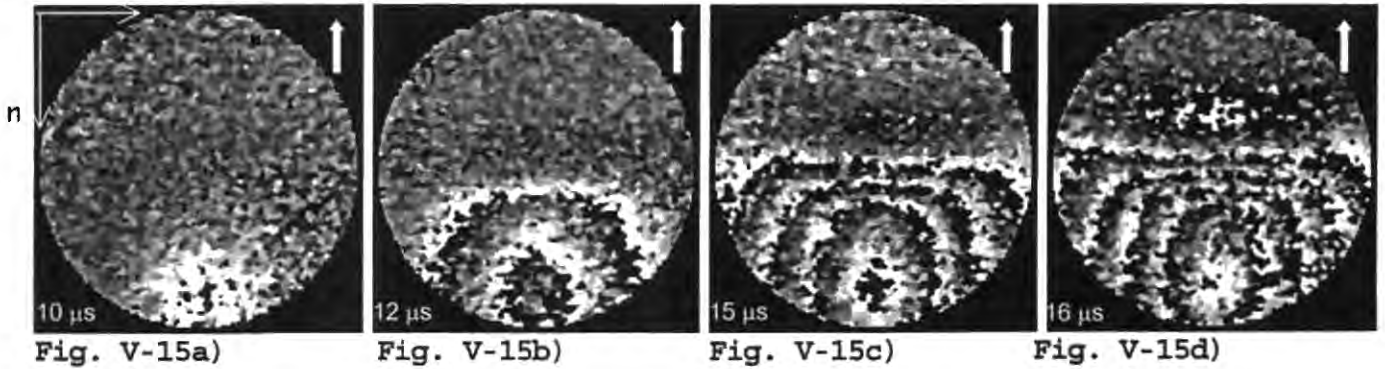
Fig. V-15. Optical phase maps associated with the fringe patterns of Fig. **V-16**. a) t_d= **10 μs**. b) t_d= **12 μs**. c) t_d= **15 μs**. d) t_d= **16 μs**. Displacement maps in gray levels at: e) t_d= 15 μs (607.51,-379.324,3.71 fringes), the circular notch is indicated by a dashed circle. f) t_d= **19 μs** (767.96,-1008.848,6.7 fringes), obtained by updating of reference. g) and h) as e) and f) in perspective, respectively. The region of interest corresponds to a 19-mm-diameter circle at the object plane. The arrows indicate the direction of the mechanical disturbance.

Figs. V-15a-d show the corresponding optical phase maps at t_d= {10, 12, 15, 16} μs. On the other hand, the displacement maps for t_d= {15, 19} μs are shown in Figs. V-15e-h, in gray levels and in perspective.

V-3   Validation of results

As it was shown in **Section IV-4**, the validation of the results for this method involves the calculation of three different error sources. The environmental noise is neglected in this case because we controlled the external conditions in the time between consecutive acquisitions, 16.7 ms. Similarly, the departure of conjugacy was eliminated. For completeness, Fig. V-16 shows that the departure of conjugacy is null considering the transient event of Fig. V-14. In this case, no deformation is introduced during the second acquisition and only environmental noise is expected to be present. The recordings were taken about 90 s apart. Figs. V-16a and V-16b show the subtraction patterns corresponding to the techniques indicated in Fig. V-7 and Fig. V-4 (**Ch. IV**), respectively. Their statistics are the following: mean intensity, 12.7322 and 13.6398 gray levels, standard deviation, ±10.42 and ±11.16 gray levels, limiting values, 0-254 gray levels in both cases. Fig. V-16c shows the phase map obtained from the fringe pattern of Fig. V-16a by DOP. From these figures, it is noticed that no spurious fringes arise from departure of conjugacy. Furthermore, the error stemming from misalignment of the CGH is null since the hologram remains unchanged during the measurements. Thus, there is actually one error source: the one arising from the normalization factors (which is expected to be practically the same as that calculated in **Chapter IV**, $3\sigma=\pm0.05\lambda=\pm 26.6$ nm.)
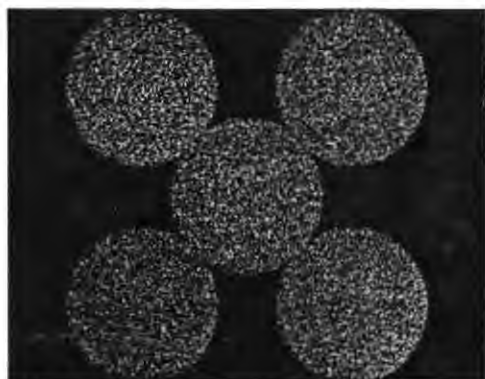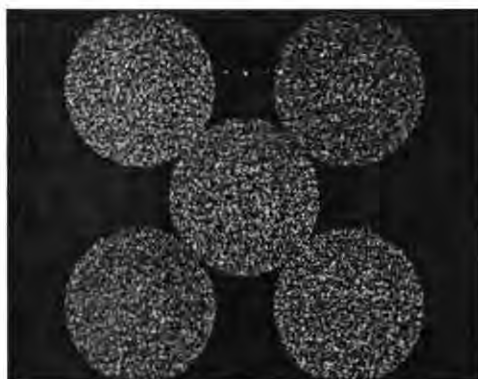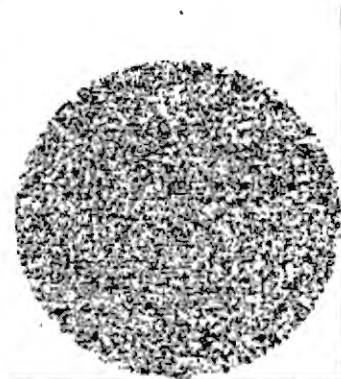
Fig. V-a)   Fig. V-16b)   Fig. V-16c)

Fig. V-16. Subtraction of identical deformation states. a) Subtraction by taking quadrant 1 as the reference speckle pattern (see diagram in **Fig. IV-7,**

Chapter IV.) b) Subtraction on a quadrant basis (see diagram in **Fig. IV-4,
Chapter IV.)** c) Phase map obtained from 16a by DOP.

By means of the introduction of a known change of the object, the precision (3σ) was found to be ~0.15λ. To obtain this, we proceeded as in the previous chapter, i.e. the plate was given an out-of-plane rotation and the result was compared to a fit plane.

V-4   Conclusions

We have implemented a transient method for ESPI. The obtained precision (3σ) was good (less than one sixth of the wavelength). The DOP method can readily cover any range of deformation if only deformation of two adjacent states is calculated. In general, the number of fringes which can be resolved by the unwrapping algorithm is less than 12 fringes, considering a 1.375-mm-radius circle at the image plane. Care must be taken when aligning the CGH since this is one of the most important factors that the overall precision depends on. Two other important factors are the departure of conjugacy and the correspondence pixel function.

The separation between consecutive acquisitions is the main drawback of the method presented here. Environmental disturbances should be controlled during this time.

V-5   References

[01] A. Fernandez, A. J. Moore, C. Perez-Lopez, A. F. Doval, J. Blanco-García, "Study of transient deformations with pulsed TV holography: Application to crack detection," Appl. Opt. **36**(10) 2058-2065 (1997).

[02] A. J. Moore and C. Perez-Lopez, "Low-frequency harmonic vibration analysis with double-pulsed addition electronic speckle pattern interferometry," Opt. Eng. **35**(9) 2641-2650 (1996).

[03] D. Kerr, G. H. Kaufmann, and G. E. Galizzi, "Unwrapping of interferometric phase-fringe maps by the discrete cosine transform," App. Opt. **35**(5) 810-816 (1996).

[04] S. Nakadate and H. Saito, "Fringe scanning speckle-pattern interferometry," App. Opt. **24**(14) 2172-2180 (1985).

[05] C. C. Spyrakos, *Finite Element Modeling in Engineering Practice*, Algor Publishing Division, Pittsburgh PA (1994).

[06] J. Lambros and A. J. Rosakis, "An experimental study of dynamic delamination of thick fiber reinforced polymeric matrix composites," Exp. Mech. **37**(3) 360-366 (1997).

Chapter VI   General conclusions and future work

VI-1   General conclusions

The presented results have shown the feasibility of the use of a CGH in spatial ESPI. We have successfully quantified transient events of the order of microseconds. In addition to this, we have extensively analyzed two techniques for phase calculation, DOP and POD, and confirmed that DOP produces better results (~0.15λ). Furthermore, some exploring work was carried out on two well-known unwrapping algorithms and we have concluded that the spiral algorithm is very promising for transient events since it can be executed very fast and is tolerable to high noise contents. On the other hand, the iterative algorithm presented a high precision with the noisiest images. However, it is time-consuming and then can not be used for live transient analyses.

In subtraction mode, the technique which involved a stepping grating resulted to be very useful since no change of any other parameter is needed to introduce phase step between consecutive recordings. This enabled us to have the information necessary for the calculation of the optical phase in any TV field. The feasibility of this technique was confirmed by the measurement of transient events in phase objects and static and transient events of mechanical pieces. The precision of the method is comparable to the reported in the literature.

We can summarize the main novel points that this work resulted in:

1   Implementation of spatial phase-stepping by the use of a CGH.
2   Calculation of the optical phase due to deformation at any time position without movement of any pieces or introduction of any change.
3   Quantification of high-speed transient events.

VI-2   Future work

To end up this work, we would like to put forward some possible further investigations related to this work.

A   Implementation of a polarization-based setup for double-pulsed addition. Double pulsed

addition combined with rapid cameras enables us to study very rapid transient events.

B Calculation of important mechanical parameters (at every pixel) in order to have a full understanding of the behavior of mechanical designs. Among these parameters we may mention velocity, acceleration, stress, strain, and bending and torsion moments. The advantage of the optical methods is the possibility to study the whole piece at once.

C Design and fabrication of CGHs. These elements are the core part of future versions of the optical arrangements.

D Comparison of ESPI results with FEM predictions.

Publications derived from this work:

1 B. Barrientos, A. J. Moore, C. Pérez-López, L. L. Wang and T. Tschudi, "Spatial phase-stepped Interferometry using a holographic optical element", to be published in Optical Engineering.

2 B. Barrientos, A. J. Moore, C. Pérez-López, L. L. Wang and T. Tschudi, "Transient deformation measurement with ESPI using a holographic optical element for spatial phase-stepping", to be published in Applied Optics.

Appendix A   Thin-lens model of a zoom-lens

We used a zoom-lens with effective focal distance f in the range of 70-210 mm and F number of 5.6.

Firstly, we checked that the numbers on the f scale of the zoom showed indeed the correct number. A nodal bank was used for this purpose. The precision was within ±4mm. Next, the thin-lens model was attained as follows.

1. While maintaining a fixed focal length and focussing at a distant point source, we measured the posterior (back) and anterior (front) focal plane distances, PFP and AFP (see Fig. A1), as 53 mm and 419 mm, respectively.
2. We read the value of f directly from the zoom scale as 181 mm.
3. The position of the principal planes (PPP and APP) were then obtained.

The resulting parameters are shown in Fig. A1. The physical length of the zoom is 113 mm with f=181 mm.
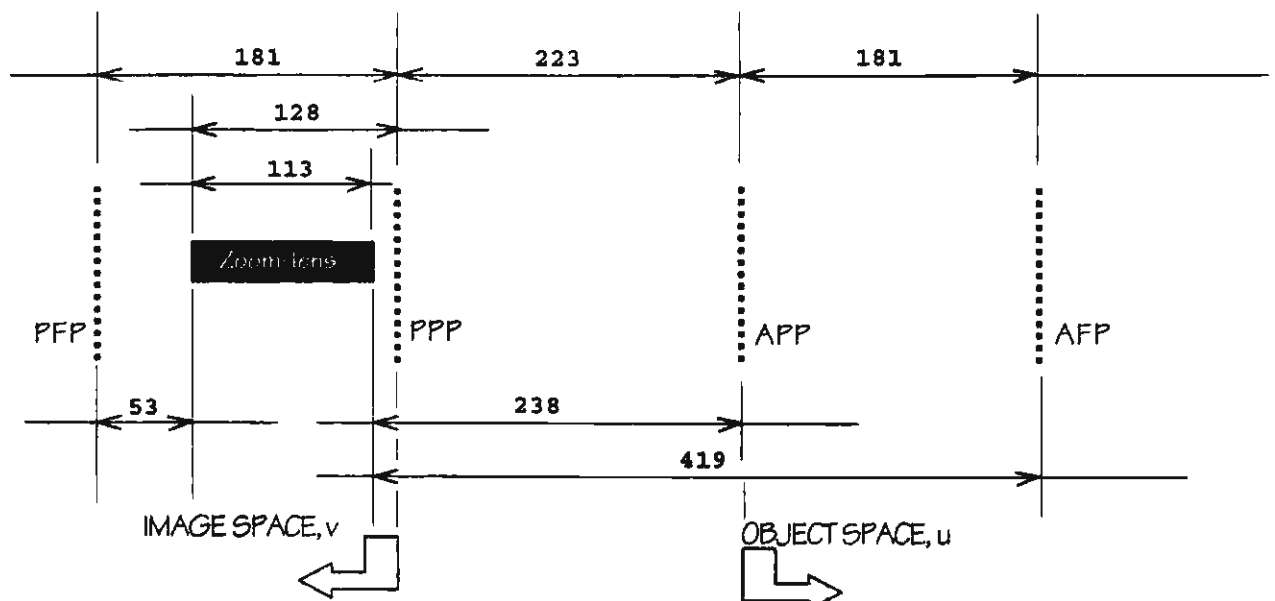
Fig. A1. Thin-lens representation of the zoom-lens. Dimensions are in **mm**.

When the zoom-lens is used as the imaging system, the values shown in Fig. A2 were measured.
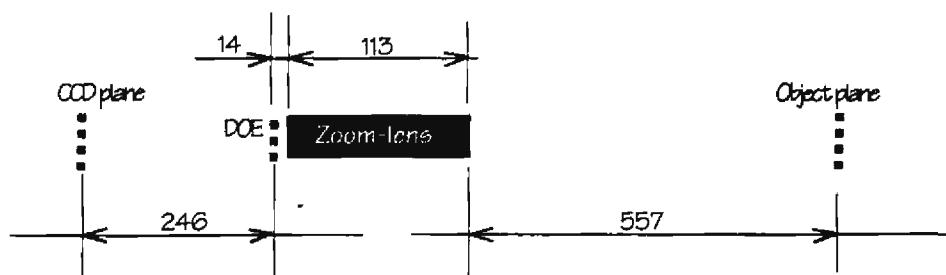
Fig. A2. Measured dimensions for the optical arrangement (mm).

In Fig. A2, the CCD-to-zoom distance was a fixed parameter and was calculated considering the diffraction power of the CGH as shown in **Chapter III**. The value of the effective focal distance, 181 mm, was chosen on account of several factors, namely the size of the mechanical holders, the size of auxiliary negative lenses and the object dimensions. The length of the optical rail, the optical aberrations, and the depth of field were considered as well.

Considering the dimensions in Figs. A2 and A1, we find that

$$246 + 14 + 113 + 557 = u(1+m) + 223 \tag{A1}$$

The magnification m resulted to be different in the y- and x-directions, 1.189 and 1.315, respectively. This difference gave rise to barrel distortion. The design was based on the length of the vertical side of the CCD sensor (6.6 mm), and the following distance values were obtained: $u=323$ mm, $v=384$ mm, and $f=175.4$ mm, which is close to the f read from the zoom scale, 181 mm. If the posterior and anterior sides of the zoom are taken as the reference positions for the image and object spaces, then the new coordinates for u and v are found as $u'= 323+238=561$ mm and $v'= 384-128-14=242$ mm, which are in good agreement with those shown in Fig. A2. By using the above values, the performance of the zoom is analyzed. Fig. A3 shows that the object-to-zoom and the effective focal distances are directly proportional. Furthermore, Fig. A4 shows that for a 45-mm-height object (as the object we actually used), u' (measured with respect to the zoom) is around 3500 mm. This length is too long to fit in an optical table, so we added an auxiliary negative lens with a 50-mm focal distance.
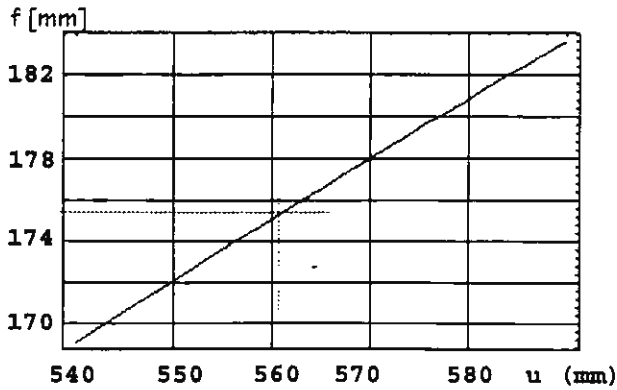
Fig. A3. Plot of f vs u. Here f=1/(1/(v+142)+1/(u+238)) and v is fixed to 260 mm.
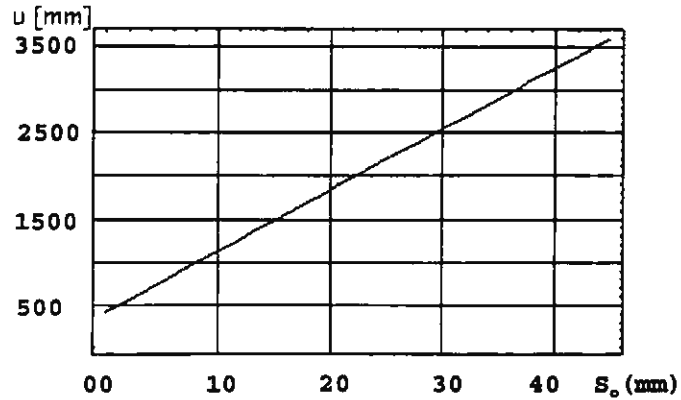
Fig. A4. Plot of u vs S_o, the object size. u=f(1+(S_o/2)/1.2375))+238. The image at the CCD is a fixed parameter, 1.2375 mm high.

The inclusion of a negative lens, as shown in Fig. A5, yields,

$$u_1 = f_1(\frac{m_z}{m} - 1) \qquad u = v_1 + c \qquad U = u_1 + c \qquad v_1 = \frac{u_1 f_1}{u_1 + f_1}, \qquad (A2)$$

where m_z denotes the zoom magnification (1.189) and f_1=-50 mm. Here m is the total magnification, S_o/S_i. The operation of this setup is analyzed from the plots in Figs. A6 and A7.
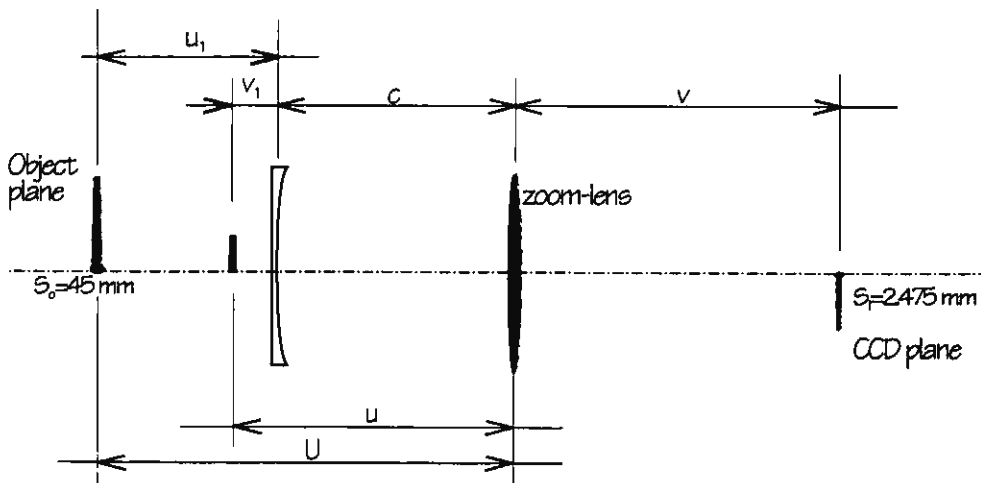
Fig. A5. The field of view is increased by the use of a negative lens.
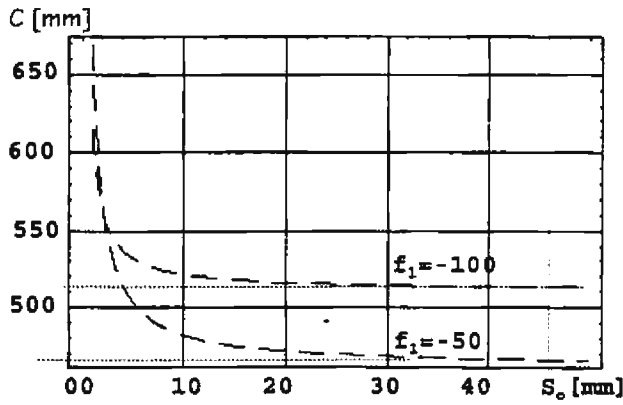
Fig. A6. Plot of c vs S_o. Here $c=u-f_1(1-m/m_2)$ with $u=561$ mm.
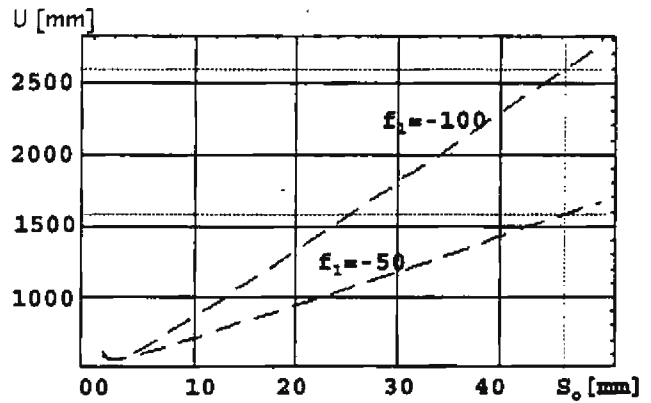
Fig. A7. Plot of U vs S_o. $U=u-f_1(2-m/m_2-m_2/m)$.

We can see from Fig. A6 that the zoom-to-negative-lens distance c is constant for object sizes greater than 30 mm. This means that this part of the arrangement may be used for focussing purposes. In Fig. A7, for an object size of 45 mm, the total length U is around 1500 mm, which is still too long, but less than that obtained with the first setup, 3500 mm. This configuration was actually used in **Chapter V** with $S_o= 19$ mm. Furthermore, notice that using a 100-mm-focal-distance negative lens U increases almost twice.

Should we add another negative lens, the setup will shorten further. The corresponding configuration is presented in Fig. A8.
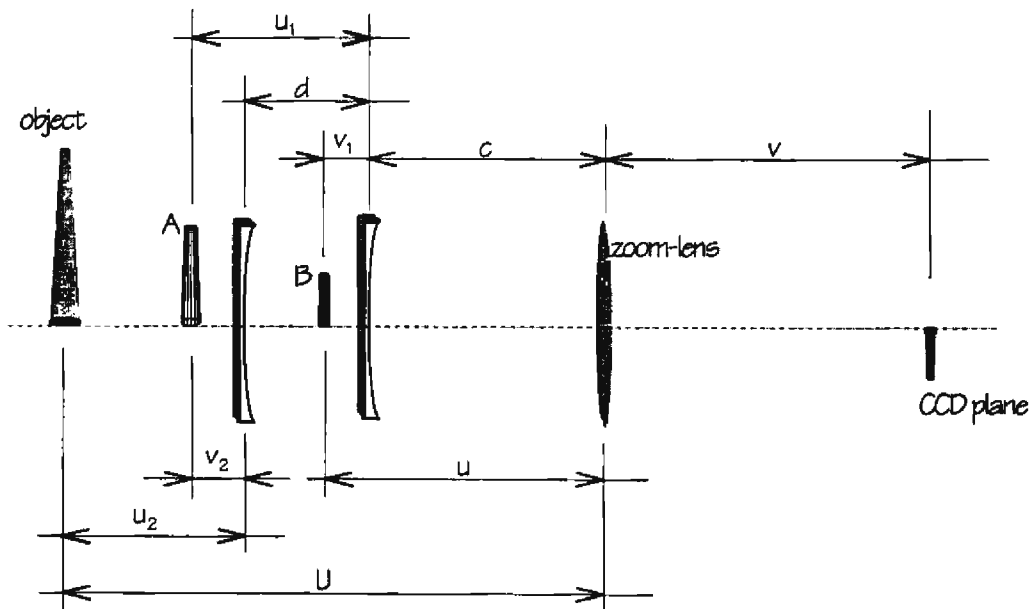
Fig. A8. This setup shortens further the total length U.

Eq. (A3) models this setup. Optimization of U with respect to u_1 and u_2 is assumed. Furthermore, we chose $f_1=f_2$.

$$u_1 = u_2 = f_1\left(\sqrt{\frac{v}{u}\frac{s_o}{s_1}} - 1\right),$$

$$v_1 = \frac{u_1 f_1}{u_1 + f_1}, \qquad d = \frac{u_1^2}{u_1 + f_1}, \qquad\qquad (A3)$$

$$c = u - v_1, \qquad U = u + \frac{2u_1^2}{u_1 + f_1}.$$

These expressions suggest some interesting features shown in Figs. A9, A10 and A11.
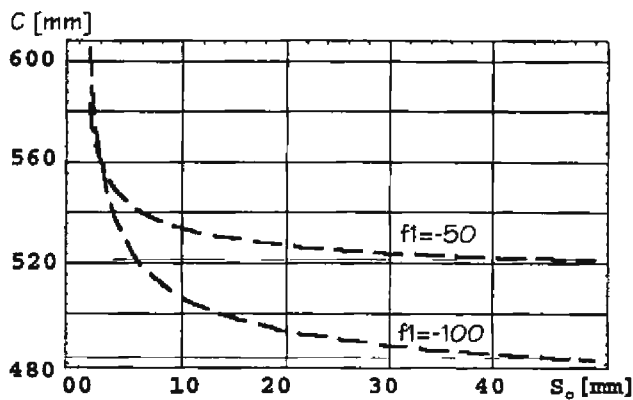
Fig. A9. Plot of c vs s_o. $c=u-f_1(1-(m/m_2)^{05})$. $u=561$ mm.
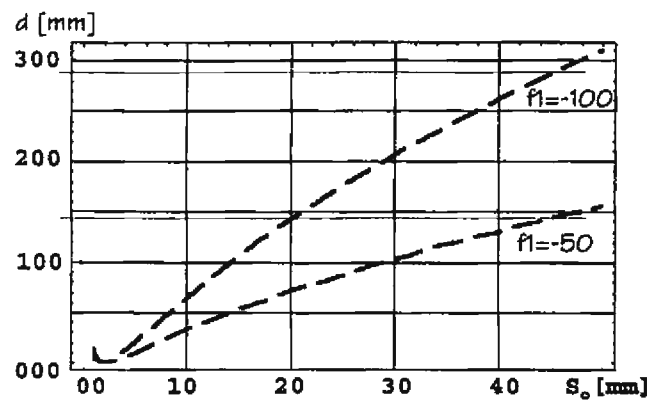
Fig. A10. Plot of d vs s_o. $d= f_1((m_2/m)^{05}+(m/m_2)^{05}-2)$.
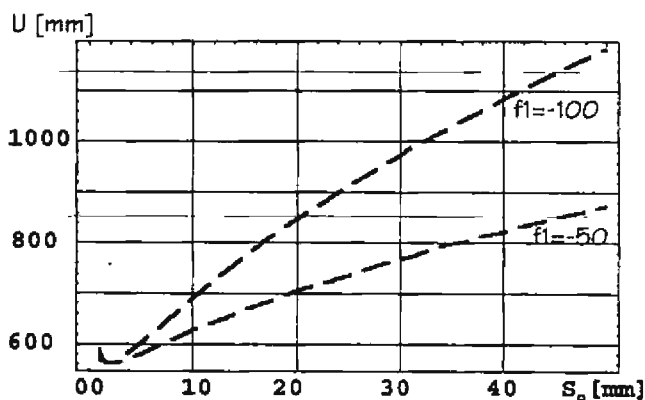
Fig. A11. Plot of U vs s_o. $U= u+2d$.

The tendency of Fig. A9 resembles that of Fig. A6, i.e. by slightly varying c, the object can be

focussed correctly. Fig. A10 shows that a small variation of d corresponds to a change of the allowable object size. This means that by changing this distance we can control the magnification of the system (remember that S_i is fixed to 2.475 mm at the CCD plane, see **Chapter III**). On the other hand, Fig. A11 shows that for the actual object size (45 mm) the total length is about 860 mm, which corresponds to half the value obtained in the previous case.

One important difference between the three previous setups is the brightness at the CCD. Although the latter setup was the dimmest and presented the less resolution, it enables us to analyze larger objects.

An important parameter related to the contrast of the interference fringes is the size of the speckle at the image plane. After trying different F numbers of the zoom, an F=5.6 was selected at f=70, so F=8 at f=175.4. See **Appendix B** for a revision of the measurement of the contrast.

Before 1987 [e.g., Ref. 1, except for [6]], it was thought that the speckle structure was fully resolved if only the speckle frequency was less than the Nyquist limit. That is to say, that a minimum of two pixels per speckle implied good visibility. However, as Wykes showed [2], a good modulation pixel for subtraction fringes is obtained yet the speckle frequency is greater than the Nyquist frequency. This has been confirmed experimentally in this work and in others [3]

The spatial distribution of the speckles is determined by the diffraction limit of the imaging system [4]. The diameter of the zoom aperture is calculated as 175.4/8=21.93 mm. Hence, the average diameter of the speckles at the CCD plane is 2.44(0.633)(384)/(21.93)=27.05 μm. We have used $d=2.44\lambda v/D$, where D is the diameter of the zoom-lens aperture. This formula was checked by displaying images with different F numbers and counting the number of speckles on the monitor. The diameter of the speckle is of the order of a pixel element sensor of the CCD, 11.5 μmx27 μm, and represents twice the Nyquist frequency.

The demagnification of the system is 45/(2*1.2375)= 18.1818. Then, the magnification of each negative lens is 0.2151, considering identical negative lenses and a zoom magnification of 1.189. The speckle size at plane B (Fig. A8) is therefore 22.75 μm, where we used $d=2.44(1+m)\lambda F/m$, with m being the magnification of the zoom. The speckle size at A and at the object plane is 105.77 μm

and 491.7 μm, respectively. This latter value is important when working with speckle photography since the illuminating light must remain coherent over one speckle diameter at the object plane [5]. Furthermore, as the object is rotated about an axis lying in the object plane, the speckle patterns after and before rotation become decorrelated when the angle is greater than [2] $0.1(\lambda/d_{ap, object\ plane})= 26.554''$, which is three times greater than the values obtained in **Chapter IV** (~4 fringes). This value agrees with the maximum number of fringes observed before decorrelation, 12.

References

[01] M. Lehmann, "Optimization of wave field intensities in phase-shifting speckle interferometry," Opt. Comm. **118** 199- 206 (1995).

[02] C. Wykes, "A theoretical approach to the optimization of electronic speckle interferometry fringes with limited laser power," J. Mod. Opt. **34** (4), 539-554 (1987).

[03] T. Yoshimura, M. Zhou, K. Yamahai, and Z. Liyan, "Optimum determination of speckle size to be used in electronic speckle pattern interferometry," App. Opt. **34** (1), 87-91 (1995).

[04] R. Jones and C. Wykes, *Holographic an Speckle Interferometry*, CUP, London 52-57 (1983).

[05] A. E. Ennos, "Speckle Interferometry," in *Laser Speckle and Related Phenomena*, Ed. J. C. Dainty, Springer-Verlag N. Y. 239 (1975).

[06] G. A. Massey, "Photomixing with diffusely reflected light", App. Opt. **4** 781-785 1965).

Appendix B   Correspondence function

The determination of the pixel correspondence involves two operations: translation and shape transformation. If the four quadrant images produced by the CGH are identical, a translation function will suffice. On the other hand, when the images are different because of optical and diffractive aberrations, both operations must be performed.

Let an ideal quadrant image be the reference image. The problem is to find the best function that relates an actual quadrant image to the reference image. The relationship between these two images is shown in Fig. B1.
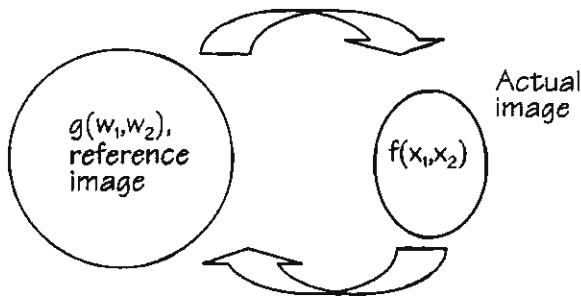
Fig. B1. Geometrical correspondence of two images.

We use the Polynomial warp model ['] to compensate for nonideal geometrical optics. This model uses a polynomial function, which describes the distortions, and a set of known corresponding image points of the form (x,w). Notice that only geometry is dealt with so far. The coordinates in both spaces may be related by

$$x_1 = g_1(w_1, w_2) \quad \text{and}$$
$$x_2 = g_2(w_1, w_2).$$

(B1)

The degree of the Nth order 2D polynomial depends on the number of known points (control points) so that the polynomial warp relationship is expressed by

$$x_1 = \sum_{i=0}^{N} \sum_{j=0}^{N} k_{i,j}^1 w_1^i w_2^j \quad \text{and}$$
$$x_2 = \sum_{i=0}^{N} \sum_{j=0}^{N} k_{i,j}^2 w_1^i w_2^j.$$

(B2)

These equations are applied to every control point. Given a set of m corresponding control points $[(x_{1i},x_{2i}),(w_{1i},w_{2i}), i=1,\ldots,m]$, the polynomial coefficients k can then be estimated, and a fit relationship may be obtained. If the order N is equal to 2 (up to powers of 2) in a 2D case, 18 coefficients must be estimated. Every control point yields two equations according to Eq. (B2). Therefore, a minimum of nine control points which produce linearly independent equations are necessary. The polynomial coefficients can then be calculated by a least-squares fit. The resulting coefficient matrix is symmetrical.

In our case, we used a circular reference mask with 29 control points, as shown in Fig. B2. The mask covered completely the actual object, which was an aluminum circular plate of diameter 45 mm. We chose a white mask in a black background to avoid overlapping of spurious reflected light. The image of the calibration mask is shown in Fig. B3.
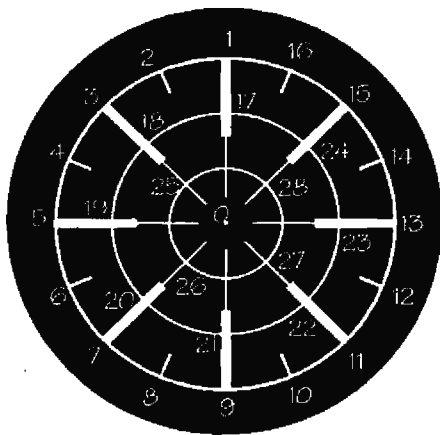
Fig. B2. Calibration mask.
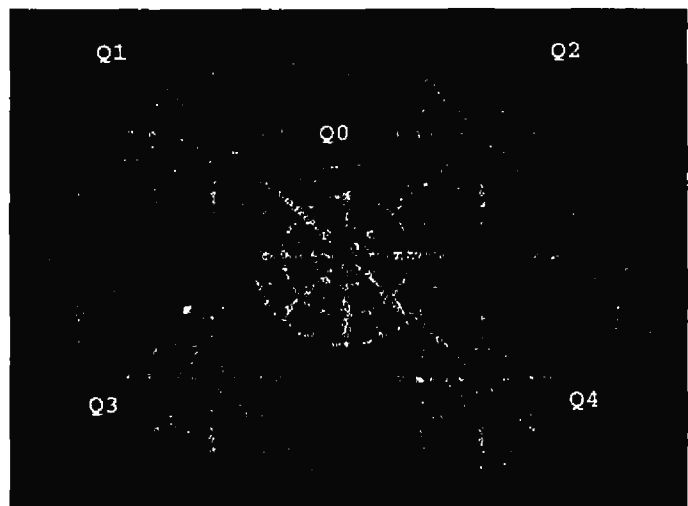
Fig. B3. Calibration image. Q stands for quadrant.

It is better to use an absolute coordinate system than a local system to the quadrant images. Furthermore, it is convenient that the transformation goes from the reference circle to a distorted image since interpolation of the corresponding intensity values is straightforward, see Fig. B4. Then, the problem consists of finding the polynomial coefficients that represent the distorted image out of an ideal image, that is, the coefficients that will transform one pixel point of the ideal image into one point of the distorted image. In this case, the (w_1,w_2) coordinate system corresponds to the ideal image coordinate, see Fig. B4. For an ideal point, say A, we want to know its corresponding point E' in the distorted image. Generally, E' is not an integer number and

therefore the corresponding intensity value of A is not known. A bilinear interpolation ['] may be applied to the intensity values in the (x_1, x_2) coordinate system. The corresponding intensity for each transformed pixel is readily found. If this process were done the other way round, the ideal intensity values would not be obtained straightforward. The ideal image (reference image) may be either any of the five quadrant images or a synthetic circular image.
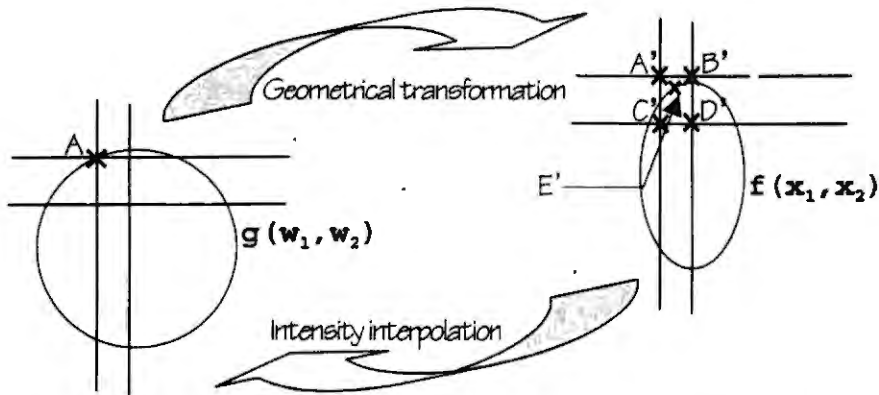
Fig. B4. Coordinate correspondence function. The interpolation of the intensity is done in the (x_1, x_2) coordinate system.

Fig. B5 shows the transformed image after the application of the above transformations to a distorted image. The recovered image, shown in Fig. B5b, is very well reconstructed in shape and intensity.
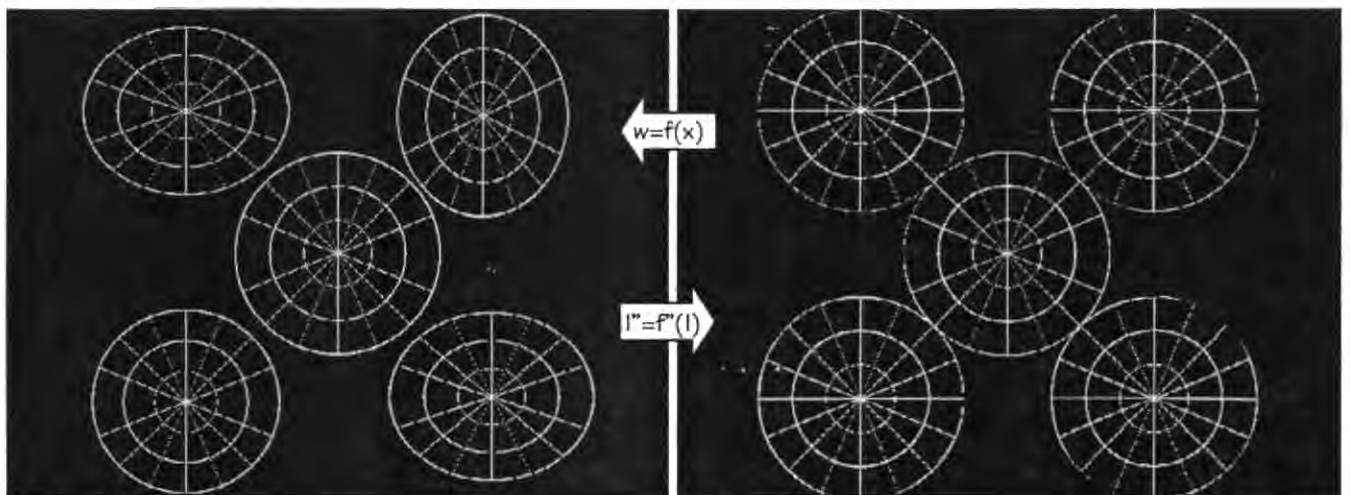
Fig. B5a)   Fig. B5b)

Fig. B5. a) Image for simulation of distortions. b) Figure **B5a** after geometrical transformation and intensity interpolation.

By using Fig. B3 as the calibrating image, the speckle pattern in Fig. B6b was obtained. The original image was the speckle pattern in Fig. B6a. A synthetic circle was used as the reference (ideal) image. The calculated polynomial coefficients are given next, considering the notation of Eq. (B2), with the last subscript denoting the quadrant number.

X_1-components

Q0:

$k_{000}^1 = -2.9756879807$ $k_{100}^1 = 0.7945592403$ $k_{010}^1 = 0.1239135861$ $k_{110}^1 = 0.0004956828$ $k_{200}^1 = 0.0007009467$

$k_{020}^1 = -0.0004293395$ $k_{210}^1 = -0.0000032818$ $k_{120}^1 = 0.0000005759$ $k_{220}^1 = 0.0000000032$

Q1:

$k_{001}^1 = -6.0621342659$ $k_{101}^1 = 1.1298633814$ $k_{011}^1 = 0.2605473995$ $k_{111}^1 = -0.0032634209$ $k_{201}^1 = -0.0003386778$

$k_{021}^1 = -0.0011765613$ $k_{211}^1 = 0.0000097919$ $k_{121}^1 = 0.0000157108$ $k_{221}^1 = -0.0000000505$

Q2:

$k_{002}^1 = 30.0184059143$ $k_{102}^1 = 0.7202757001$ $k_{012}^1 = -0.5461848378$ $k_{112}^1 = 0.0035843041$ $k_{202}^1 = 0.0004250411$

$k_{022}^1 = 0.0014513778$ $k_{212}^1 = -0.0000057183$ $k_{122}^1 = -0.0000101697$ $k_{222}^1 = 0.0000000170$

Q3:

$k_{003}^1 = 105.9143142700$ $k_{103}^1 = -0.1651912928$ $k_{013}^1 = -0.5568541288$ $k_{113}^1 = 0.0064871674$ $k_{203}^1 = 0.0034467829$

$k_{023}^1 = 0.0007665969$ $k_{213}^1 = -0.0000193678$ $k_{123}^1 = -0.0000089622$ $k_{223}^1 = 0.0000000267$

Q4:

$k_{004}^1 = -131.6893920898$ $k_{104}^1 = 1.2602244616$ $k_{014}^1 = 0.6772741079$ $k_{114}^1 = -0.0017478025$ $k_{204}^1 = 0.0002201915$

$k_{024}^1 = -0.0009590631$ $k_{214}^1 = -0.0000006188$ $k_{124}^1 = 0.0000027373$ $k_{224}^1 = 0.0000000001$

X_2-components

Q0:

$k_{000}^2 = 84.3562240601$ $k_{100}^2 = -0.8455627561$ $k_{010}^2 = 0.0465923660$ $k_{110}^2 = 0.0089851590$ $k_{200}^2 = 0.0018437624$

$k_{020}^2 = 0.0024027843$ $k_{210}^2 = -0.0000192709$ $k_{120}^2 = -0.0000225665$ $k_{220}^2 = 0.0000000479$

Q1:

$k_{001}^2 = 32.6362953186$ $k_{101}^2 = -0.1841133833$ $k_{011}^2 = 0.7399266958$ $k_{111}^2 = 0.0039056935$ $k_{201}^2 = 0.000617$

$k_{021}^2 = 0.0010386588$ $k_{211}^2 = -0.0000144595$ $k_{121}^2 = -0.0000191791$ $k_{221}^2 = 0.0000000732$

Q2:

$k_{002}^2 = 64.0785369873$ $k_{102}^2 = -0.2638016939$ $k_{012}^2 = 0.9037903547$ $k_{112}^2 = 0.0008223093$ $k_{202}^2 = 0.000382390$

$k_{022}^2 = -0.0015280402$ $k_{212}^2 = -0.0000016339$ $k_{122}^2 = 0.0000059186$ $k_{222}^2 = -0.0000000053$

Q3:

$k_{003}^2 = -19.1813678741$ $k_{103}^2 = -0.1127793863$ $k_{013}^2 = 1.1047704220$ $k_{113}^2 = -0.0010108246$ $k_{203}^2 = 0.0004856$

$k_{023}^2 = -0.0003023864$ $k_{213}^2 = 0.0000029309$ $k_{123}^2 = 0.0000029777$ $k_{223}^2 = -0.0000000094$

Q4:

$k_{004}^2 = -9.2733707428$ $k_{104}^2 = -0.3690173328$ $k_{014}^2 = 1.4599124193$ $k_{114}^2 = -0.0007636343$ $k_{204}^2 = 0.00091164$

$k_{024}^2 = -0.0011871245$ $k_{214}^2 = -0.0000012844$ $k_{124}^2 = 0.0000037684$ $k_{224}^2 = -0.0000000018$

It is noticed that only the first four terms are important, i.e. a constant term ($k_{00Quad}^{Component}$), w_{1i}-terms ($k_{10Quad}^{Component}$), w_{2i}-terms ($k_{01Quad}^{Component}$), and $w_{1i} w_{2i}$-terms ($k_{11Quad}^{Component}$).
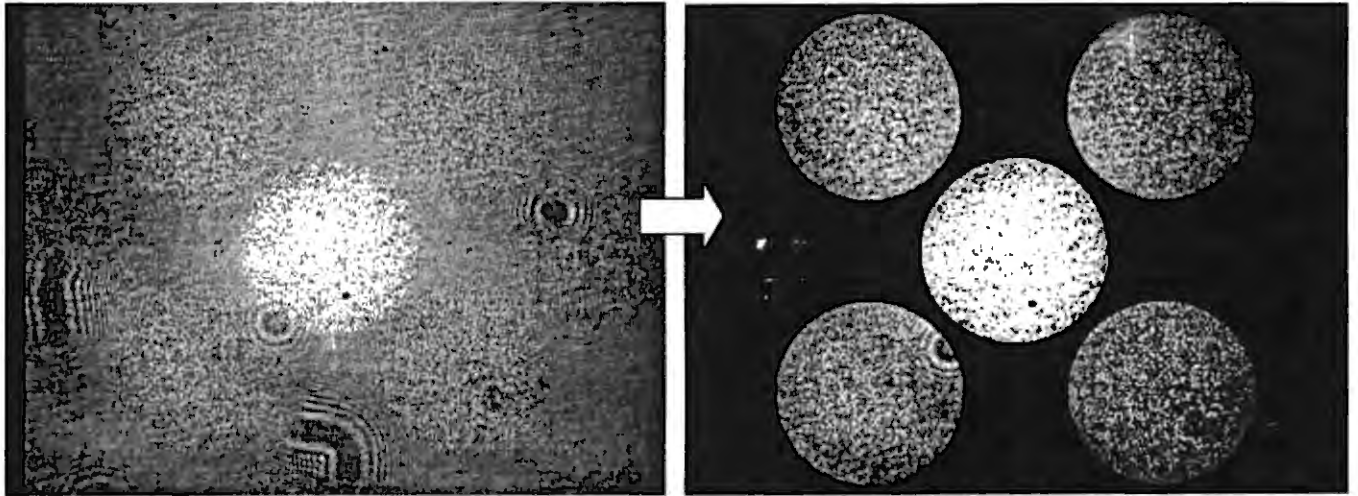
Fig. B6a)   Fig. B6b)

Fig. B6. a) Original image with a phase-referenced speckle pattern. b) Image after geometric and intensity transformations.

In our experiments, the difference between quadrant images due to aberrations was less than one pixel. This enabled us to use a simple translation function for the calculation of the corresponding function, which can be determined analytically by spatial cross correlation [2]:

$$I_{fg} = \int\limits_{-\infty}^{+\infty}\int\limits_{-\infty}^{+\infty} f^{*}(m,n)g(m+\Delta m, n+\Delta n)\,dm\,dn,\tag{B3}$$

where $f(m,n)$ and $g(m,n)$ are the spatial functions (two speckle-pattern quadrant images) and Δm and Δn are the relative spatial displacements between the two functions. Both functions are referenced to a local (m,n) coordinate system. The peak value of this function represents the best match between the functions.

Another method to find the translation function consists of calculating subtraction-correlation fringes between the five quadrants produced by a hologram (see diagram in Fig. IV-7, **Chapter IV**). Thus, we subtract each quadrant image in turn from the reference quadrant Q_1. If the contrast of the resulting fringe pattern is good, then the center of the quadrant has been found, otherwise, the current center is changed and a new subtraction is done. We assume that all quadrant images are identical and that the coordinate origin (center) of the reference Q_1 is kept to a fixed value. The inspection of the contrast may be done automatically, by calculating the ratio of the

standard deviation and the mean [3], or by direct observation.

References

[01] R. J. Schalkoff, *Digital Image Processing and Computer vision*, Wiley & Sons, N. Y. 51-56 (1976).

[02] T. D. Upton and D. W. Watt, "Optical and electronic design of a calibrated multichannel electronic interferometer for quantitative flow visualization," App. Opt. **34**, 5602-5610 (1995).

[03] J. W. Goodman, "Statistical Properties of Laser Speckle Patterns," in *Laser Speckle and Related Phenomena*, Ed. J.C. Dainty, Springer-Verlag, N. Y. 17 (1975).

Appendix C   Implementation of the Carré algorithm

The Carré algorithm involves four intensity measurements with a constant phase step $\Delta\theta$ between them, where $\Delta\theta_l(x,y) = \{-3\alpha(x,y), -\alpha(x,y), \alpha(x,y), 3\alpha(x,y)\}$; with $l = 1, 2, 3, 4$. The Carré expressions for the phase step and the optical phase are given by

$$\alpha(x,y) = \tan^{-1}\frac{\sqrt{3(I_2 - I_3) - (I_1 - I_4)}}{(I_2 - I_3) + (I_1 - I_4)}, \tag{C1}$$

$$\phi(x,y) = \tan^{-1}\frac{\sqrt{[3(I_2 - I_3) - (I_1 - I_4)][(I_2 - I_3) + (I_1 - I_4)]}}{(I_2 + I_3) - (I_1 + I_4)}, \tag{C2}$$

respectively, where the (x,y) dependence of the intensities is implied. If we replace I_2 by I_3 and I_1 by I_4 in these equations, they will remain unchanged. The subscripts in Eqs. (C1) and (C2) are assigned to corresponding pixels in the four quadrants, following the convention below.

According to the original design of the CGH, the expected stepping is as shown in Fig. C1a. However, at the CCD, the optical arrangement inverts the diffraction orders in the x-direction and in the y-direction, as shown in Fig. C1b.
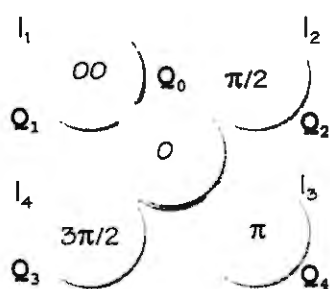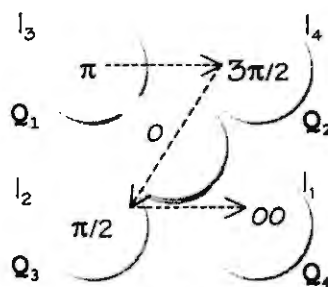
Fig. C1a)   **Fig. C1b)**

Fig. C1. Designed stepping of the CGH. a) Stepping obtained in transmission. b) Stepping detected by the CCD.

If we assign the subscripts 1,2,3,4 to the diffraction orders considering the phase step ($I_1 \rightarrow -3\alpha \rightarrow 0$, $I_2 \rightarrow -\alpha \rightarrow \pi/2$, $I_3 \rightarrow +\alpha \rightarrow \pi$, and $I_4 \rightarrow +3\alpha \rightarrow 3\pi/2$), then Fig. C1a will be labeled with the combination

1243. Similarly, label 3421 will correspond to Fig. C1b. Every number denotes the phase step and its position means the quadrant. Take this case, 3241. This label means that the intensity of the corresponding pixel in quadrant 1 has a phase step of π rad, that the pixel in quadrant 4 has a phase step of 0 rad, and so on. Taking into account the previous valid replacements (position 4 by position 1, i.e. the pixel intensity in Q_4 by the pixel intensity in Q_1, and position 2 by position 3), combination 1234 is equivalent to 4321, see Fig. C2. Therefore, the total number of combinations is 12. Now, if the phase step 2α, in Eqs. (C1) and (C2), is $\pi/2$ rad, all possible combinations are equivalent.
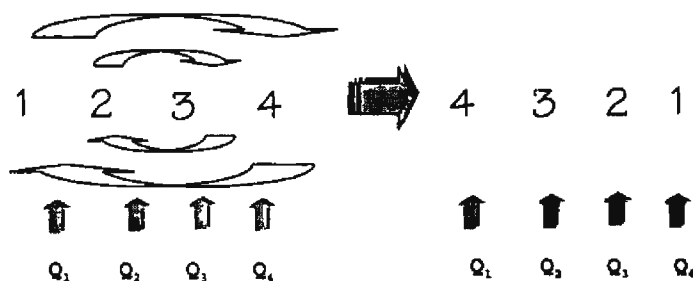
Fig. C2. Equivalent combinations, **1234≡4321**.

We found that each pixel had a different constant phase step, so each behaved as a separate interferometer. In practice, the phase step was found to vary due to tilt of the CGHs. For the nonstepping CGH, unwanted error steps could be introduced between the diffracted orders, and for the stepping CGH the step size would deviate from $\pi/2$ radians. Therefore, a CGH mount was designed so that correct alignment of the CGHs could be achieved The CGHs need only be positioned once when setting up the interferometer.

The results of this work were obtained by using combination 2413≡3142, where the corresponding pixels presented the following stepping: Q_3, -3α; Q_1, $-\alpha$; Q_4, α; and Q_2, 3α. A typical average value for the stepping of a speckle pattern was $2\alpha \approx 100°\pm 11°$, where the last number stands for the standard deviation (we obtained a similar error for a calibrated-PZT temporal phase-stepping of $\pi/2$). Considering the sample theorem, the phase step must be in the range of 0-π rad if a good intensity modulation is to be attained [1].

In **Chapters IV** and **V** some statistics are reported for each experiment. They are related to the

percentage of valid pixels. Some pixels are taken as invalid when the modulation is less than a percentage of the average intensity modulation, which is 127 in an 8-bit digitizing board. Then, a pixel is marked as invalid when [2]

$$[(I_2 + I_3) - (I_1 + I_4)]^2 + [(I_2 - I_3) + (I_1 - I_4)]^2 <= 8.0 \, I_{mod}, \tag{C3}$$

where I_{mod} is the intensity threshold, i.e. percentage*127.

References

[01] K. Creath, "Comparison of phase-measurement algorithms," SPIE Vol. **680**, Surface characterization and testing 19-28 (1986).

[02] K. Creath, "Temporal Phase Measurement Methods", in *Interferogram Analysis*, Ed. by D.W. Robinson and G.T. Reid, IOP 106-108 (1993).